The Dissertation Committee for Burton Hamilton Neuner III
certifies that this is the approved version of the following dissertation:

Controlling Infrared Radiation with Subwavelength Metamaterials and Silicon Carbide

Committee:

Gennady Shvets, Supervisor

Manfred Fink

Ernst-Ludwig Florin

Zhen Yao

Xiaojing Zhang

Controlling Infrared Radiation with Subwavelength Metamaterials and Silicon Carbide

by

Burton Hamilton Neuner III, B.S.

DISSERTATION
Presented to the Faculty of the Graduate School of
The University of Texas at Austin
in Partial Fulfillment
of the Requirements
for the Degree of

DOCTOR OF PHILOSOPHY

THE UNIVERSITY OF TEXAS AT AUSTIN
May 2011

Dedicated to my wife Carrie.

Acknowledgments

The research presented in this dissertation would not be possible without the direction of my adviser, Professor Gennady Shvets. He has a seemingly infinite supply of new and exciting research ideas, and always looks beyond the first layer of results for deeper, more meaningful physics. I would like to thank additional individuals that contributed to this work in significant ways. Dr. Dmitriy Korobkin joined the group one year before I did, and until his departure in 2010, he was a tireless instructor and persevering research scientist. I thank fellow group members Chris Fietz, Chihhui Wu, Hossein Mousavi, Dr. Alexander Khanikaev, and Dr. Yoav Avitzour for their willingness to help answer any and all questions, as well as their substantial contribution to our collaborative research efforts. I also thank Dr. Yaroslav Urzhumov and Dr. Serguei Kalmykov; without their dedication, most of our group's first experimental projects would have never achieved success. More recently, the experimental support provided by Nihal Arju, Dr. David Fozdar, and Dr. Kamil Alici has helped me greatly.

At twelve years old, all children in the sixth grade were asked to record what we wanted to be when we grew up. Instead of following the majority of the male students by responding with the name of a professional sports team, I simply replied "physicist." Nearly two decades later, and "grown up" with a

child of my own, I know I've been blessed by God to have been given the ability and opportunity to see my dream through to reality. I may not study the black hole singularities that originally sparked my interest, but the excitement remains. I thank my parents for always demanding my best effort, and for encouraging my scientific curiosity. Lastly, but most importantly, my wife Carrie has supported me since I studied upper-level undergraduate physics at the University of Illinois at Urbana-Champaign, when I applied for graduate school, through my enrollment and doctoral candidacy at the University of Texas at Austin, and to the conclusion of this difficult but rewarding and life-changing academic journey.

Controlling Infrared Radiation with Subwavelength Metamaterials and Silicon Carbide

Publication No. ____________________

Burton Hamilton Neuner III, Ph.D.
The University of Texas at Austin, 2011

Supervisor: Gennady Shvets

The control and manipulation of infrared (IR) radiation beyond the capabilities of natural materials using silicon carbide (SiC), metamaterials, or a combination thereof, is presented. Control is first demonstrated using SiC, a polar crystal that exhibits a dielectric permittivity less than zero in the mid-IR range, through the excitation of tightly confined surface phonon-polaritons (SPPs), thus enabling a multitude of applications not possible with conventional dielectrics. Optimal, or critical coupling to SPPs is explored in SiC films through Otto-configuration attenuated total reflection. One practical application based on Otto-coupled SPPs is presented: IR refractive index sensing is shown for three pL-scale fluid analytes. It is then demonstrated that when two SiC films are brought to a few-micron separation, IR radiation can excite surface modes that possess phase velocities near the speed of light, a property required for efficient table-top particle accelerators. Metamaterials are engineered with subwavelength structure and possess optical properties not found in nature. Two such metamaterials will be introduced: metal films perforated with arrays of rectangular holes display the ability to control IR light polarization through spoof surface plasmon excitation, and metal/dielectric multilayers patterned with subwavelength-pitch corrugations display frequency-tunable, wide-angle, perfect IR absorption. Two experiments, which have implications in polarization control and thermal emission, combine the benefits of SiC with those of metamaterials: extraordinary optical transmission and absorption are observed in SiC hole arrays, and the design of individual SiC antennas permits the control of the bulk metamaterial responses of impedance and absorption/emission. Finally, a new optical beamline based on Fourier transform IR spectroscopy was designed, built, characterized, and implemented, serving as the major experimental objective of this dissertation. The novel beamline, which confines radiation to a 200-micron diameter and enables angle-dependent IR spectroscopy, was verified using multiple metamaterial structures.

Table of Contents

List of Abbreviations

ATR	Attenuated total reflection
BS	Beamsplitter
CVD	Chemical vapor deposition
CW	Continuous wave
EBL	Electron beam lithography
EM	Electromagnetic
EOA	Extraordinary optical absorption
EOT	Extraordinary optical transmission
FIB	Focused ion beam
FTIR	Fourier transform infrared (spectroscopy)
ICP	Inductively coupled plasma
IR	Infrared
NA	Numerical aperture
OAP	Off-axis parabolic (mirror)
PEC	Perfect electric conductor
PECVD	Plasma-enhanced chemical vapor deposition
PV	Photovoltaic
QS	Quasi-static
rf	Radio frequency
SEM	Scanning electron microscope
S-FIL	Step and flash imprint lithography
SPP	Surface plasmon- or phonon-polariton
SPR	Surface plasmon resonance
SSP	Spoof surface plasmon
SW	Surface wave
SWABSiC	Surface wave accelerator based on SiC
TE	Transverse electric
TIR	Total internal reflection
TM	Transverse magnetic
TPV	Thermophotovoltaic
UV	Ultraviolet

List of Tables

List of Figures

Chapter 1

Introduction

1.1 Visible and Infrared Light Control through Surface Wave Excitation: a Recent Perspective

In the last decade, tremendous attention has been paid to surface plasmon/phonon-polaritons [84] because the resulting intense, localized electromagnetic fields enable a multitude of applications, one of the most popular of which being the refractive index analyte sensor [86]. Surface plasmon/phonon-polaritons (SPPs) are electromagnetic waves tightly confined to the interface between polaritonic ($\epsilon_p < 0$) and dielectric ($\epsilon_d > 0$) materials. Negative permittivity ϵ can result from (i) the collective oscillation of conduction electrons (plasmons) in metals such as gold (Au) and silver (Ag) [84, 7] or (ii) lattice vibrations (phonons) in polar crystals such as silicon carbide (SiC), zinc selenide (ZnSe), and indium phosphide (InP) [46].

Surface plasmons are typically excited by visible-range and near-infrared-range photons, while surface phonons generally exist in the mid-infrared range. In both cases, the nature of the excitation is such that the incident light source alone is not sufficient to excite the mode (i.e., the longitudinal wavevector is too small). Therefore, a coupling method is required. When prism couplers are used, applications such as index sensing are made possible [24]. One dimensional gratings can also be used to excite SPPs, enabling highly efficient thermal emission sources [37]. And two dimensional structures enable such applications as enhanced biosensing that exploits Ni-mesh extraordinary infrared (IR) transmission [116].

Many other exotic physical phenomena and applications are made possible by the control of surface modes and electric field enhancement, which include ultraviolet [30] and mid-IR [104] sub-diffraction-limited superlensing, surface wave particle acceleration [54], negative index materials [96], impedance-matched perfect absorbers [5], and IR emission from SiC antennas [90].

A majority of surface polariton work has been focused on visible- and near-IR-range surface plasmons, primarily because there are many applications of interest in those ranges, and, to a lesser extent, noble metals permit less complex fabrication and are more readily available than high-quality polar crystals. Historically, the mid-IR spectrum has been used in applications that include chemical spectroscopy and medical diagnostics because of analyte specificity (larger differences in refractive index, n) and molecular fingerprints that exist in the mid-IR range. Recently, interest has grown in using such resonant phenomena to improve upon mid-IR applications such as pathogen sensing based on biofunctionalized films [33] and gas index sensing based on surface excitation in Ti/Au layers [42]. In many such applications, metamaterials—which are artificially engineered materials with subwavelength periodic structure—are used to achieve the desired resonance.

This dissertation work presents diverse methods demonstrated to understand, control, and apply IR SPPs using polar crystalline SiC, subwavelength metamaterials, or a combination of both. The major experimental advancement of this work was the design, implementation, characterization, and usage of a novel beamline based on Fourier transform infrared (FTIR) spectroscopy that allows for angle-resolved and polarization-controlled IR optical analysis of samples as small as 200 μm in diameter. In the next section, the organization for this dissertation will be presented.

1.2 Organization of the Research to Follow

In Chapter 2, critical coupling to SiC SPPs is presented. This coupling is enabled and observed by Otto-configuration attenuated total reflection (ATR) of mid-IR radiation. Reflectance measurements demonstrate critical coupling, which is a maximal coupling of incident radiation to surface modes, by a double-scan of wavelength and incidence angle. Critical coupling results in maximal electric field enhancement and occurs when radiative prism coupling loss is equal to resistive loss in SiC and radiative leakage into the substrate.

One experimental application for Otto-configuration SPP excitation is detailed in Chapter 3, where it is demonstrated that pL-scale analyte index sensing is enabled in the mid-IR by surface modes supported at the SiC/analyte interface. Attenuated total reflectance measurements reveal analyte index specificity through a double-scan of wavelength and incidence angle for fluid volumes as small as 100 pL. Three fluid analytes—air, mineral oil, and silicone oil—are used in laser experiments to demonstrate the sensor's capabilities.

The experiments of Chapters 2 and 3 probed SPP physics of smooth SiC surfaces; it is shown in Chapter 4 that perforated SiC membranes can be used for engineering advanced optical properties of metamaterials in the IR range. The complex-valued, frequency-dependent, effective dielectric permittivity ($\epsilon_{\text{eff}}(\omega)$) of a membrane can be controlled by the size and spacing between the holes. Regions of anomalous dispersion and strong absorption described by $\epsilon_{\text{eff}}(\omega)$ are identified and related to the excitation of SPPs of a smooth SiC film. The effective permittivity description is validated by comparing the transmittance and absorbance of the film obtained from $\epsilon_{\text{eff}}(\omega)$ with that calculated using electromagnetic simulations. Theoretical predictions of enhanced transmission and absorption in the perforated film are experimentally verified using FTIR micro-spectroscopy.

Whether an application employs surface plasmon-polaritons or surface phonon-polaritons, the electric permittivity ϵ (where $\epsilon = n^2$) of the medium must be (i) less than zero and (ii) not too large. When $\epsilon \to -\infty$, the material is considered a perfect electric conductor (PEC), which typically occurs in metals for IR frequencies, and electromagnetic (EM) control becomes difficult. But engineering the optical response of metals in the IR range is still possible using *spoof* surface plasmons, which are controlled not by permittivity but through surface corrugations or perforations. Furthermore, by engineering the structures properly, advanced control over such properties as polarization can be gained. It is shown in Chapter 5 that spoof surface plasmon modes with engineered polarization states—e.g., planar chirality—are predicted to exist in perforated PEC surfaces. The excitation of these modes is experimentally confirmed by performing cross-polarized FTIR micro-spectroscopy, resulting in enhanced transmission when polarization rotation occurs in the structure.

As a complimentary structure to holes perforated in polaritonic media (Chapters 4 and 5), metamaterials can be fabricated such that only the subwavelength object remains, resulting in periodic antenna arrays. In Chapter 6, it is presented that by engineering the resonances of individual subwavelength IR antennas, better control over the metamaterial properties of impedance and absorption is achieved: (i) cutting long antennas to subwavelength size permits impedance matching by suppressing electromagnetic scattering, and (ii) large, tunable absorption is generated from bianisotropic resonances of the asymmetric antenna/pedestal structure. These designer modes are verified with a novel metal-free metamaterial array of subwavelength SiC antennas that exhibits electric, magnetic, and bianisotropic modes in regions of large positive and negative permittivity. The promise of using such antennas as emissive IR materials is verified by emission spectroscopy, which, through Kirchhoff's law of emission, exhibits agreement with FTIR absorption spectroscopy.

The experiments of Chapters 4, 5, and 6 relied primarily on FTIR micro-spectroscopy, a method that combines the wide frequency range of the FTIR spectrometer with the tight focusing capability of the IR microscope. This method a powerful for analyzing optical metamaterials, but it has limitations, which include a fixed angle of incidence and an atypical convergent beam profile. The former limits the tool's utility in angle-dependent studies, while the latter leads to spectral differences not easily accounted for by theory. Chapter 7 presents the benefits, limitations, and characteristics of FTIR spectroscopy using the IR microscope.

To remedy the problems encountered with the microscope, a new optical beamline external to the FTIR mainframe was proposed: the development and implementation of the new apparatus served as the major experimental objective of this dissertation work. In Chapter 8, the external beamline and its characterization will be presented in detail. Despite the presence of chromatic aberration, a 200-μm spot size is achieved. Numerical renormalization compensates for chromatic aberration, even permitting the analysis of samples smaller than 200 μm by accounting for beam/substrate interaction. Angle-dependent spectroscopy of small-area metamaterials is verified using an array of Au antenna pairs. The external beamline will then be used to analyze the angle-sensitive experiments of Chapters 9 and 10 in detail.

Chapter 9 presents a device whose design requires analysis over a broad angle range—the two dimensional, ultra-thin, wide-angle perfect IR absorber. The geometry of the structure is simple enough to be realized over areas larger than (1 mm)^2 with present fabrication techniques (step and flash imprint lithography), and is numerically shown to exhibit absorption of nearly 100 percent at the resonant wavelength. Peak absorption is spectrally tunable by adjusting geometric parameters and material choice. The angular dependence of absorption for different incident radiation polarizations is experimentally demonstrated, remaining above 90 percent with p polarization for incidence angles up to 80°, and above 75 percent with s polarization up to 45°.

Finally, an application based on multilayer SPP excitation is presented in Chapter 10. The Surface Wave Accelerator Based on SiC (SWABSiC) is a compact, near-field, solid-state accelerating structure that can be powered by a carbon dioxide laser, and it supports two transverse magnetic (TM) modes—a sub-luminous ($v_{ph_x} < c$) mode and an *accelerating* luminous ($v_{ph_x} \sim c$) mode. These surface waves are excited in a few-micron-wide evacuated planar channel between two SiC films grown on silicon (Si) slabs. The Si slab is fabricated into a triangular prism and coupling to the mode is accomplished by illuminating the structure with the light source through one of the prism facets. Super-luminous and sub-luminous modes are experimentally demonstrated with both the laser and external beam FTIR optical setups. While the laser provides strong incident power (and a correspondingly high signal-to-noise ratio), it is limited in the number of frequencies it can deliver. The external FTIR beamline provides broadband IR coverage and variable incident angles, but is limited by power and beam divergence. Two dimensional color plots will show mode evolution via reflectivity over incident angle and frequency space for both methods.

Chapter 2

Critical Coupling to Surface Phonon-Polaritons in Silicon Carbide

2.1 Introduction

As a result of their tight confinement to the metal/dielectric interface and their sensitivity to the surrounding dielectric permittivity ϵ_d, surface plasmon-polaritons [84, 7] have been employed for resonant index sensing using visible light in applications that include detecting the adsorption of atomic-layer films [36]. The extension of this technique into the mid-infrared (mid-IR) using surface phonon-polaritons has great potential in spectroscopic "fingerprint" identification but has not been widely implemented. Beyond sensing [33], mid-IR SPPs find diverse applications that include highly efficient thermal emission [37], surface wave particle acceleration [54], and near-field superlensing [104].

The SPP propagation wavenumber k_{SPP} (which will be given by Eq. 2.14) implies that $k_{\mathrm{SPP}} > \omega/c$, where $\omega = 2\pi c/\lambda$, and λ is the vacuum wavelength of light. Since the SPP wavenumber is larger than that provided by incident radiation, auxiliary coupling devices such as gratings or high-index prisms are necessary to excite surface waves [84]. When a dielectric prism is used, either

Otto [77] configuration or Kretschmann configuration is employed. Otto coupling is the focus of this work; Fig. 2.1 presents a schematic of this method. Regardless of the coupling method, it is desirable to couple a maximal amount of incident radiation into SPPs. The complete coupling of laser energy to SPPs—*critical coupling*—results in vanishing reflectivity ($R \rightarrow 0$) and the largest enhancement of the SPP electric field over the incident laser field E_0.

By using SiC films grown on a silicon (Si) substrate, critical coupling to SPPs is theoretically described and experimentally demonstrated. The dispersion relation for the complex propagation constant k_{free} of a freely propagating leaky and lossy SPP is solved and it is demonstrated that critical coupling is achieved when the energy loss of the *free* SPP into the prism (radiative coupling) is equal to the sum of all other losses (resistive loss and substrate leakage). Finally, by conducting a double-scan of incident angle (θ) and wavelength (λ) for two subwavelength air gaps, critical coupling of incident radiation to SPPs in the Otto configuration is experimentally demonstrated. The SPP modes are excited by the Otto-coupling method, and their presence is measured by attenuated total reflection (ATR) of p-polarized (TM) radiation, where light evanescently couples through the gap.

Theoretically, for every wavelength satisfying $\epsilon_{\text{SiC}}(\lambda) < 0$, there exists a small gap d_{gap} (typically <10 μm) and an incidence angle θ_0 for which reflectivity $R(\lambda_0, \theta_0, d_{gap}) = 0$, which corresponds to critical coupling. Experimentally, $R = 0$ is usually unattainable because of the radiation source's finite angular spread. Therefore, critical coupling is experimentally deduced from

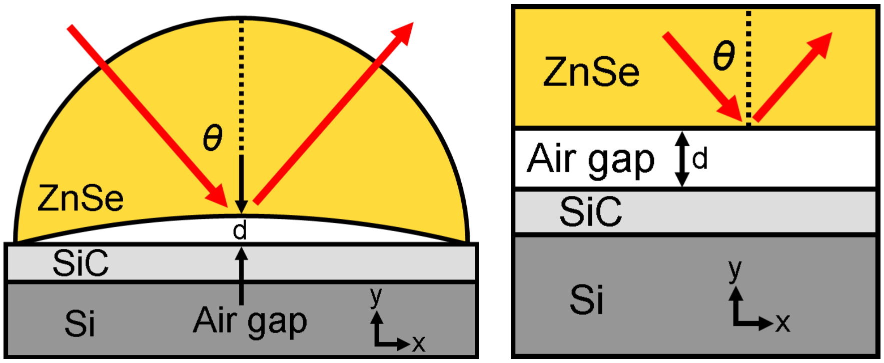

Figure 2.1: (Left) Experimental and (right) theoretical setup schematics are given as 2D depictions (not to scale). In the laboratory, incident light is coupled through a hemispherical ZnSe prism to the air gap/SiC surface where surface phonon polaritons are excited. Analytical theory models the structure as a 1D multilayer of four materials (ZnSe/air/SiC/Si) with realistic thicknesses and optical properties.

the global minimum of $R(\lambda, \theta)$ for each d_{gap}. While the excitation of mid-IR SPPs has been measured by scanning λ [106, 60, 17, 73] or by scanning d_{gap} and θ [32, 14], the demonstration of critical coupling to SPPs—which requires a double-scan of both λ and θ—has not been fully explored.

In this work, spectroscopic experiments were performed by the author and Dmitriy Korobkin, theoretical calculations and numerical modeling were derived by Chris Fietz, numerical SPP calculations and interferometric fitting were performed by the author, and sample growth was performed by University Claude Bernard Lyon I collaborator Gabriel Ferro.

2.2 Theoretical Description of Surface Polaritons

The dielectric permittivity ϵ describes how a material will respond to an incident electric field; matter with $\epsilon > 0$ polarizes in the same direction as $\mathbf{E}$, whereas matter with $\epsilon < 0$ polarizes in the opposite direction to $\mathbf{E}$. Metals and polar crystals exhibit negative permittivity in certain frequency ranges; $\epsilon < 0$ occurs in metals for frequencies below the plasma frequency and in polar crystals for frequencies between the transverse and longitudinal optical (TO and LO) phonon modes (the *reststrahlen* band). Free electron gas oscillation is responsible for the metal's "plasmonic" behavior, while TO and LO phonon resonances are responsible for the polar crystal's "phononic" behavior. The coupling of photon radiation to surface excitations are classified as polaritons. Such coupling at one interface is now reviewed (SPP excitation in a multilayer consisting of two SiC films will be presented in Ch. 10).

2.2.1 Electromagnetic Surface Waves at a Single Interface

The surface plasmon- or phonon-polariton dispersion relation is presented in Ref. [84]. This unique excitation is possible at the interface between materials that possess dielectric permittivity of opposite sign. While the physical mechanisms behind $\epsilon < 0$ exhibited by Au and SiC differ, EM dispersion is the same, depending only on the material's frequency-dependent optical properties.

The surface excitation presented here occurs at an interface between two nonmagnetic media with dielectric permittivity functions $\epsilon_1(\omega)$ and $\epsilon_2(\omega)$,

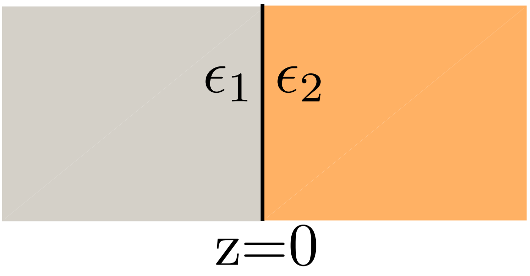

Figure 2.2: Two materials with semi-infinite thickness and dielectric permittivity functions ϵ_1 and ϵ_2 separated by a single interface at $z = 0$.

separated by an interface at $z = 0$, as depicted in Fig. 2.2. To begin, Maxwell's electromagnetic equations [51] are given as

$$\nabla \times \mathbf{H}_i = \epsilon_i \frac{1}{c}\frac{\partial}{\partial t}\mathbf{E}_i, \tag{2.1}$$

$$\nabla \times \mathbf{E}_i = -\frac{1}{c}\frac{\partial}{\partial t}\mathbf{H}_i, \tag{2.2}$$

$$\nabla \cdot (\epsilon_i \mathbf{E}_i) = 0, \tag{2.3}$$

and

$$\nabla \cdot \mathbf{H}_i = 0, \tag{2.4}$$

where i denotes the media in which equations are being solved: $z < 0$ and $\epsilon_i = \epsilon_1$ when $i = 1$, and $z > 0$ and $\epsilon_i = \epsilon_2$ when $i = 2$.

Solutions of Maxwell's equations are classified into s- and p-polarized modes, where the electric field $\mathbf{E}$ and the magnetic field $\mathbf{H}$ are parallel to the interface, respectively. Waves propagating along the interface must then possess a component of electric field that is perpendicular to the surface, so p polarization must be used. The mode propagates along the interface ($z = 0$)

in the x direction, and fields evanescently decay out of the surface (i.e., for $z > 0$ or $z < 0$), leading to the following:

$$\mathbf{E}_i = (E_{ix}, 0, E_{iz})e^{-\kappa_i|z|}e^{i(k_i x-\omega t)} \tag{2.5}$$

and

$$\mathbf{H}_i = (0, E_{iy}, 0)e^{-\kappa_i|z|}e^{i(k_i x-\omega t)}, \tag{2.6}$$

where k_i is the magnitude of the propagation wavevector parallel to the interface. Introducing the field Equations 2.5 and 2.6 into Equations 2.1–2.4, it can be found that the following result:

$$i\kappa_1 H_{1y} = +\frac{\omega}{c}\epsilon_1 E_{1x}, \tag{2.7}$$

$$i\kappa_2 H_{2y} = -\frac{\omega}{c}\epsilon_2 E_{2x}, \tag{2.8}$$

and

$$\kappa_i = \sqrt{k_i^2 - \epsilon_i \frac{\omega^2}{c^2}}. \tag{2.9}$$

The electric displacement must be equal on both sides of the interface. Also, fields tangential to the surface must be continuous. Using Eqs. 2.7 and 2.8, it is found, following these two boundary conditions, that

$$\frac{\kappa_1}{\epsilon_1}\mathbf{H}_{1y} + \frac{\kappa_2}{\epsilon_2}\mathbf{H}_{2y} = 0\bigg|_{z=0} \tag{2.10}$$

and

$$\mathbf{H}_{1y} = \mathbf{H}_{2y}\big|_{z=0}\,, \tag{2.11}$$

respectively. The surface polariton condition is then found through Eqs. 2.10 and 2.11 to be

$$\frac{\epsilon_1}{\kappa_1} + \frac{\epsilon_2}{\kappa_2} = 0. \tag{2.12}$$

Applying the same boundary conditions to the wavevector $\mathbf{k}$ from Eq. 2.9 results in $k_1 = k_2 = k$. Finally, the surface polariton wavevector dispersion can be presented in a more intuitive, frequency-dependent form [84]:

$$k(\omega) = \frac{\omega}{c}\sqrt{\frac{\epsilon_1\epsilon_2}{\epsilon_1 + \epsilon_2}}. \tag{2.13}$$

The factor ω/c represents the magnitude of the free-space radiation wavevector.

Relating this result to the mid-IR material SiC simply requires replacing the general permittivities ϵ_i with those of SiC and air:

$$k_{\mathrm{SPP}}(\omega) = \frac{\omega}{c}\sqrt{\frac{\epsilon_{\mathrm{SiC}}\epsilon_0}{\epsilon_{\mathrm{SiC}} + \epsilon_0}}. \tag{2.14}$$

For air, $\epsilon_0 = 1$, and the standard equation for polar crystals describes SiC permittivity [35]:

$$\epsilon_{\mathrm{SiC}}(\omega) = \epsilon_\infty \frac{\omega^2 - \omega_{LO}^2 + i\gamma\omega}{\omega^2 - \omega_{TO}^2 + i\gamma\omega}, \tag{2.15}$$

where $\omega_{LO} = 972$ cm^{-1} ($\lambda_{LO} = 10.288$ μm), $\omega_{TO} = 796$ cm^{-1} ($\lambda_{TO} = 12.563$ μm), $\gamma = 3.75$ cm^{-1}, and $\epsilon_\infty = 6.5$ fit T and R data for a 1.5 μm air-bridged membrane. Characterization details will be discussed in Ch. 4 and are published in Ref. [108].

Mode excitation requires wavevector matching by external methods such as prisms or gratings. A prism is used in this work, and the dielectric prism dispersion relation [84] is

$$k_x = \frac{\omega}{c}\sqrt{\epsilon_{\mathrm{ZnSe}}}\sin\theta, \tag{2.16}$$

where k_x describes the prism dispersion light line. Efficient, evanescent coupling to SPPs through the high-index ZnSe hemispherical prism ($\epsilon_{\mathrm{ZnSe}} = 5.76$) occurs when $k_x \approx \mathrm{Re}\left(k_{\mathrm{SPP}}\right)$, and can be calculated by setting Eq. 2.14 equal to Eq. 2.16. The SPP dispersion curve $\omega\left(k_{\mathrm{SPP}}\right)$ and prism light lines $\omega\left(k_x\right)$ are shown in Fig. 2.3, and satisfy excitation criteria where intersecting. This simple argument is qualitative because (i) it does not account for the finite thickness of SiC or the SPP's leakage into the Si substrate, (ii) the coupling prism's proximity to the SiC surface is not considered, and (iii) the SPP's excitation efficiency is not quantified.

2.2.2 Dispersion that Accounts for Radiative and Resistive Losses

To address the three limitations that exist in the single-interface SPP theory, the dispersion relation for a free SPP propagating along the air/SiC interface of a ZnSe/air/SiC/Si system is numerically solved in MATLAB, accounting for concerns (i) and (ii). Energy radiates into ZnSe and Si, contributing to SPP energy loss. The complex propagation constant is calculated as

$$k_{\mathrm{free}}(\omega) = k_{\mathrm{res}} + i\kappa, \tag{2.17}$$

where $k_{\mathrm{res}} \approx k_{\mathrm{SPP}}$ and

$$\kappa = \kappa_{\mathrm{ohm}}^{\mathrm{SiC}} + \kappa_{\mathrm{rad}}^{\mathrm{Si}} + \kappa_{\mathrm{rad}}^{\mathrm{ZnSe}}, \tag{2.18}$$

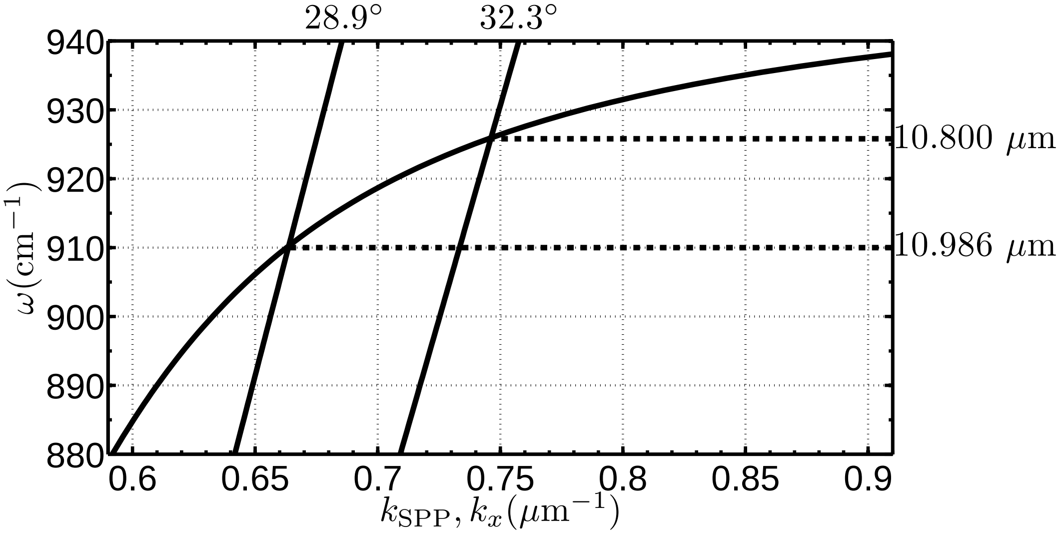

Figure 2.3: Dispersion curves correspond to k_{SPP} (Eq. 2.14; curved line) and the prism's k_x (Eq. 2.16; straight lines for the two angles as indicated above). Light lines (k_x) intersect k_{SPP} at two wavelengths, $\lambda = 10.800$ μm (accessible by CO_2 laser) and $\lambda = 10.986$ μm (inaccessible by CO_2 laser), indicating SPP excitation criteria for the two critical coupling cases.

in the limit of weak loss. The κ terms are spatial decay rates: $\kappa_{\mathrm{ohm}}^{\mathrm{SiC}}$ represents ohmic loss in SiC, and $\kappa_{\mathrm{rad}}^{\mathrm{Si}}$ and $\kappa_{\mathrm{rad}}^{\mathrm{ZnSe}}$ represent radiative leakage into Si and ZnSe, respectively. Matching the incident radiation source's k_x to k_{res} excites resonant SPPs. In the limit of weak loss, *free* SPP leakage into ZnSe is equivalent to *laser-driven* SPP coupling from ZnSe (as is the case in experiments).

Reflectivity is represented by the Lorentzian response when SPPs are laser-driven:

$$R = 1 - \frac{4\left(\kappa_{\mathrm{ohm}}^{\mathrm{SiC}} + \kappa_{\mathrm{rad}}^{\mathrm{Si}}\right)\kappa_{\mathrm{rad}}^{\mathrm{ZnSe}}}{\left(k_x - k_{\mathrm{res}}\right)^2 + \left(\kappa_{\mathrm{ohm}}^{\mathrm{SiC}} + \kappa_{\mathrm{rad}}^{\mathrm{Si}} + \kappa_{\mathrm{rad}}^{\mathrm{ZnSe}}\right)^2}, \tag{2.19}$$

in the limit of weak loss and when θ is such that $k_x \approx k_{\mathrm{res}}$. The derivation of a

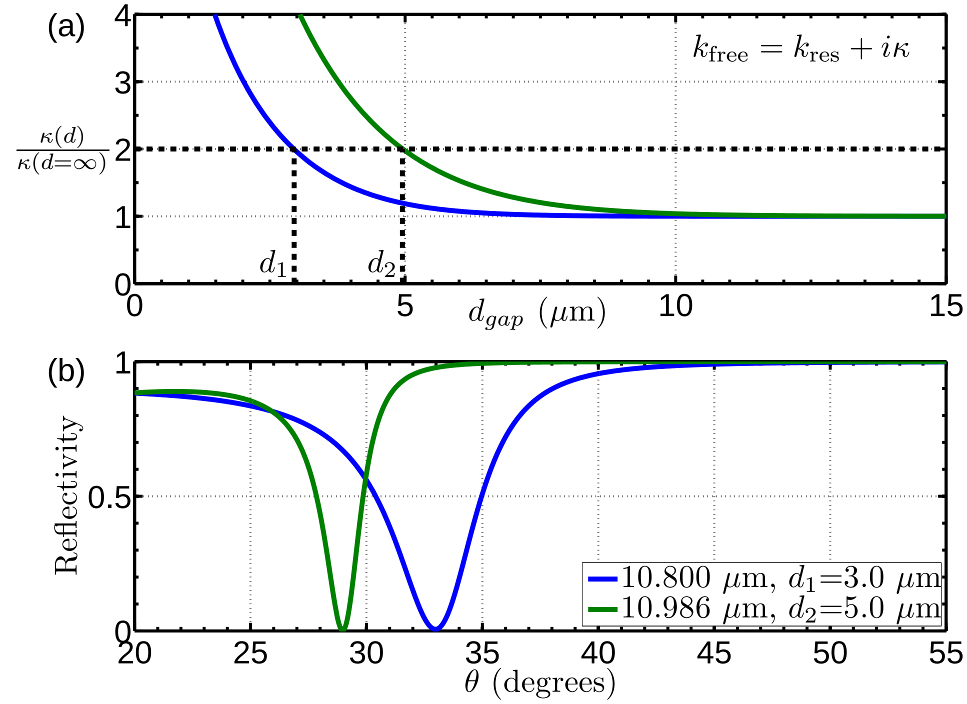

Figure 2.4: (a) k_{free} is the SPP in-plane wavenumber; the imaginary part of k_{free}, $\kappa(d)$, is normalized to $\kappa(d = \infty)$. Critical coupling occurs when coupling loss into the prism ($\kappa_{\text{rad}}^{\text{ZnSe}}$) is equal to losses in SiC ($\kappa_{\text{ohm}}^{\text{SiC}}$) and the Si substrate ($\kappa_{\text{rad}}^{\text{Si}}$) combined, which is shown graphically as $\kappa(d) = 2\kappa(d = \infty)$. (b) Reflectivity R vs. θ is plotted for two laser-driven SPPs, each with an air gap that satisfies critical coupling criteria. SPP attenuation rates $\kappa(d = \infty) = \kappa_{\text{ohm}}^{\text{SiC}} + \kappa_{\text{rad}}^{\text{Si}} = 22$ and 10 mm^{-1} for $\lambda_{1,2} = 10.800$ and 10.986 μm, respectively.

similar response in a three-layer, metal-based plasmonic system can be found in Ref. [84].

Critical coupling, which is accompanied by zero reflectivity, occurs when

$$\kappa_{\text{rad}}^{\text{ZnSe}} = \kappa_{\text{ohm}}^{\text{SiC}} + \kappa_{\text{rad}}^{\text{Si}}. \tag{2.20}$$

Any solution of the dispersion relation for a fixed wavelength yields a single decay rate κ. Separate $\kappa_{\text{rad}}^{\text{ZnSe}}$ and $\kappa_{\text{ohm}}^{\text{SiC}}+\kappa_{\text{rad}}^{\text{Si}}$ can be extracted by varying d_{gap} and by knowing that for large d_{gap}, radiative loss into ZnSe vanishes, resulting in

$$\kappa = \kappa_{\text{ohm}}^{\text{SiC}} + \kappa_{\text{rad}}^{\text{Si}}. \tag{2.21}$$

Therefore, to find the correct gap for critical coupling, d_{gap} is varied until the imaginary part of k_{free} is twice its value for infinitely large gaps: $\kappa(d) = 2\kappa(d = \infty)$. According to Eq. 2.19, this specific gap $d_{gap}(\lambda_0)$ corresponds to the critical coupling case. The decay rate $\kappa(d)$ is shown in Fig. 2.4 (a) for two wavelengths, enabling the identification of critical coupling gaps $d_{1,2}$. Next, the laser-driven solution is obtained as a function of θ for $d_{1,2}$ by assuming light incident from the ZnSe side. As shown in Fig. 2.4 (b), reflectivity indeed vanishes for $d_{1,2}$, corresponding to critical coupling.

2.3 Infrared Spectroscopy of Critically Coupled SPPs

To demonstrate critical coupling, ATR measurements were used to detect SPPs excited in the Otto configuration [69], shown in the left panel of Fig. 2.1. The 1.5-μm 3C-SiC film was grown on a Si(100) substrate by a two-step atmospheric pressure chemical vapor deposition (CVD). Substrate carbonization was achieved under propane at 1150°C, which was then followed by epitaxial growth using a silane/propane mixture at 1350°C [43]. The growth rate was 3 μm/hour. In the laboratory, infrared radiation from a line-tunable continuous wave (CW) $^{13}CO_2$ laser was coupled through the hemispherical, 2.5-cm-diameter ZnSe prism, which was aligned in close proximity to SiC to allow for finite air gaps. The laser tunability ranges are 10.666 μm–10.867 μm (R branch) and 11.025 μm–11.310 μm (P branch). Incident and reflected radiation intensity were measured using a laser power meter (5-percent accuracy). A rotation stage provided angular steps of 0.5° for the target.

2.3.1 Gap Determination by Visible-Range HeNe Fabry-Perot Interferometry

Two air gaps were used: $d_1 = 3$ μm and $d_2 = 5$ μm. Rather than fitting IR spectral data to theory to determine gap distance, the spectral theory stands alone and instead visible laser light was used to find the gap size. The distance was determined *in situ* by HeNe laser (632.8 nm) Fabry-Perot interferometry (50-nm accuracy) because the ZnSe coupling prism is transparent to both visible and IR radiation. The same 1D MATLAB code used for theory was used for visible-range interferometry by replacing the IR dielectric functions for ZnSe, SiC, and Si with those valid in the visible range. In the lab, the prism/sample multilayer was aligned at $\theta_i < \theta_{crit}$, where θ_{crit} is the prism's critical angle. For a hemispherical ZnSe prism, $\theta_{crit} = 24.6°$. The only observables required were the angular reflection minima positions. These minima were then compared to theoretical reflection minima (as seen in Fig. 2.5) in a least-squared minimizing routine run in MATLAB. The result yielded a dielectric (air) Otto-configuration gap d. Accuracy was determined by finding the next computed local minimum, typically occurring 50 nm from either side of the global minimum result.

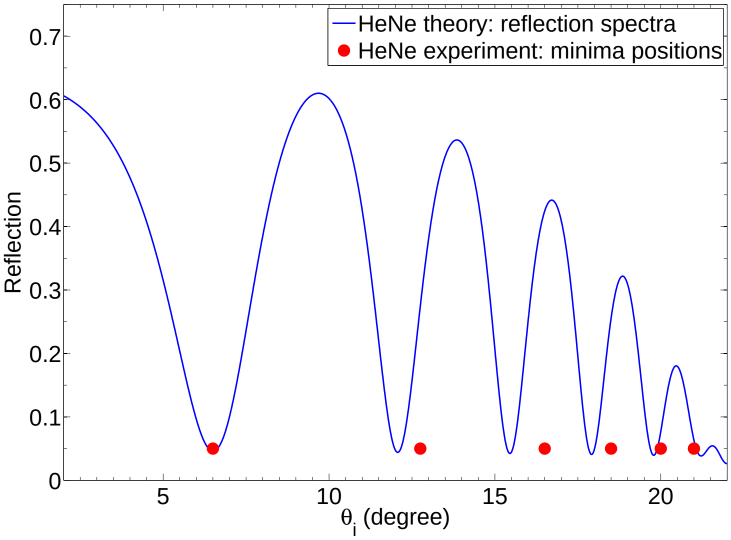

Figure 2.5: Helium-neon (HeNe, $\lambda = 632.8$ nm) visible-range laser reflection theory and experimental minima that result from thin-dielectric Fabry-Perot interferometry. The two minima sets are passed to a least-squared minimizing routine in MATLAB, yielding a dielectric (air) Otto configuration gap of $d = 3$ μm, with 50 nm accuracy.

2.3.2 Experimental Results and Discussion

In the first experiment, reflection spectra were collected for $d_2 = 5$ μm, shown in Fig. 2.6 (a) [69]. The experimental reflectivity R never falls below 30 percent, and R reaches its minimum at the boundaries of the laser tunability ranges. This implies that critical coupling for d_2 is never fully achieved because the corresponding λ_2 is not accessible to the laser. The physical interpretation is that for the laser's 10-μm R branch, short-range SPPs are under-coupled (coupling from ZnSe less than other losses), whereas for the 11-μm P branch, long-range SPPs are over-coupled (coupling from ZnSe larger

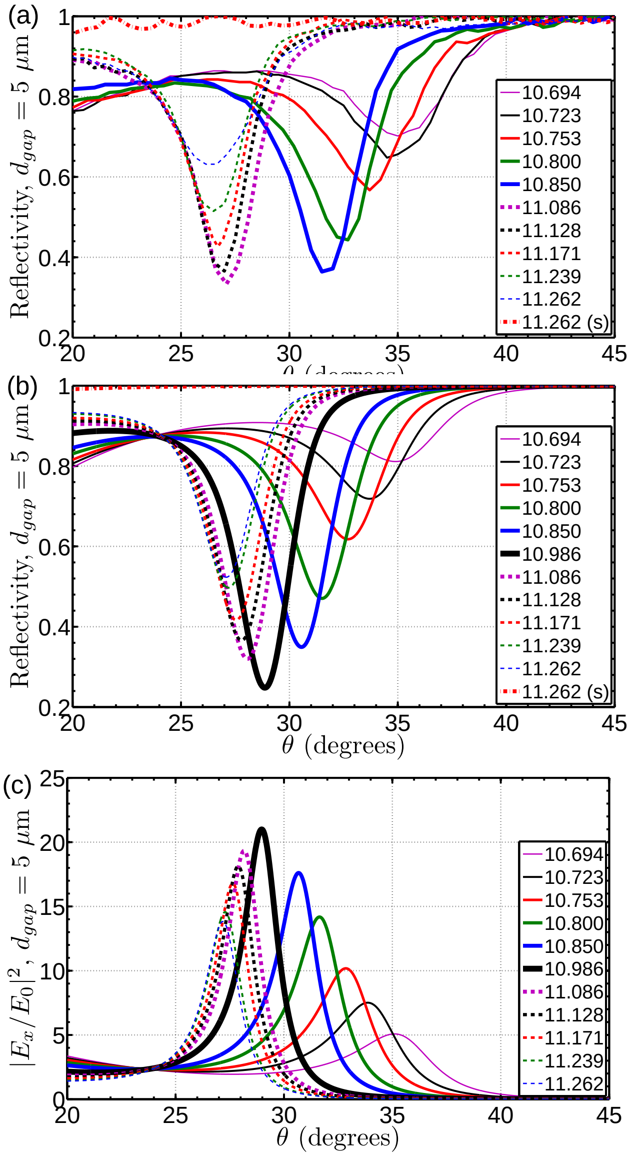

Figure 2.6: (a) Experimental and (b) theoretical plots of laser reflectivity vs. θ for the Otto configuration with air gap $d_2 = 5$ μm; s-polarized (TE) reflectivity spectra included. (c) Theoretical field enhancement $|E_x/E_0|^2$ in the plane of SiC. Critical coupling was not observed because of laser tunability, but the trend is clear and predicted for $\lambda_2 = 10.986$ μm (shown in (b,c)).

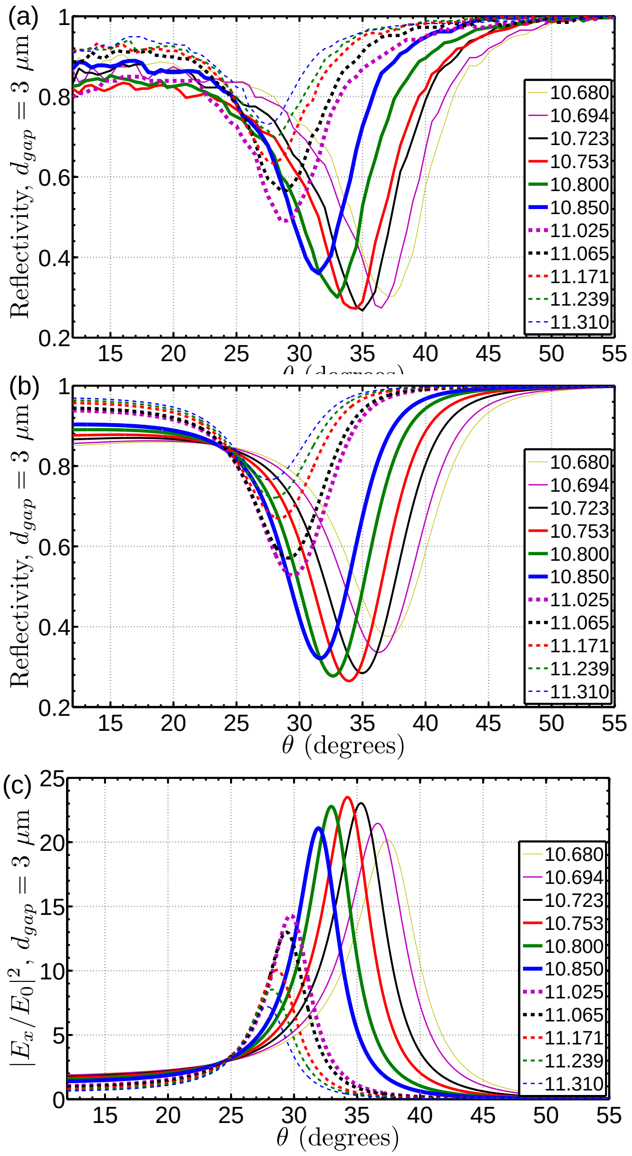

Figure 2.7: (a) Experimental and (b) theoretical plots of laser reflectivity vs. θ for the Otto configuration with air gap $d_1 = 3\ \mu$m. (c) Theoretical field enhancement $|E_x/E_0|^2$ in the plane of SiC. Critical coupling was observed at $\lambda_1^{\text{exp}} = 10.753\ \mu$m.

than other losses).

Numerical simulations shown in Fig. 2.6 (b) confirm that tunability prevented critical coupling: $\lambda_2 = 10.986$ μm, which is outside of the two available laser frequency branches, is given and corresponds to critical coupling. Numerical results are averaged assuming a Gaussian angular profile (2° full width half max, FWHM) that matches the experimental setup. According to simulations, the finite angular spread prevents $R = 0$, even for $\lambda = \lambda_2$. However, the global minimum of $R(\lambda_2, \theta_2)$ shown in Fig. 2.6 (b) clearly indicates critical coupling, which would be experimentally achievable with greater laser tunability. Simulations also show that critical coupling to SPPs is accompanied by a maximum electric field enhancement [84]. Figure 2.6 (c) displays the calculated field enhancement $|E_x/E_0|^2$ at the SiC/air interface, with a maximum value of 21.0 at critical coupling.

To achieve true critical coupling in the laboratory, the gap was reduced to $d_1 = 3$ μm and the system was double-scanned again; results are shown in Fig. 2.7 (a) [69]. The global reflectivity minimum at $\lambda_1^{\text{exp}} = 10.753$ μm agrees with numerical simulations shown in Fig. 2.7 (b), within the 5-percent experimental error. Plane wave (zero angular spread) calculations shown in Fig. 2.4 (b) instead predict critical coupling at $\lambda_1 = 10.800$ μm. But if angular divergence was reduced by a factor of 2.2, as was explored in simulations (not shown), the experimentally measurable global reflectivity minimum would indeed shift from λ_1^{exp} to λ_1.

2.4 Conclusions

In conclusion, the first experimental demonstration of critical coupling to mid-infrared surface phonon-polaritons at the air/SiC interface in the Otto configuration was presented. Critical coupling was observed by performing a double-scan of wavelength and incidence angle for two subwavelength air gaps. It was theoretically shown that critical coupling occurs when radiative prism coupling is equal to the sum of resistive, ohmic loss in SiC and radiative leakage into the Si substrate. Because critical coupling results in minimal reflectivity and maximal electric field enhancement, advanced mid-IR index sensing applications are made possible. One sensing application, which will be presented next in Ch. 3, takes advantage of the micron-scale Otto-configuration gap as a chamber for small-volume fluid containment.

Chapter 3

Mid-Infrared Index Sensing of pL-Scale Analytes Based on Surface Phonon-Polariton Excitation in Silicon Carbide

3.1 Introduction

Two of the most desirable features of any refractive index sensing technique are analyte index specificity and small-volume sensitivity. For decades, the mid-IR spectrum has been employed in diverse sensing applications that include biochemical spectroscopy, the detection of atmospheric pollutants, and medical diagnostic tests because of its IR analyte specificity. Molecules exhibit unique spectroscopic fingerprints in the mid-IR that are often manifested as larger refractive index differences between materials in the mid-IR than in the visible. One example is shown in Fig. 3.1, where the refractive index difference between mineral oil and silicone oil is both (i) larger than in the visible and (ii) wavelength-dependent.

There has been growing interest in using electromagnetically resonant methods to improve upon mid-IR sensing, which include biosensing that exploits Ni-mesh extraordinary infrared transmission [116], pathogen sensing based on refractive index-sensitive biofunctionalized films [33], and gas index

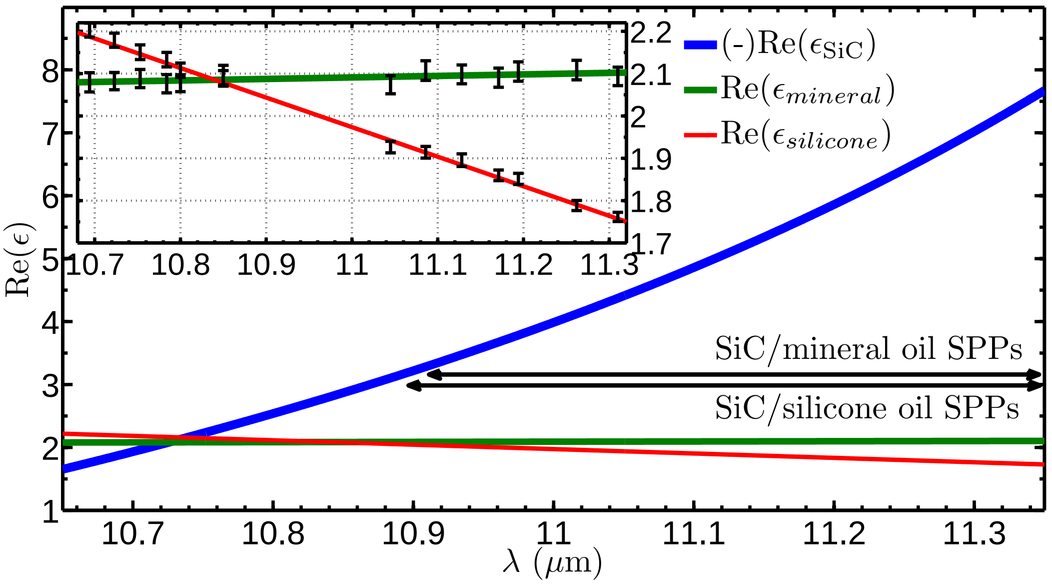

Figure 3.1: The real components of SiC, mineral oil, and silicone oil permittivity are represented by Re(ϵ_{SiC}), Re($\epsilon_{mineral}$), and Re($\epsilon_{silicone}$), and are shown for the laser's tunability range. The SPP excitation is enabled when $\epsilon_{\mathrm{SiC}} < -[\epsilon_{\mathrm{ZnSe}}\epsilon_a/(\epsilon_{\mathrm{ZnSe}} - \epsilon_a)]$, which corresponds to the ranges indicated above using mineral and silicone oils. Inset: an expanded view of $\epsilon_{mineral}$ and $\epsilon_{silicone}$; $\Delta\epsilon(11.31\ \mu\mathrm{m}) = 0.35$, which is nearly four times greater than $\Delta\epsilon(632.8\ \mathrm{nm}) = 0.09$.

sensing based on surface wave excitation in both prism-coupled Ti/Au layers [42] and SiC gratings [6]. Such resonant techniques are needed for sensing because weak vibrational modes contain detailed biomolecular information, but are difficult to resolve without electric field enhancement [116].

The desire to achieve high sensitivity with small-volume samples explains the prevalent use of surface *plasmon*-polaritons [84]; often generated by visible light, these surface excitations are tightly confined to the metal/analyte interface, and are used for such applications as the detection of atomic-layer film adsorption [36]. Surface *phonon*-polaritons (SPPs) [12], on the other hand, are supported at the polar crystal/analyte interface, and hold potential for small-volume mid-IR sensing because resonant SPPs, which are sensitive to the surrounding analyte permittivity ($\epsilon_a = n_a^2$), enhance detection capability.

Optical properties of molecules often change rapidly with frequency in the infrared, a result of characteristic vibrational modes whose intensities are both weak (CH_2 bend, C=O stretch) and strong (C–H and O–H stretch). The weak, low-frequency modes are centered in the mid-IR and contain detailed molecular information but are often difficult to resolve without the aid of surface electric field enhancement [116], one product of resonant SPP generation. Studies on IR-range, SPP-supporting polar crystals include SiC [60, 50, 108], SiO_2 [18, 17], GaN [106], AlN [73], and GaP [112]. Additionally, crystals such as SiC are robust when compared to metal, making them preferable for sensing applications that require contact with hot, abrasive, or chemically aggressive materials.

Building on the results of Ch. 2, this work shows that by exploiting SPP sensitivity to changes in incident angle (θ), vacuum wavelength (λ), gap spacing (d_{gap}), and the analyte's ϵ_a, Otto-configuration SPP spectroscopy can enable resonant, small-volume, mid-IR index sensing. The few-micron, subwavelength gap required for SPP excitation provides an ideal environment for the study of fluid analytes, and the focused laser confines light to a small region, enabling index sensing of volumes as small as 100 pL with resolution down to 1.5×10^{-3} refractive index units [48] (RIU). Sensing was experimentally implemented by performing a reflectivity (R) double-scan of θ and λ for three analytes—air, mineral oil, and silicone oil—confined in the micron-scale gap between the surface of SiC and the coupling prism.

In this work, spectroscopic experiments were performed by the author and Dmitriy Korobkin, theoretical calculations and numerical modeling were derived by Chris Fietz, numerical SPP calculations, analyte index determination, and sensitivity analysis were performed by the author, and sample growth was performed by University Claude Bernard Lyon I collaborator Gabriel Ferro.

3.2 Single-Interface SPPs and Sensitivity to Refractive Index

Resonant SPP excitation generates large electric field enhancement in the gap [69], which enables mid-IR sensing and makes the detection of weak vibrational bonds possible [116]. As reviewed in Ch. 2, SPPs are supported at the SiC/analyte interface when $\epsilon_{\mathrm{SiC}} < 0$, $\epsilon_a > 0$, and $|\epsilon_{\mathrm{SiC}}| > |\epsilon_a|$. The SPP dispersion relation [84] for this semi-infinite interface was presented in Sec. 2.2 and is restated by

$$k_{\mathrm{SPP}} = \frac{\omega}{c}\sqrt{\frac{\epsilon_{\mathrm{SiC}}\epsilon_a}{(\epsilon_{\mathrm{SiC}} + \epsilon_a)}}, \tag{3.1}$$

where fluid analyte permittivity ϵ_a replaces the air or vacuum permittivity of $\epsilon_0 = 1$.

This work employs the Otto configuration to excite SPPs, as schematically shown in Fig. 3.9 inset. The ZnSe prism, SiC film, and analyte permittivities are given by $\epsilon_{\mathrm{ZnSe}} = 5.76$, ϵ_{SiC}, and ϵ_a. The prism light line is given by Eq. 2.16, and strong evanescent coupling to SPPs through the hemispherical prism occurs when $k_x \approx \mathrm{Re}(k_{\mathrm{SPP}})$. Therefore, SiC/analyte SPPs are supported when

$$\epsilon_{\mathrm{SiC}} < -\left[\frac{\epsilon_{\mathrm{ZnSe}}\epsilon_a}{(\epsilon_{\mathrm{ZnSe}} - \epsilon_a)}\right], \tag{3.2}$$

or when $\mathrm{Re}(\epsilon_{\mathrm{SiC}}) < -3.28$ ($\lambda > 10.908$ μm) with mineral oil and $\mathrm{Re}(\epsilon_{\mathrm{SiC}}) < -3.18$ ($\lambda > 10.894$ μm) with silicone oil, in the range of Fig. 3.1.

3.3 Experimental Determination of 3C-SiC Permittivity, ϵ_{SiC}

To determine the permittivity of 3C-SiC, ϵ_{SiC}, spectra were collected from an air-bridged SiC membrane of identical composition and thickness. The 1.5-μm-thick SiC, grown as described in Sec. 2.3, was fabricated into a membrane using the following process. A 5-μm-thick layer of SiO_2 was grown on both sides of the sample to provide a hard etch mask. Ablation by 355-nm Nd:YAG laser radiation opened (1 mm)^2 etch windows in the hard-mask/residual 100-nm-SiC back side of the substrate. This process was used because SiC etching processes are not locally available. Exposed Si was anisotropically etched using a 35-percent solution of KOH at 80°C until reaching the 1.5-μm SiC film on the front side of the substrate. Residual SiO_2 was removed by a room-temperature HF buffered oxide etch. Reflection and transmission were contained to a focal-plane region of (100 μm)^2 and were collected from the resulting (350 μm)^2 SiC membrane. Transmission and reflection spec-

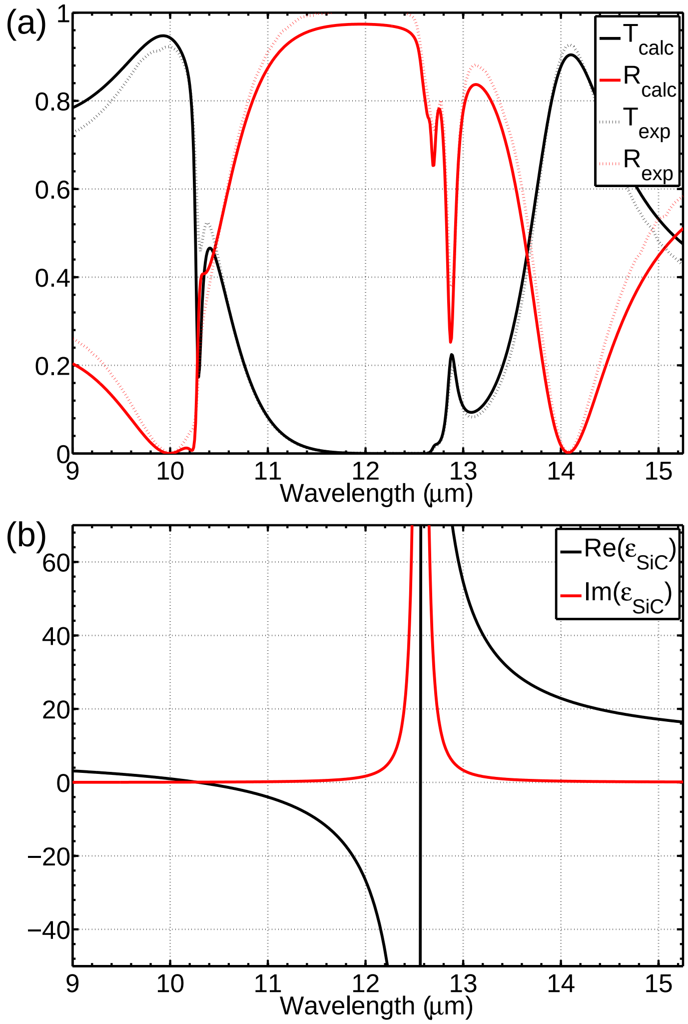

Figure 3.2: (a) FTIR micro-spectroscopy transmittance and reflectance for the 1.5-μm SiC membrane, with calculated theoretical fits. Fresnel theory fit $\mathrm{T}_{\mathrm{calc}}$ and $\mathrm{R}_{\mathrm{calc}}$ to $\mathrm{T}_{\mathrm{exp}}$ and $\mathrm{R}_{\mathrm{exp}}$ using the polaritonic function of ϵ_{SiC} given by Eq. 2.15. (b) Complex permittivity of SiC, cropped for clarity. The maximum of $\mathrm{Re}(\epsilon_{\mathrm{SiC}}) = 340$ at 12.59 μm (the minimum is -330 at 12.53 μm) and the maximum of $\mathrm{Im}(\epsilon_{\mathrm{SiC}}) = 670$ at 12.56 μm. $\mathrm{Re}(\epsilon_{\mathrm{SiC}}) = 0$ at 10.29 μm (LO phonon mode) and 12.56 μm (TO phonon mode).

tra, shown in Fig. 3.2 (a), were collected with a 2-cm^{-1} resolution by a Thermo Scientific Continuum microscope coupled to a Nicolet 6700 FTIR spectrometer. The permittivity of 3C-SiC is shown in Fig. 3.2 (b) and is represented by the polaritonic formula of Eq. 2.15.

3.4 Extracting the Complex Permittivities of Mineral and Silicone Oils

Reflectance calculations shown in Figs. 3.6, 3.7, and 3.8 required the use of known ϵ_a, but neither oil has published values available. The complex index of silicone oil was presented [38], but changes of ϵ on the sub-micron-wavelength scale are unresolvable, and the viscosity grade differs from that used in this work. Therefore, total internal reflection (TIR) experiments were performed to characterize $\epsilon_{oil} = \epsilon_r + i\epsilon_i$ for large oil depths. An oil bath was prepared by placing a 2.5-mm thick rubber gasket between a ZnSe prism and a glass slide, as depicted in the Fig. 3.3 inset. This ensured an oil depth that was effectively infinitely deep for mid-IR radiation and resulted in TIR spectra dependent on ϵ_{oil} alone (as opposed to the glass slide).

Infrared reflection spectra were collected as the prism was rotated from small angles ($\theta \geq 12°$, where reflection is low), through the TIR critical angle (where reflection becomes unity), to large angles ($\theta \leq 85°$). As shown in Fig. 3.3, spectra vary greatly for different dielectric fluids. At $\lambda = 11.31$ μm, mineral oil exhibits low optical loss, as evident by the abrupt TIR transition. Silicone oil, on the other hand, is more absorptive and exhibits a more gradual

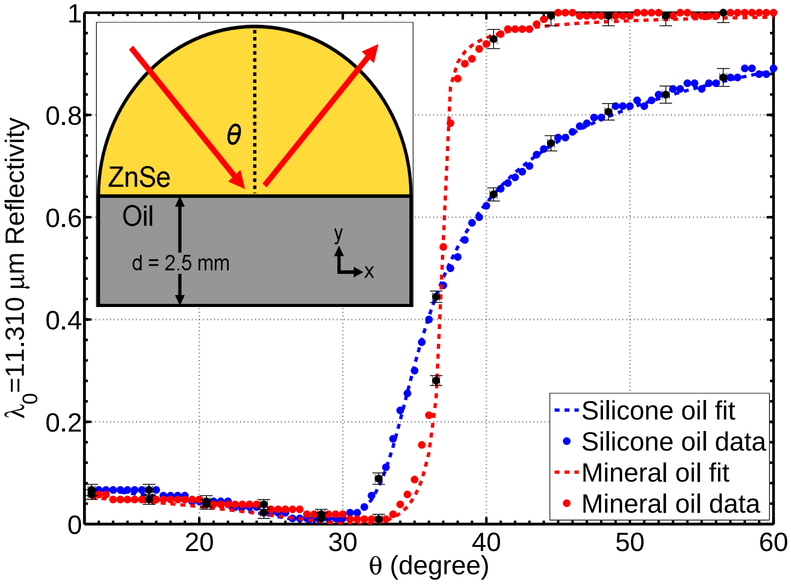

Figure 3.3: Attenuated total reflection data for mineral oil and silicone oil at $\lambda = 11.310\ \mu$m. Intensity-dependent error bars in reflectivity are sparsely shown for clarity. The error in angular measurement is $\pm 0.25°$ (not shown). The oils display different optical responses: the TIR critical angle depends on the fluid's Re(ϵ), while the slope of the transition depends on Im(ϵ).

transition. The real component of permittivity, ϵ_r, is plotted in Fig. 3.5 and determines θ_{crit}, while ϵ_i determines the slope of the transition. By subsequently scanning the line-tunable laser, initial values of complex permittivity vs. frequency were generated for both oils. Error was then approximated, an accepted value of ϵ_{oil} was derived, and polynomial functions were fit to represent the results.

In reflectivity measurements, R and θ error are independent. The experimental error in θ was $\pm 0.25°$. In reflectance measurements, the error was ± 1 mW for powers up to 50 mW and ± 2 percent of the signal for values above

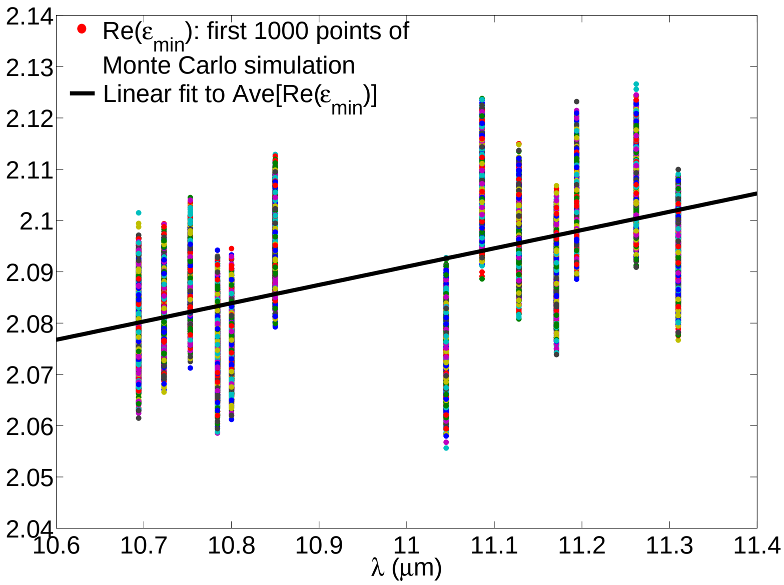

Figure 3.4: The first 10^3 results of the Monte Carlo-like error simulation for Re(ϵ_{min}) with a polynomial (linear) best fit to Ave[Re(ϵ_{min})]. The numerical simulation for each wavelength is independent.

50 mW; error bars in reflectivity are sparsely shown in Fig. 3.3 for clarity. Because the entire R vs. θ curve was fit to theory using a least-square minimization, one value of error did not suffice for all measurements, i.e., it is incorrect to offset each value of R by 0.5 percent and θ by 0.25°. Therefore, a Monte-Carlo-type numerical simulation properly estimated ϵ_{oil} and quantified error. A random array of error was generated that was (i) evenly distributed within the error range (e.g., θ between $-0.25°$ and $+0.25°$) and (ii) independent for each (R, θ) point. Random arrays were assigned to both R and θ, after which the numerical fitting returned a single value—the complex permittivity. The routine was run 10^4 times (to illustrate the simulation, the first 10^3 results

are shown in Fig. 3.4), resulting in a single average value of ϵ with error bars of $\pm 3\sigma$, the results of which are shown in Fig. 3.1 and Fig. 3.5. Wavelength-dependent $\epsilon_{mineral}$ and $\epsilon_{silicone}$ are represented by polynomial equations that best fit results, with $\lambda(\mu\text{m})$ in the laser's range given below:

$$\epsilon_{mineral} = 0.0357\lambda + 1.6989 + (-0.0018\lambda + 0.0324) * i \tag{3.3a}$$

$$\begin{aligned} \epsilon_{silicone} = &- 0.6984\lambda + 9.6559 \\ &+ (0.60994\lambda^3 - 19.6197\lambda^2 + 210.3616\lambda - 751.7636) * i. \end{aligned} \tag{3.3b}$$

Mineral oil is a generic mixture of liquid hydrocarbons (Fisher Scientific Cat. No. S55667), and silicone oil is poly[dimethylsiloxane] (Fisher Scientific Cat. No. S159-500).

3.5 Spectroscopic Methods

The 1.5-μm 3C-SiC film was grown on Si(100) as detailed in Ch. 2 and Ref. [69]. Infrared radiation was provided by a line-tunable CW $^{13}CO_2$ laser, with ranges of 10.666 μm–10.867 μm (R branch) and 11.025 μm–11.310 μm (P branch). Radiation was focused and then coupled through a 2.5-cm diameter ZnSe prism aligned in close proximity to SiC using the Otto configuration to allow for finite analyte gaps. The Otto method benefits from the principle that the prism is separated from the polaritonic film by a gap, allowing prism-free SiC film deposition and preventing the hard contact damage that is more common with the Kretschmann configuration. Moreover, the Otto gap provides an ideal chamber for small-volume analyte sensing.

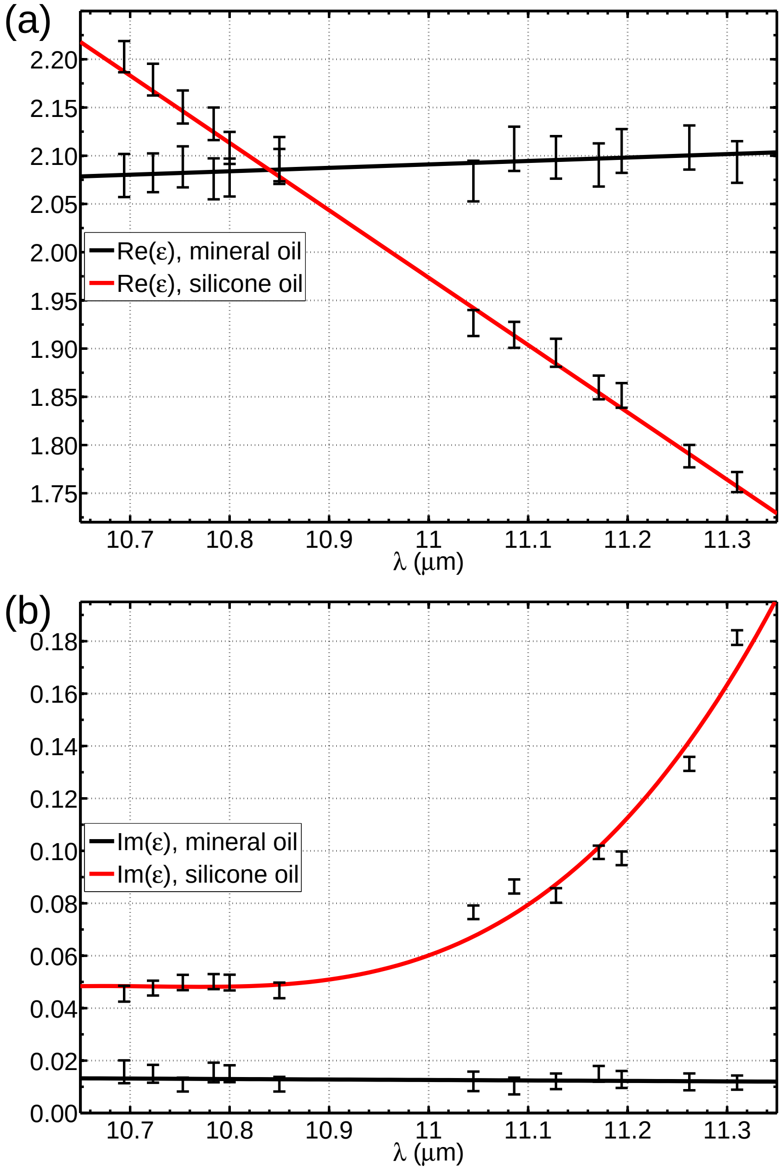

Figure 3.5: (a) Real and (b) imaginary components of mineral oil and silicone oil permittivity, resulting from Monte Carlo-like simulations. Polynomial fits to Ave[ϵ] are given by solid lines. Error bars denote the $\pm 3\sigma$ uncertainty.

The schematic exaggerates the 2-μm prism face bow (40-m radius of curvature). A HeNe laser (632.8 nm) was used for *in situ* gap determination to 50 nm accuracy via Fabry-Perot interferometry (Sec. 2.3.1). For analyte sensing experiments, the gaps were $d_1 = 3.0$ μm for analyte 1 (air), $d_2 = 2.1$ μm for analyte 2 (mineral oil), and $d_3 = 1.0$ μm for analyte 3 (silicone oil). The laser spot size in vacuum is 300 μm; considering radiation traveling through the prism ($n_{\mathrm{ZnSe}} = 2.4$) and oblique incidence, a typical *interaction* volume of 100 pL is calculated using, e.g, a 2 μm gap.[1] In comparison, nearly 20 nL are needed to detect biomolecular binding events with the Biacore 3000, a commercial instrument based on surface plasmon resonance (SPR) excited by visible radiation [86]. An interaction volume of order 100 nL was used for SPP-based mid-IR gas index sensing [6]. And 50 μL were required for mid-IR ZnSe-based ATR in the analysis of blood substrates in human plasma [41]. Numerical results in this work are averaged using a Gaussian angular profile (2° FWHM) of the incident beam that matches the experimental apparatus. Incident and reflected radiation intensities were measured using a laser power meter, and a rotation stage provided angular steps of 0.5°.

---

[1] To be certain, the *total* analyte volumes used in this and other sensing schemes are much larger than the interaction volumes, as the latter often account for volumes interacting with the evanescently decaying, sub-micron fields alone. It would be more appropriate to compare the total volumes required to sustain such sensors (e.g., fluid pumped through the sensing device). In such a case, micro-fluidic channels can be designed to minimize required fluid volumes.

3.6 Experimental Refractive Index Sensing

In the first sensing experiment, analyte 1 (air) was used with a gap of $d_1 = 3.0\ \mu$m, which provided an excellent baseline for fluid sensing because air is a simple dielectric, with $\epsilon_a = 1$. In the second sensing experiment, analyte 2 (mineral oil) was used with a gap of $d_2 = 2.1\ \mu$m, and in the third, analyte 3 (silicone oil) was used with a gap of $d_3 = 1.0\ \mu$m. Experimental results [70], which are given in Figs. 3.6 (a), 3.7 (a), and 3.8 (a), show that λ- and θ-dependent reflectivity is reproducible by theory, as given in Figs. 3.6 (b), 3.7 (b), and 3.8 (b). All spectra exhibit minima and thus SPP excitation, but by scanning λ, it's shown that the structure can achieve a globally minimal reflectivity and maximal SPP excitation—critical coupling—as reviewed in Ch. 2. Experiments would benefit from a fixed-gap apparatus and therefore a direct analyte sensing comparison. This important technical improvement was outside the scope of this work, but variable-gap prism coupling has been previously demonstrated [24]. Nevertheless, SPPs were observed for each fluid and gap, demonstrating resonant analyte sensing.

3.6.1 Results and Comparison to Modern Sensing Interrogation Schemes

Refractive index sensing is typically implemented using intensity (I), angular (θ), or wavelength (λ) interrogation [48]. The sensitivity S_x [48] and refractive index resolution δn_x [6] are given by

$$S_x = \frac{\mathrm{d}x}{\mathrm{d}n_a} \tag{3.4}$$

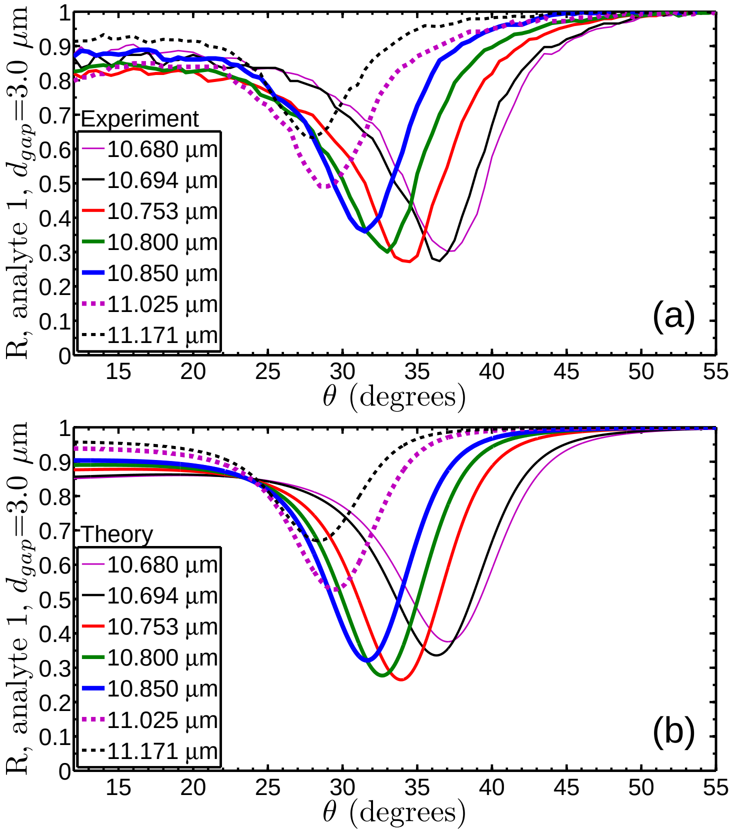

Figure 3.6: (a) Experimental plots of Otto-configuration R vs. θ are shown for multiple λ. (b) Corresponding theoretical plots, averaged over an angular spread to match experimental conditions. A 3.0-μm layer of analyte 1 (air) is contained between the prism and SiC.

and

$$\delta n_x = \frac{\delta x}{S_x}, \tag{3.5}$$

respectively, where x refers to to the interrogation method (I, θ, or λ), S_x is the derivative of the monitored parameter with respect to analyte index, and δx is the minimum parameter change that can be resolved by the sensing

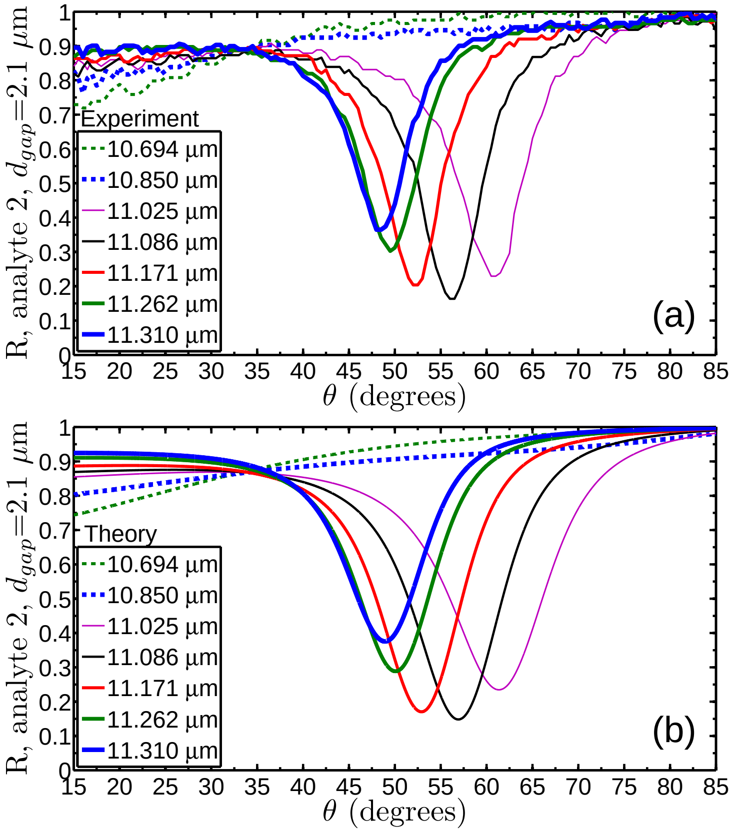

Figure 3.7: (a) Experimental plots of Otto-configuration R vs. θ are shown for multiple λ. (b) Corresponding theoretical plots, averaged over an angular spread to match experimental conditions. A 2.1-μm layer of analyte 2 (mineral oil) is contained between the prism and SiC.

system, which is usually limited by the rotation stage, detector sensitivity, etc.

To demonstrate the sensitivity and resolution of the sensing scheme presented here, the experimental results are built upon with the assistance of computation: an apparatus consisting of a fixed-gap SiC channel, a mid-IR source, and a variable-θ stage is proposed that can be tuned to achieve

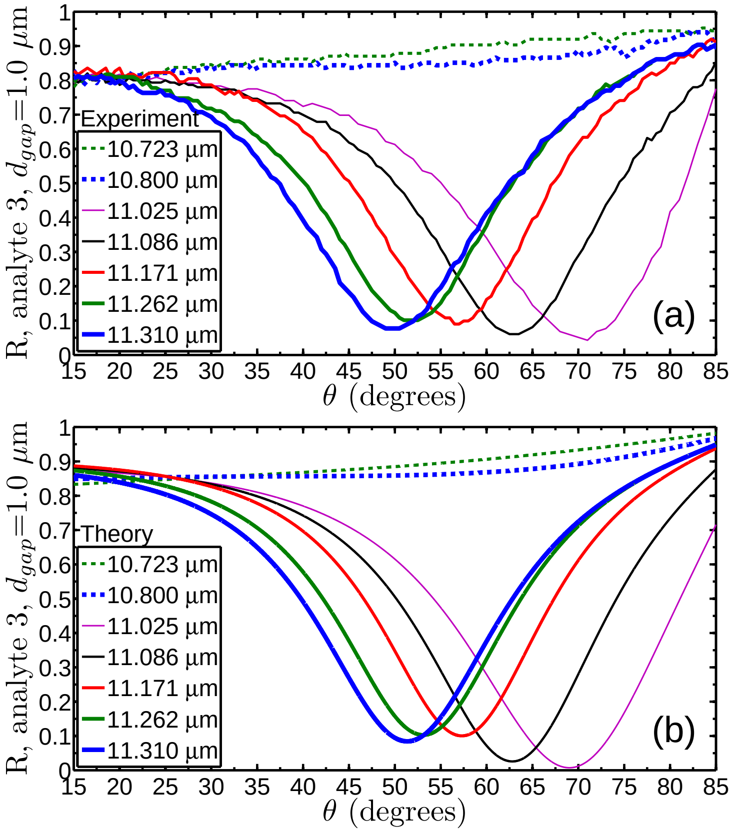

Figure 3.8: (a) Experimental plots of Otto-configuration R vs. θ are shown for multiple λ. (b) Corresponding theoretical plots, averaged over an angular spread to match experimental conditions. A 1.0-μm layer of analyte 3 (silicone oil) is contained between the prism and SiC.

minimal R and mid-IR index sensing through SPP excitation. This analysis, which uses experimentally verified values, will focus on intensity and angular interrogation, though wavelength interrogation, which yields resolutions comparable to angular measurements [48], has been demonstrated in the mid-IR using FTIR spectroscopy [6]. Using a gap of $d_{gap} = 2$ μm, which provides an interaction volume of 100 pL, and $\lambda = 11.086$ μm, reflectivities of 99 percent,

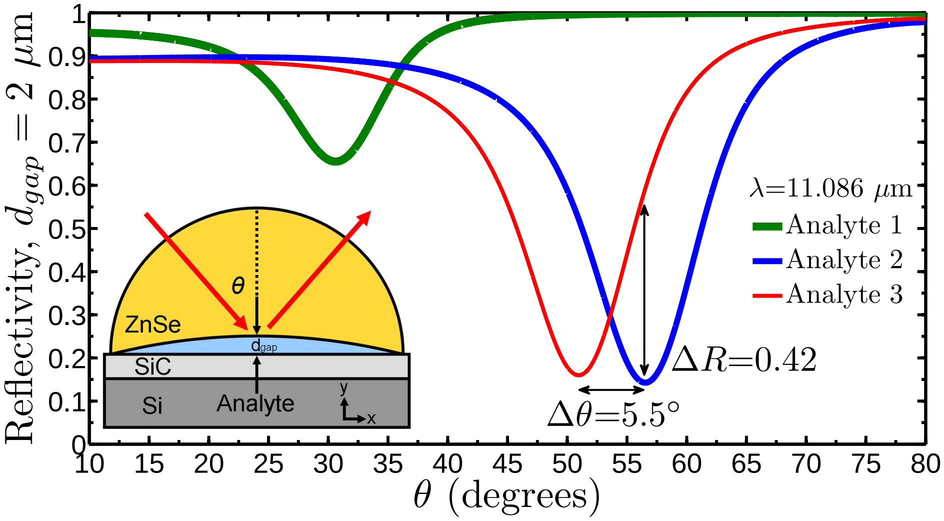

Figure 3.9: Reflectivity calculated at $\lambda = 11.086\ \mu$m with experimentally determined properties, with 1 μm of analytes 1 (air), 2 (mineral oil), and 3 (silicone oil) contained within the gap. Inset: schematic of SPP sensing at the SiC/analyte interface.

14 percent, and 56 percent are calculated for analytes 1, 2, and 3 at $\theta = 56.5°$, as shown in Fig. 3.9. Here, $\Delta n_{2,3} = n_2 - n_3 = 0.064$ RIU, or only 4.4 percent of n_2, but R increases by 42 percent—a fourfold increase in intensity. This increase in reflectivity corresponds to a sensitivity of $S_I = 656\%$ RIU^{-1} and a resolution of $\delta n_I = 1.5 \times 10^{-3}$ RIU ($\delta I = 1$ percent, limited by the optical system stability).

When analyzing the angular interrogation performance, the SPP minimum shifts by $\Delta\theta = 5.5°$ with $\Delta n_{2,3} = 0.064$ RIU, for a sensitivity of $S_\theta = 85.9°$ RIU^{-1} and a resolution of $\delta n_\theta = 5.8 \times 10^{-3}$ RIU ($\delta\theta = 0.5°$, SPP minimum shift resolution limited by prism divergence). This system's sensitivity is comparable to $S_\theta = 78.4^\circ$ RIU^{-1} found with a 2D nanohole array SPR sensor at near-IR wavelengths [105]. Near-IR and visible-range experiments offer superior source stabilization and detector sensitivity, leading to resolutions of order 10^{-5} RIU or better [48, 105] when probing analyte volumes as small as order 1 nL [105]. Depending on the target application, it is possible (as was shown in this work) to interrogate smaller volumes at the expense of higher resolution. The combination of analyte index specificity and pL-volume sensitivity makes mid-IR surface wave excitation a competitive platform for small-volume sensing applications.

3.7 Conclusions

In conclusion, small-volume index sensing with analyte specificity based on mid-IR surface phonon-polaritons at the SiC/analyte interface in the Otto configuration was presented. Highly specific sensing was demonstrated by a double-scan of λ and θ for three fluid analytes. SPP-based index sensing of pL-scale volumes exploits the local SPP resonance conditions and sensitivity to surrounding dielectric properties. Advanced sensing applications are possible, and by selecting other SPP-supporting materials such as AlN (11.2 μm–16.4 μm [73]) and GaP (24.8 μm–27.4 μm [112]), there is potential to tailor sensing applications to specific frequency bands as needed.

Chapter 4

Extraordinary Optical Transmission and Absorption in Subwavelength Silicon Carbide Hole Arrays

4.1 Introduction

The calculation of light transmitted through a single hole in a perfectly conducting metal screen was one of the first analytically solved problems in subwavelength (sub-λ) optics. Bethe found that transmission through a sub-λ hole is small, rapidly decaying with the hole diameter D as $(D/\lambda)^6$, where λ is the wavelength of light [10]. While this limitation seemed to suggest that nanoholes cannot serve as a nano-photonic devices, real metallic screens are not perfectly conducting, are not infinitely thin, and, in contrast to isolated holes, can be perforated with periodic arrays. More recently, extraordinary optical transmission (EOT) through sub-λ periodic hole arrays was discovered [28], generating increased interest in such structures.

The original EOT experiments were done using optically thick substrates: no light is transmitted through the films in the absence of holes. But contrary to Bethe's prediction, significant transmission was observed when the sub-λ hole array was present. Applications have already been discovered that make use of this novel result, including refractive index sensors [105], infrared absorption spectroscopy sensors [20], and multispectral biosensors [100].

Enhanced transmission results from the resonant excitation of surface plasmons, though some questioned the role of plasmons in subsequent publications [15, 63] because several complicated phenomena occur in EOT experiments. Diffractive and interference phenomena such as waveguide resonances [67, 15] were shown to contribute to or generate EOT. In this work, measurements were done in the mid-IR spectrum with perforated SiC films; an SEM image of the sample is shown in Fig. 4.1. It is shown that mid-IR SPPs are responsible for the observed EOT. As was presented in Ch. 2 and applied in Ch. 3, SPPs can be excited through prism coupling, but, as shown in this work, periodic structures, corrugations, or perforations can be used as well.

The skin depth represents the distance propagated in a material required to attenuate a wave's intensity to $1/e$, and is given by

$$\lambda_{\text{skin}} \equiv \frac{\lambda}{4\pi \text{Im}(n)}, \tag{4.1}$$

where λ is the free-space wavelength, the index of refraction $n = \sqrt{\epsilon}$, and ϵ is the material's dielectric permittivity. Because sub-micron-scale SiC films of thickness H are thin ($\lambda_{\text{skin}} > H$), transmission is larger for both perforated and unperforated films than optically thick samples. By using air-bridged (suspended) SiC membranes, the high-index substrate is eliminated, simplifying interpretation. Experiments are performed in the sub-λ regime ($D \ll \lambda$, and

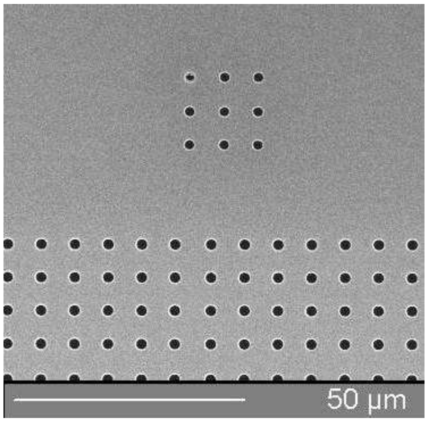

Figure 4.1: An SEM micrograph of the 7-μm period array of 2-μm diameter holes, with a reference cluster approximately 20 μm from the array edge. A nine-hole cluster was fabricated as a reference for spatial orientation.

pitch $L < \lambda$) where only SPPs and not diffractive effects can be responsible for EOT.

Extraordinary optical transmission and absorption of incident radiation was demonstrated through polarized FTIR micro-spectroscopy, which collects both transmitted and reflected radiation. Theoretical calculations and numerical simulations show that both phenomena are caused by the excitation of quasi-electrostatic SPPs. A perforated film can be described as a metamaterial with the effective permittivity $\epsilon_{\text{eff}} = \epsilon_r + i\epsilon_i$ strongly modified by the excitation of SPPs. With ϵ_{eff} known, transmission and reflection coefficients T and R can be calculated using Fresnel formulas for a dielectric slab. Regions of the enhanced transmission and absorption result from the lowering of $|\epsilon_r|$ and increase of ϵ_i, respectively. Quasi-static (QS) theory, which describes the SiC hole array optical response, is presented. The experimental methods and results are presented and compared to theory.

In this work, quasi-static theory and modeling were performed by Yaroslav Urzhumov, nanoscale sample fabrication and FTIR micro-spectroscopy were performed by the author and Dmitriy Korobkin, and SiC film growth was performed by Case Western Reserve University collaborator Christian Zorman.

4.2 Theory of Effective Optical Constants of SiC Hole Arrays

Theoretical techniques can characterize 3D metamaterials with sub-λ features [108]. The approach relies on the quasi-static approximation, which assumes that a patterned metamaterial (e.g., a SiC film perforated by a hole array) can be described by a quasi-static dielectric permittivity that is obtained by solving the electrostatic problem [9, 101, 94] of the material's response to an imposed electric field.

A series of electrostatic resonances are found using finite-element solver COMSOL, resulting in real eigenvalues s_n ($0 \leq s \leq 1$) and electric dipole strengths f_n of the n^{th} resonance. Each resonance contributes to the metamaterial's response to an external electric field according to its electric dipole strength, which in turn alters ϵ_{eff}. The effective permittivity is therefore given by the following expression [108]:

$$\epsilon_{\text{eff}}(\omega) = \epsilon_{\text{QS}}(\omega) = 1 - \frac{f_0}{s(\omega)} - \sum_{n>0} \frac{f_n}{s(\omega) - s_n}. \tag{4.2}$$

Four sample combinations were fabricated—using period and hole diameters of $[L, D] = [5\ \mu\text{m}, 1\ \mu\text{m}]$, $[5\ \mu\text{m}, 2\ \mu\text{m}]$, $[7\ \mu\text{m}, 1\ \mu\text{m}]$, and $[7\ \mu\text{m}, 2\ \mu\text{m}]$—but because the most dramatic results were obtained for the sample with thickness $H = 458$ nm, period $L = 7\ \mu$m, and hole diameter $D = 2\ \mu$m, all experiments and theoretical calculations were performed for these specific hole array dimensions.

The following expression for the dielectric permittivity of an unintentionally doped SiC film has been used in calculations:

$$\epsilon_{\mathrm{SiC}}(\omega) = \epsilon_\infty \frac{\omega^2 - \omega_{LO}^2 + i\gamma\omega}{\omega^2 - \omega_{TO}^2 + i\gamma\omega} + \frac{i\sigma}{\omega}, \tag{4.3}$$

where $\omega_{LO} = 972\ \text{cm}^{-1}$ ($\lambda_{LO} = 10.288\ \mu$m), $\omega_{TO} = 796\ \text{cm}^{-1}$ ($\lambda_{TO} = 12.563\ \mu$m), $\gamma = 5.25\ \text{cm}^{-1}$, finite conductivity $\sigma = 346.2\ \text{cm}^{-1}$, and $\epsilon_\infty = 4.71$ were found to give the best fit to the experimental transmission data for the unperforated membrane, as explained in Sec. 4.3.2. Equation 4.3 is the same as Eq. 2.15, but with an extra term accounting for low-frequency conductivity from unintentional dopants.

Many electrostatic resonances were discovered from the COMSOL simulation analysis; two examples are shown in Fig. 4.2. The lowest frequency modes are identified as modes modified by the presence of large-hole SPP(1,0) and SPP(1,1) resonances (given in Fig. 4.2 (a,b)), where the electrostatic potential and electric field in the film's mid-plane are shown. Additional resonances, along with eigenvalues and electric dipole strengths, are provided elsewhere [108].

With effective permittivity $\epsilon_{\mathrm{QS}}(\omega)$ known [108], the transmission (T)

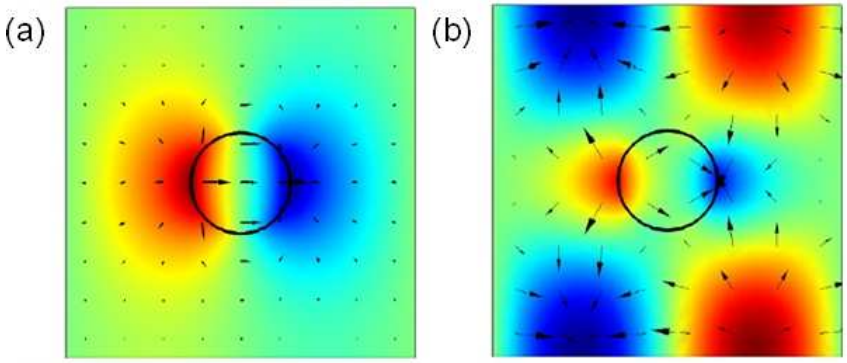

Figure 4.2: Electrostatic potential (color) and electric field profiles (arrows) in the mid-plane of a perforated SiC film ($H = 458$ nm, $L = 7$ μm, $D = 2$ μm). Delocalized resonances corresponding to (a) SPP(1,0) and (b) SPP(1,1). Courtesy of Y. A. Urzhumov.

and reflection (R) for the sub-λ array can be calculated using well-known formulas for a homogeneous slab. At normal incidence, these formulas are given as follows:

$$T = \left| \frac{(1 - r_1^2) e^{ik_0(n-1)H}}{1 - r_1^2 e^{2ik_0 nH}} \right|^2, \tag{4.4a}$$

$$R = \left| \frac{r_1 (1 - e^{2ik_0 nH})}{1 - r_1^2 e^{2ik_0 nH}} \right|^2, \tag{4.4b}$$

where $n = \sqrt{\epsilon_{\mathrm{QS}}}$, $k_0 = \omega/c$, and $r_1 = (1 - n)/(1 + n)$ [108].

Transmittance T and absorbance $A = 1 - R - T$ of the perforated film have been calculated, and the corresponding quantities for the non-perforated film (ϵ_{QS} replaced by ϵ_{SiC}) have been subtracted, resulting in differential quantities, which are shown in Fig. 4.8 (b). The absorption peak (red solid line) is caused by the peak of $\mathrm{Im}(\epsilon_{\mathrm{QS}})$ at $\lambda \approx 11.7$ μm in quasi-static approximation. At the same wavelength, excess transmission (blue solid line) equals zero, because $\mathrm{Re}(\epsilon_{\mathrm{QS}} - \epsilon_{\mathrm{SiC}}) \approx 0$. The transmission maximum occurs because the absolute value $|\mathrm{Re}(\epsilon_{\mathrm{QS}})|$ decreases at $\lambda \approx 11.8$ μm (since the value $\mathrm{Re}(\epsilon_{\mathrm{QS}}) < 0$ increases).

Surface plasmon polarization and dispersion responsible for transmission resonances have been explored through experiment [3, 8, 105] and theory [34, 88] for thick films, and their connection to the surface plasmons of smooth (unperforated) films has been noted. The connection is made by wavenumber matching: resonances of a perforated film with period L are related to surface plasmons of a smooth film with the in-plane wavenumbers

$$k_{(m,n)} = \left|\frac{2\pi}{L}(m\hat{x} + n\hat{y})\right| \equiv \frac{2\pi}{L}\sqrt{m^2 + n^2}, \tag{4.5}$$

where m and n are integers. Experimental spectra will be given in Sec. 4.3.3, showing EOT and extraordinary optical absorption (EOA) that results from the excitation of such optical-response-modifying SPP modes as those given in Fig. 4.2.

4.3 Spectroscopy of Perforated SiC Membranes

The experimental measurements of EOT and EOA in sub-λ arrays of holes milled in air-bridged SiC films is described. Experiments were performed in the mid-IR frequency range (7 μm $< \lambda <$ 16 μm) which includes the *reststrahlen* band of SiC. The FTIR micro-spectroscope used in this study collects all transmitted and reflected light, enabling the separate computation of scattered and absorbed fractions of the incident light, similar to an earlier study [8] of a perforated metal screen. An infrared polarizer enables the separation of peaks of EOT and EOA for both s and p polarizations. Also, by rotating the stage on which the perforated film is positioned (Fig. 4.3), the incidence plane of the beam with respect to the rows/columns of the array is changed for each polarization. This additional control enables, for the first time, an experimental demonstration of large anisotropy (up to a factor of two) with respect to different orientations of the incidence plane. Depending on the incidence plane orientation, absorption spectra are shown to exhibit single- or double-peaked transmission spectra.

4.3.1 Fabrication of SiC Membrane Hole Arrays

Two-dimensional hole arrays were fabricated in suspended (air-bridged) SiC membranes. The starting material for the membrane was a 458-nm thick single crystalline 3C-SiC film heteroepitaxially grown on a 0.5-mm-thick Si(100) wafer. The epitaxy of SiC was performed in a radio frequency (rf) induction-heated reactor using a two-step, carbonization-based atmospheric pressure CVD process detailed elsewhere [120]. Silane and propane were used as process gases, and hydrogen was used as the carrier gas. Epitaxial growth is performed at a susceptor temperature of about 1330°C. The SiC films grown using this process have a uniform orientation (100) across each wafer, as indicated by x-ray diffraction. Transmission electron microscopy and selective-area diffraction analysis indicates that the films are single crystalline.

The following steps were followed in the creation of SiC membranes.

Layers of 5 μm SiO_2 were deposited on both sides of the Si wafer in a high-temperature furnace (600°C). The surface opposite to SiC was coated with a 1-μm-layer of photoresist (Clariant AZ5209), after which 1 mm × 1 mm windows were exposed to ultraviolet (UV) by contact optical lithography (Karl Suss mask aligner). After resist exposure (60 s), development (45 s in Clariant AZ726 developer) and post-bake (20 m), the samples were placed in a BOE solution (2 hours), completely removing SiO_2 from the SiC side of the wafer and forming 1 mm × 1 mm openings in the SiO_2 mask on the opposite side. After removing photoresist in an acid solution, Si etching in a 35-percent KOH solution (at 80°C for 10 hours) was performed. The etch process of Si by KOH is anisotropic, which forms an angle of 35.3° from normal. Upon etching through the Si wafer (0.5 mm), 0.35 mm × 0.35 mm SiC membranes were exposed. High selectivity of the KOH etch with respect to SiC (260 000:1) ensured that SiC membranes were relatively unaffected.

A dual-beam focused ion beam (FIB)/scanning electron microscope (SEM) system (FEI Strata DB235) was used to create hole arrays in SiC membranes: FIB uses Ga^+ ions to mill through SiC while SEM uses electrons to observe results and produce micrographs. Several types of hole arrays were fabricated, but this work focuses on a square array sample with 2-μm hole diameters and a 7-μm lattice spacings, as shown in Fig. 4.1. Using an ion current of 300 pA, it took nearly four hours to fabricate a single 150 μm × 150 μm hole array with the aforementioned parameters.

4.3.2 FTIR Micro-Spectroscopy and SiC Film Characterization

A Perkin-Elmer Spectrum GX AutoImage FTIR microscope at the University of Texas at Dallas collected the transmission and reflection coefficients of samples in the 600 cm^{-1}–1500 cm^{-1} spectral range. The schematic of a typical IR microscope in Fig. 7.4. Spectral resolution of the FTIR was set to 1 cm^{-1}, and the spatial range was a $(100\ \mu\text{m})^2$ region in the focal plane, described in detail below. A video camera within the microscope displayed the sample position on a monitor. Samples were translated in horizontal (x, y) and vertical (z) directions, and were rotated about the z-axis. To define the spatial orientation of the sample, a nine-hole cluster was fabricated above the sample, as seen in Fig. 4.1. To calibrate reflection measurements, a high-quality aluminum mirror (CVI) was used. A wire-mesh polarizer (ISP Optics, 2400 grooves/mm) analyzed radiation in the FTIR spectrometer.

The IR beam is directed by Cassegrain optics, as schematically shown in Fig. 7.4, solely comprised of reflective surfaces. To determine the actual geometrical characteristics of the probing IR beam, its cross-section was scanned by small apertures in two planes—the focal plane and 557 μm above the focus. Pinholes with diameters of 20 μm and 40 μm were used for focal plane and above-focal plane scans, respectively. The beam distribution in the focal plane was nearly square with a 100-μm edge length. The beam characteristics are described by the two spherical coordinate angles θ and φ defined in Fig. 4.3. By analyzing the IR beam intensity distribution in both planes, it was determined that the incidence angle range is $\theta = 22^\circ \pm 4^\circ$. The azimuthal range of φ

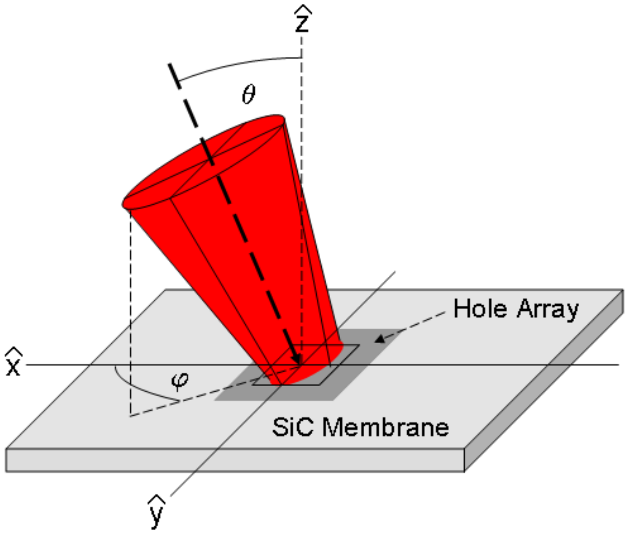

Figure 4.3: Schematic of the FTIR beam incident upon the hole array (not to scale). The beam characteristics are described by spherical coordinates: θ denotes the polar angle from the z-axis (normal incidence) and φ denotes the azimuthal angle in the x-y plane (SiC surface) from the x-axis, with respect to hole rows.

defining the orientation of the incidence planes with respect to rows/columns of holes is equal to $\approx \pm 10°$. Note that $\varphi = 0°$ corresponds to the incidence plane parallel to the rows of holes.

Unusual spectra from edge effects have been observed [25] in experiments with finite-sized arrays, where larger-than-array beams probe additional areas of non-perforated materials. The arrays in this work are effectively infinite because the probing radiation is contained to an area smaller than the array, ensuring that any observed result comes from the holes rather than from edge effects. The SiC hole arrays cover an area of $(150\ \mu\text{m})^2$; when rotated 45° about the z-axis, a square sample space must be larger than $(\sqrt{2} \times 100\ \mu\text{m})^2$

or about (142 μm)^2 in size to remain within the original (100 μm)^2 window of study. Samples of area (150 μm)^2 can therefore undergo 360° rotation for edge-effect-free illumination under any sample orientation, a condition necessary if studying angular anisotropy. In this work, the sample was studied under four orientations: $\varphi = 0°, 45°, 90°, 135°$. Clearly, the latter two orientations are redundant for square lattices, but the data are given in Fig. 4.6 and Fig. 4.7, showing the expected agreement between equivalent permutations.

Although the optical constants of bulk SiC are well documented [98], those of a thin epitaxially grown film must be determined experimentally. The discrepancy between thin-film SiC and bulk SiC occurs because the films grown at high temperature (i) experience high stress, and (ii) contamination may be difficult to prevent. For example, there is a high probability of unintentional nitrogen doping during growth that results in a high carrier concentration [120]. By examining transmission data, it is verified that the frequencies $\omega_{LO} = 972$ cm^{-1} ($\lambda_{LO} = 10.288$ μm) and $\omega_{TO} = 796$ cm^{-1} ($\lambda_{TO} = 12.563$ μm) reported for bulk SiC [76] are in excellent agreement with the data, but contamination alters the other parameters.

To account for the likely unintentional doping of SiC, an extra conductivity term appears in Eq. 4.3. A three-parametric least-square fitting between transmission spectra and transmittance given by Eq. 4.4a is then performed to determine the three unknown optical constants ϵ_∞, γ, and σ. Transmittances of both s and p polarizations ($T_{s,p}$) were included in the least-square minimization. The following constants gave the best fit: $\gamma = 5.25$ cm^{-1},

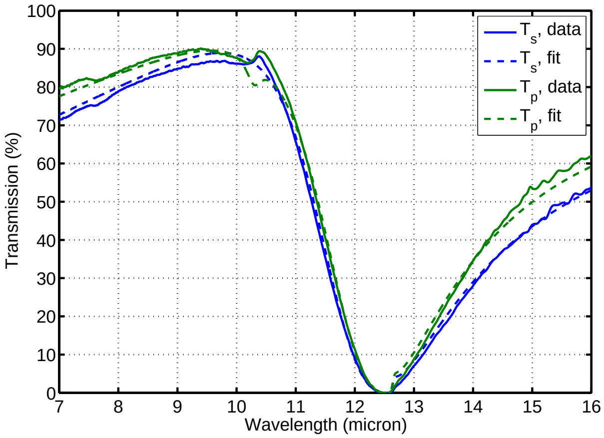

Figure 4.4: FTIR transmission spectra of the non-perforated 458-nm SiC film are given for s- and p-polarized light (solid lines). Theoretical spectra result from the best parametric fits, obtained as described in the text (dashed lines). Theory courtesy of Y. A. Urzhumov.

$\sigma = 346.2\ \mathrm{cm}^{-1}$, $\epsilon_\infty = 4.71$. Theoretical fits (dashed lines) and experimental measurements (solid lines) for both polarizations are plotted in Fig. 4.4 and show good agreement.

4.3.3 Experimental Results and Discussion

Using the dielectric permittivity $\epsilon_{\mathrm{SiC}}(\omega)$ with experimentally determined optical constants, theoretical simulations were compared with measured reflection $R(\lambda)$, transmission $T(\lambda)$, and absorption $A(\lambda) = 1 - R - T$ coefficients. The results obtained using an s-polarized incident beam and an incidence plane corresponding to $\varphi = 0°$ (parallel to rows of holes) are plotted in Fig. 4.5. An incidence angle $\theta = 22°$ was assumed for numerical simulations. Given the finite experimental spread in θ and φ, the agreement between theory and experiment is good. Both $T(\lambda)$ and $R(\lambda)$ exhibit characteristic kinks at frequencies corresponding to the excitation of SPPs, and the shapes of these kinks resemble Fano resonances [109, 29]. Fano-type resonances represent interference between radiation transmitted through the film (continuum state) with the radiation re-emitted by SPPs through the holes (discrete state). In previous experiments, identification of the continuous and discrete states was elusive [16]. In this experiment, there is no ambiguity in identifying the dominant continuum state because the film is transparent. Furthermore, the identification of surface polaritons as discrete states is clear because they are well-separated from Wood's anomalies. Spectra are taken for the 10.5 μm $< \lambda <$ 12.5 μm *reststrahlen* frequency band of SiC inside which $\epsilon_{\mathrm{SiC}} < 0$, so Wood's anomalies, which correspond to $\lambda \approx L = 7$ μm, are clearly outside of the spectral range of the experiments.

Experimental results shown in Fig. 4.5 (solid lines) demonstrate that transmission peaks correlate with the absorption peaks (as was previously noted [8]) because both are related to the excitation of SPPs. In full agreement with simulation results shown in Fig. 4.5 (dashed lines), the transmission peak is red shifted from the absorption peak. This is the first known experimental observation of this frequency shift.

While most hole array studies involve *optically thick* (several times thicker than the skin depth) films, these *optically thin* samples allow non-vanishing transmission without any perforations. Therefore, the role of the

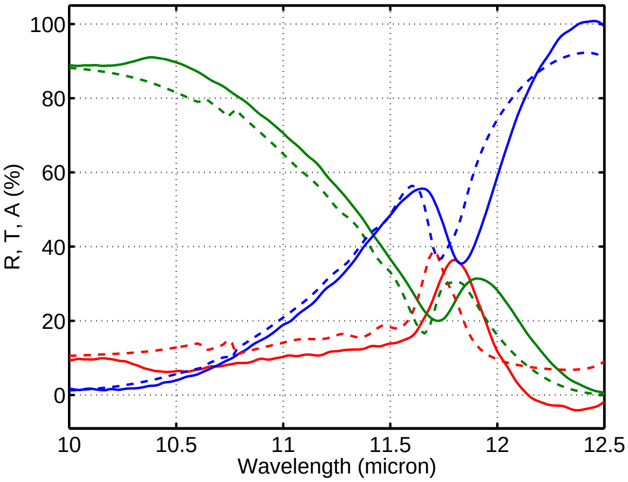

Figure 4.5: Reflection, transmission, and absorption spectra in blue, green, and red, for the 7-μm-period array of 2-μm-diameter holes under s-polarized light and with $\varphi = 0$ sample orientation. The experimental FTIR spectroscopy results (solid) are in agreement with simulation results (dashed). Reflection and transmission spectra display Fano-type resonances that result from continuum/surface mode interference. Theory courtesy of Y. A. Urzhumov.

hole array metamaterial can be directly quantified by collecting a hole array spectrum, a smooth SiC membrane spectrum, and then subtracting the second from the first to obtain a difference spectrum.

Spectra were collected under various conditions: both s- and p-polarized IR radiation were used, and the sample was rotated in the x-y plane in 45° increments from 0° to 135°. The results in Fig. 4.6 and Fig. 4.7 are displayed in a manner to show angular anisotropy at fixed polarizations. It is seen that spectra change considerably when the sample is rotated from a parallel to diagonal orientation. For p-polarized radiation with the incidence plane parallel to rows or columns ($\varphi = 0°$ or $\varphi = 90°$), both absorption (Fig. 4.6 (a)) and

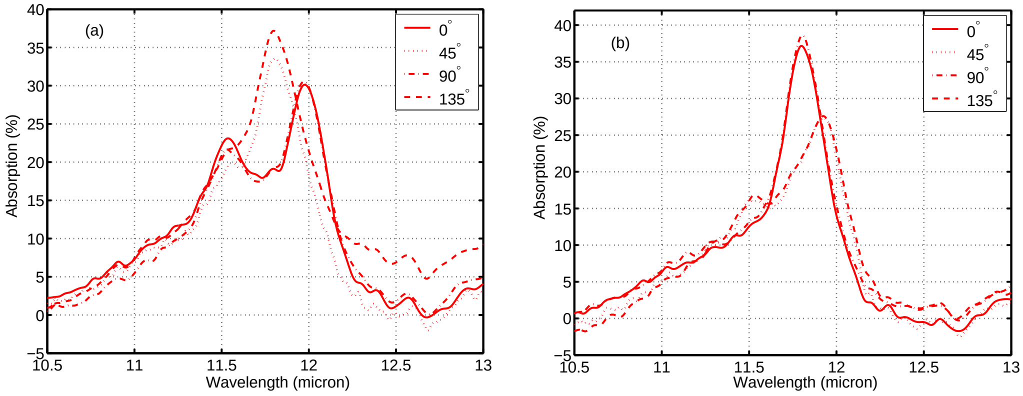

Figure 4.6: Absorption spectra for the 7-μm-period array of 2-μm-diameter holes under (a) p-polarized radiation and (b) s-polarized radiation with non-perforated film spectra subtracted. To study angular anisotropy, the sample was rotated in the x-y plane in increments of 45° from 0° to 135°.

transmission (Fig. 4.7 (a)) exhibit double-peaked spectra. Qualitatively, this is related to radiation that strongly couples to two SPPs with

$$k_{\pm}^{SPP} = \frac{2\pi}{L} \pm \frac{\omega}{c}\sin\theta \tag{4.6}$$

when incident at an angle θ. When the sample is rotated by 45°, the two peaks are too close to each other to be clearly distinguished. An opposite trend is observed in s polarization as shown in Fig. 4.6 (b) and Fig. 4.7 (b): for $\varphi = (0^\circ, 90^\circ)$ there is a single absorption/transmission peak which splits into two when the sample is rotated by 45°. As expected, the $A(\lambda)$ and $T(\lambda)$ spectra are invariant with respect to a 90° rotation as confirmed by all plots within Fig. 4.6 and Fig. 4.7—a reassuring sign that the array holes were precisely placed to form a symmetric, evenly spaced lattice. Through the aforementioned 90° sample symmetry, an absorption or transmission spectrum

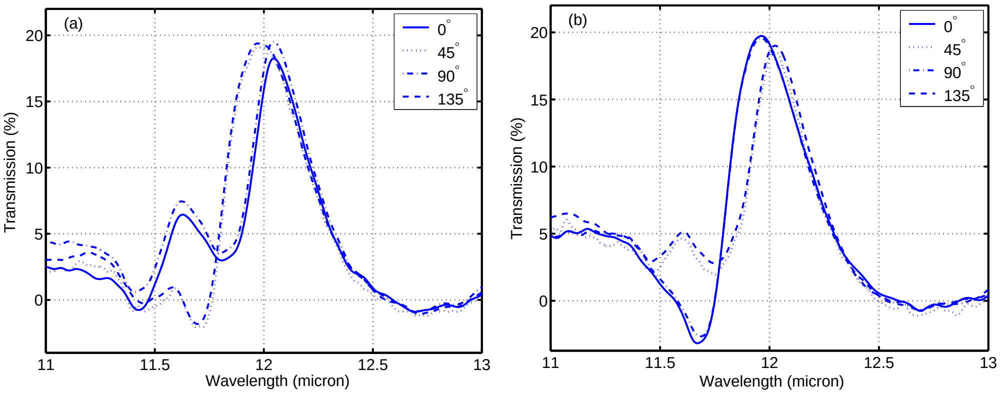

Figure 4.7: Transmission spectra for the 7-μm-period array of 2-μm-diameter holes under (a) p-polarized radiation and (b) s-polarized radiation with non-perforated film spectra subtracted. To study angular anisotropy, the sample was rotated in the x-y plane in increments of 45° from 0° to 135°.

will alternate between one and two peaks with rotation; this effect could be used in spectral filtering applications and for the identification and alignment of sample orientation.

Another interesting and potentially useful property of perforated hole arrays is their extraordinary birefringence with respect to light polarization. For a given sample orientation ($\varphi = 0°$ in Fig. 4.8 and $\varphi = 45°$ in Fig. 4.9), transmission and absorption spectra are plotted for s and p polarizations and compared to the corresponding simulations. For both sample orientations, significant transmission birefringence of order $|T_s - T_p| \approx 20$ percent can be obtained for the two polarizations, which is much larger than the birefringence from the unperforated film (about 5 percent) shown in Fig. 4.4. Enhanced s/p polarization birefringence can be explained using the qualitative band diagram

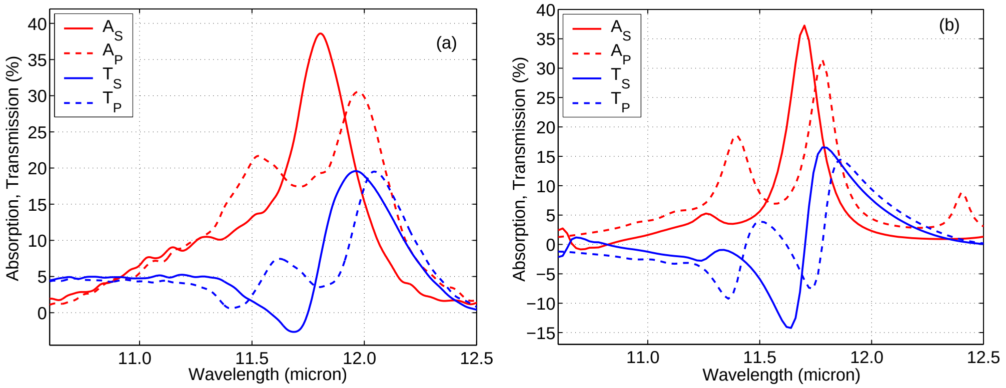

Figure 4.8: Absorption and transmission spectra from (a) experiments and (b) simulations for *s* and *p* polarization at 0° sample orientation with non-perforated film spectra subtracted. Absorption peak splitting, observed when changing from *s* to *p* polarization, is clearly seen in (a) and (b) with similar split peak-to-peak magnitude and frequency differences. Transmission spectra for both *s* and *p* polarization follow nearly identical paths in (a) and (b). Theory courtesy of Y. A. Urzhumov.

of SPPs [8]. Such enhanced birefringence will manifest itself in polarization conversion (e.g., from linear to elliptical) if the incident polarization is a superposition of *s* and *p* polarizations. Experimental indications of polarization rotation have already been found in earlier experiments [3, 105], although the connection to s/p polarization birefringence had not been made.

Experimental results shown in Fig. 4.8 (a) and Fig. 4.9 (a) show qualitative agreement when compared with their simulation counterparts shown in Fig. 4.8 (b) and Fig. 4.9 (b). For the $\varphi = 0°$ sample orientation, *s*-polarized light results in a strong single absorption/transmission peak, splitting to twin peaks with *p*-polarized light, observable in Fig. 4.8. The peak splitting in Fig. 4.8 (a) found experimentally is verified by simulations and shown in

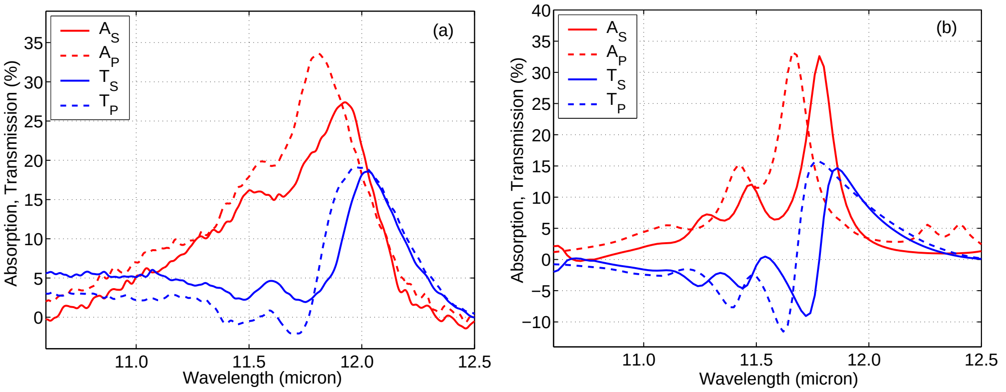

Figure 4.9: Absorption and transmission spectra from (a) experiments and (b) simulations for s and p polarization at 45° sample orientation with non-perforated film spectra subtracted. While the main s and p polarization absorption peak magnitudes differ in (a) but not (b), both sets display a similar frequency shift and maintain similar relative shapes. Transmission spectra also follow nearly identical paths in (a) and (b) for corresponding s and p polarizations. Theory courtesy of Y. A. Urzhumov.

Fig. 4.8 (b) with similar peak-to-peak magnitude and frequency differences. Peak splitting in p polarization and the lack thereof in s polarization has been noted earlier [8] for thick metallic films.

A significant s/p polarization birefringence also exists for the $\varphi = 45°$ sample orientation. Although the quantitative agreement between the experimental and theoretical results for the sample orientation of $\varphi = 45°$ shown in Fig. 4.9 (a) and (b), is less impressive than that for the $\varphi = 0°$ sample orientation (Fig. 4.8 (a) and (b)), the qualitative agreement is good. Both the primary and much smaller secondary absorption/transmission peaks in both polarizations are seen in experiments and simulations. The primary peaks in A_p and T_p are shifted to frequencies higher than those of A_s and T_s, an experimental result (Fig. 4.9 (a)) that is reproduced by simulation (Fig. 4.9 (b)). While the peak magnitude difference between A_p and A_s in Fig. 4.9 (a) is not seen in Fig. 4.9 (b), the frequency shift of 0.12 μm occurs in both experiments and simulations.

4.4 Conclusions

In conclusion, mid-IR extraordinary optical transmission from a square array of round holes with subwavelength-pitch milled in an optically thin SiC membrane was theoretically and experimentally explored. It was theoretically demonstrated and experimentally verified that EOT is accompanied by a slightly blue shifted absorption peak corresponding to extraordinary optical absorption. Both EOT and EOA were shown to be caused by the excitation of SPP resonances. While holes occupied only 6 percent of the total area, enhanced transmission (i.e., beyond smooth SiC) reached 20 percent, and enhanced absorption reached nearly 40 percent. Interestingly, total SiC volume was decreased by introducing a hole array, yet absorption *increased* as a result of microstructuring the material. An absorbance of this magnitude indicates that perforated SiC films can be used as highly efficient tunable thermal radiation source.

For the first time, the dependence of EOT and EOA on both incident wave polarization (s and p) and incidence plane orientation (with respect to the hole rows/columns) has been investigated. Large anisotropy with respect to the incidence plane orientation has been demonstrated and theoretically explained. Strong polarization dependance can be utilized in polarization converters while strong anisotropy can be used in sensing applications as a diagnostic of sample orientation.

Chapter 5

Tailoring the Polarization State of Spoof Surface Plasmons with Chiral Metal Surfaces

5.1 Introduction

Engineering dispersion, electric field confinement, and other surface plasmon properties through the design of nanoscale-structured plasmonic surfaces paves the way for advanced photonic devices. The mid-IR analogy to visible-range surface plasmon-polaritons is surface phonon-polaritons, which are supported in polar crystals such as SiC when $\epsilon < 0$, and were shown in Ch. 4 to induce extraordinary optical transmission and absorption in perforated SiC films. Conventional surface plasmons/phonons are known to be elliptically polarized in the plane normal to the metal surface and the plasmon's propagation direction. However, another type of engineered surface plasmon wave, which is referred to as the spoof surface plasmon (SSP) [81, 68], can be used in a wider range of systems—including perfect electric conductors (PECs)—and may not be limited to elliptical polarization. In this work it is shown that, along with other surface plasmon properties, SSP polarization can be tuned, thus expanding possibilities for plasmonic applications in polarization optics.

Metal surfaces can be made anisotropic by perforating them with rect-

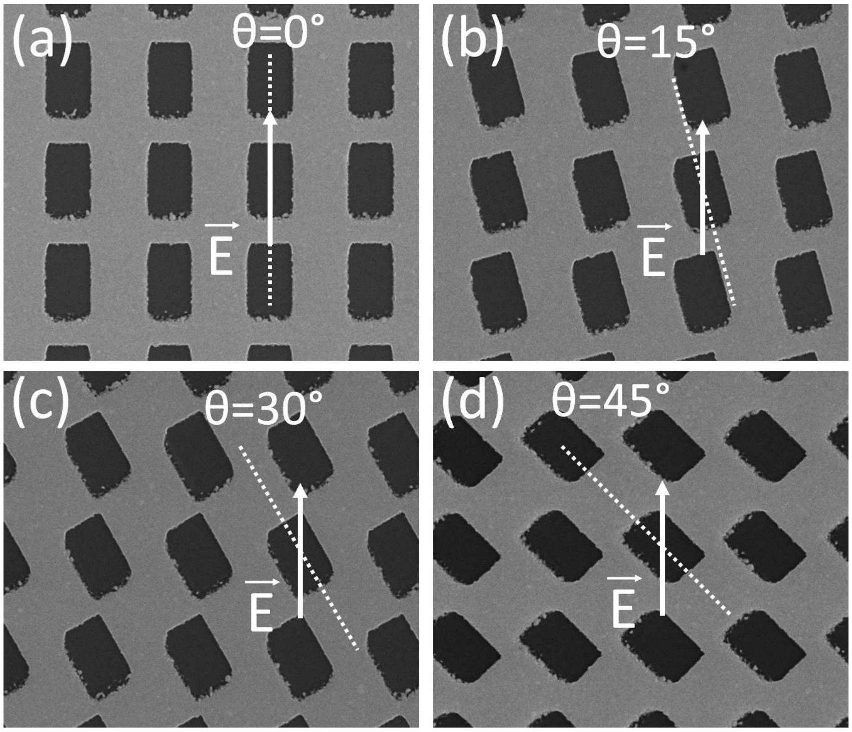

Figure 5.1: Four SEM images of the square-array chiral metamaterial structures. The samples shown correspond to rectangular perforations pinned to the square array with long axes rotated (a) 0°, (b) 15°, (c) 30°, and (d) 45° from **E**. Samples (c), (b), and (a) were then rotated 90° on the stage to achieve 60°, 75°, and 90° long axis orientations, respectively. The rectangles have width $a = 2.2\ \mu$m, height $b = 3.6\ \mu$m, and square lattice (x,y) periodicities $P_x = P_y = 4.7\ \mu$m.

angular or elliptical holes [31]. Such holes respond to incident electromagnetic fields as magnetic dipoles with differing polarizability along the two hole axes. Thus, SSPs propagating on the surface along different directions experience different effective refractive indices and interact with the surface as an anisotropic medium with anisotropy axes along those of the holes.

This work introduces the concept of an engineered SSP polarization state by making the surface chiral. The metal surface is perforated with rectangular holes that are rotated with respect to the array's square lattice by angle θ (see Fig. 5.1). In contrast to conventional optical-activity effects such as circular dichroism and polarization rotation (which arise from chirality of the constitutive molecules) this work's chirality is a collective, engineered response of achiral "molecules" (holes), and such a metamaterial can be referred to as an "extrinsically chiral" surface [82]. First, dispersion diagrams are calculated and SSP polarization is analyzed for different hole orientations, and second, SSP mode hybridization, which arises from rectangular perforation rotations and manifests in experiments as cross-polarized EOT, is explored. It is theoretically predicted and experimentally confirmed that the coupling of radiative air modes to such hybridized SSPs results in large polarization rotation.

In this work, nanoscale sample fabrication and FTIR spectroscopy were performed by the author, theoretical calculations and numerical modeling were performed by S. Hossein Mousavi and Alexander B. Khanikaev, and sample growth was performed by University Claude Bernard Lyon I collaborator Gabriel Ferro.

5.2 Description and Interpretation of the Structure

Fabrication of the metamaterial began with the deposition of SiC on Si(100), as detailed in Ch. 2. With Si back-etching, a 1-μm-thick SiC air-bridged membrane is exposed, which permits substrate-free transmission spectroscopy. In other chapters, SiC has been used as a surface phonon-polariton-supporting material; here, it is used as a mechanically stable thin dielectric slab, exhibiting $\epsilon > 0$ for $\lambda < 10.5$ μm. A 100-nm layer of Au was deposited on one side of the SiC film, and FIB milling perforated the metal. The membrane is $(800\ \mu\text{m})^2$ in size, so all four samples fit within the SiC window. In all cases, the square lattice periods are $P_x = P_y = 4.7$ μm. The four samples possess rotations as follows: $\theta = 0°$, $15°$, $30°$, and $45°$, where θ is the angle from the rectangle's long axis to the square lattice's vertical direction. The entire sample was then rotated 90° on the stage to achieve $\theta = 60°$, $75°$, and $90°$ long-axis orientations, when probing the 30°, 15°, 0° samples, respectively. The rectangles have widths $a = 2.2$ μm and heights $b = 3.6$ μm.

An extension of the semianalytical modal matching technique proposed by Martin-Moreno et al. [67] was used to describe light interaction with chiral metal surfaces. Fields outside the holes can be expressed in terms of the Rayleigh expansion because the surface indentations are periodic. Fields within the holes are calculated based on waveguide mode field expansions. Following the standard procedure of modal matching, continuity of the tangential components of the electric and magnetic fields at (i) the metal surface and (ii) at the hole entrance was imposed. Imposing such conditions permits the development of a system of linear equations that relate the amplitudes of incident fields ($\mathbf{E}_{in}$) and scattered fields ($\mathbf{E}_{sc}$) through a simplified S-matrix, $\mathbf{E}_{sc} = \hat{S}\mathbf{E}_{in}$.

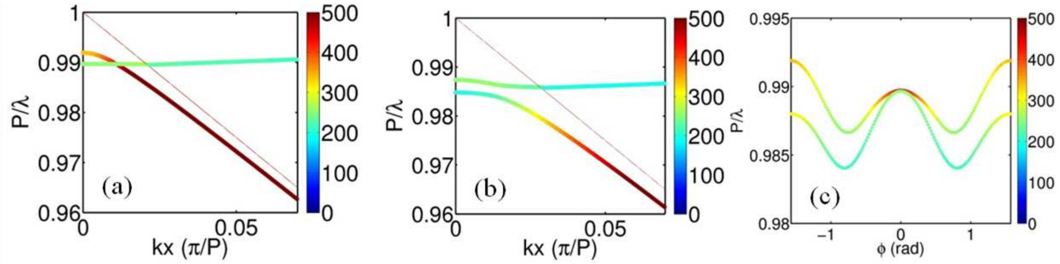

Figure 5.2: Band diagrams for the chiral structure's x $(-1{,}0)$ and y $(0{,}1)$ magnetic dipole resonances are given as lower and upper lines when the rectangle's long axis is rotated (a) $\theta = 0°$ and (b) $\theta = 40°$ from the square lattice. The thin red lines are $(-1{,}0)$ light lines. (c) The mode evolutions of the x (lower) and y (upper) modes are presented as a function of θ, beginning from the k_x degeneracy of (a). Courtesy of A. B. Khanikaev and S. H. Mousavi.

As a first step of sample interpretation, eigenmodes of the system for different hole orientations θ were found by solving the linear equation $\hat{S}^{-1}\mathbf{E}_{sc} = 0$ [57]. A reduction of lattice symmetry via hole rotation results in strong hybridization of the two SSPs in the vicinity of degeneracies. For non-rotated holes, the two SSP modes of interest correspond to the x and y magnetic dipolar moments associated with the $(-1{,}0)$ and $(0{,}1)$ diffraction orders near the Γ-point. The band diagrams for these two modes are plotted in Fig. 5.2 (a) and (b) as the lower and upper thick lines, respectively.

For the case of square holes (not shown), a twofold degeneracy takes place at the Γ-point (i.e., normal incidence), but for non-rotated ($\theta = 0$) rectangular holes ($b > a$), this *spectral* degeneracy, which is visible as a crossing in Fig. 5.2 (a), simply shifts to another point in the Brillouin zone. The removal of *geometric* degeneracy in the rectangle does not yet result in hybridization of x and y dipolar SSPs. However, once the holes are rotated ($\theta \neq 0$), the modes start to interact through the lattice and hybridize. Hybridization gives rise to a repulsion of the modes, which is visible in Fig. 5.2 (b) and (c), and new hybrid modes are formed. This repulsion results in the ability to use p-polarized light to excite the orthogonal s-polarized modes, and vice versa. Figure 5.2 (b) shows the band diagram for holes rotated 40° with respect to the lattice. Figure 5.2 (c) shows the dependence of SSP eigenfrequency on the rotation angle θ; the lower/upper lines correspond to the $(-1,0)/(0,1)$ modes.

The new modes represent waves which, in addition to the electric field component normal to the surface ($E_{\perp}$), have an electric field component elliptically polarized in the plane parallel to the surface ($E_{||}$). Such modes will now be referred to as “helical” SSPs. Calculations show that by changing the rotation angle, the degree of hybridization—and thus ellipticity—of such helical SSPs can be tuned.

5.3 Spectroscopy of Chiral Metamaterials

Coupling to helical SSPs is experimentally detected through polarization rotation. Incident light excites SSPs that propagate and then gradually decay into radiative scattered fields given by the propagating diffraction orders. However, during propagation on the surface, the SSP’s polarization evolves and the radiated wave fields will be, in general, polarized differently from the incident wave. Helical SSPs can be detected in conventional transmission/reflection experiments. Samples were analyzed using

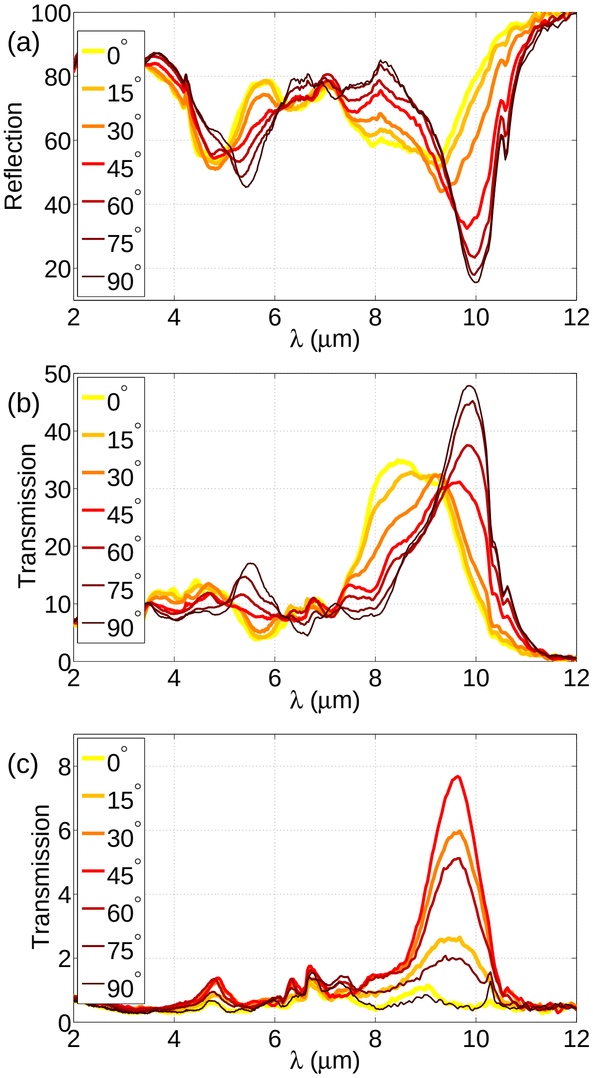

Figure 5.3: Reflection and transmission spectra from the polarization-rotating metamaterials. Angles listed correspond to rotation from the rectangle's long axis to the electric field vector. Radiation is *p*-polarized, and it is *p*-analyzed for (a) reflection and (b) transmission. Polarization rotation is directly measured in (c), as radiation is *s*-analyzed: the admixture of the cross-polarized component indicates excitation of the helical SSPs responsible for EOT.

FTIR micro-spectroscopy, where polarized reflection, polarized transmission, and polarized/cross-analyzed transmission were collected. The latter experiment directly shows the spectral regions where light undergoes polarization rotation, since no light is otherwise transmitted through the analyzer.

Theoretical spectra were confirmed through experimental reflectance and transmittance measurements of the seven sample configurations. Excitation of helical SSPs on the top side of the film alone was assured by fabricating the structure with an asymmetric cladding, i.e., air above and SiC below. The reflection spectra are plotted in Fig. 5.3 (a) and transmission spectra are plotted in Figs. 5.3 (b) and (c). The EOT for *p*-polarized radiation occurs at $\lambda \sim 8.5\ \mu$m. The spectra show that the transmitted wave has both *p*-polarized (Fig. 5.3 (b)) and cross-polarized (*s*-polarized) components (Fig. 5.3 (c)). The presence of the cross-polarized component confirms the excitation of helical SSPs in the structure, while the dependence of this component on the hole's orientation indicates tunability of the polarization state of these modes. Further theory and analysis will be presented in Ref. [57].

5.4 Conclusions

In summary, this work has shown that the polarization state of spoof surface plasmons can be altered, controlled, and ultimately made "chiral" through non-localized interactions with other perforations in the lattice. The metamaterial is a metal surface with rectangular hole perforations that are fixed to the array's square lattice but are rotated by angle θ. Polarization control is manifested by rotation or “helicity,” and it induces experimental cross-polarized extraordinary optical transmission. The degree of SSP helicity is determined by cross-polarized FTIR micro-spectroscopy of seven samples, each with a different angle θ that varies from 0° to 90° in increments of 15°. Such dispersion and polarization control in spoof surface plasmon-mediated structures may pave the way for advanced photonic devices.

Chapter 6

Engineering Better Infrared Antennas: the Metamaterial Approach

6.1 Introduction

The rf antenna [44] is one of the simplest and most ubiquitous electromagnetic devices, enabling modern communication technologies by transforming propagating radiation into localized energy, and vice versa. The principles of the metal rf antenna were extended into the optical range, making possible new types of antennas for infrared light localization and field enhancement [22], optical subwavelength microscopy [102], nanoscale photodetectors [103], and infrared emission sources [90]. When antennas or structures are organized into subwavelength-pitch 2D or 3D arrays, they are considered metamaterials [80, 96], and the bulk properties of scattering and absorption become important. Control over these metamaterial properties enables such applications as negative index materials [119] and impedance-matched absorbers [5]. Sophisticated visible range antenna design [102, 103] was facilitated by material availability, e.g., metals that possess finite-valued negative permittivity ($\epsilon < 0$) and therefore allow greater control over individual antenna response than their perfect electric conductor (PEC, $\epsilon \to -\infty$) rf counterparts.

The IR range is useful for many applications that include defense and security screening [56], nanoscale IR imaging [45], nanoantenna-array protein detection [1], and IR index sensing [70], but fewer studies have explored IR antennas because there is a relative lack of useful materials. Crozier et al. [22] demonstrated large electric field confinement and extinction $Q_{ext} \sim 4$ (absorption and scattering) with Au antennas in the mid-IR, but metals are still perfect conductors in this range and extinction is dominated by scattering because fields cannot penetrate the antenna [90]. Kirchhoff's law of thermal emission states that efficiently absorbing materials will efficiently emit radiation. Large scatterers will therefore make poor absorbers and emission sources.

In the IR, two alternative material types have been proposed as antennas/resonators: high-index dielectrics [111] and modest-valued negative permittivity ($\epsilon = n^2$) polar crystals [49, 91]. The latter provide the most exciting alternatives to metal because they possess both large positive and modest negative permittivity in the mid-IR. One such polar crystal is SiC, a material that exhibits both dielectric-type resonant modes [91] (for $\epsilon_{\mathrm{SiC}} > 0$) and "plasmon"-type surface phonon-polaritons [37, 46, 69] (for $\epsilon_{\mathrm{SiC}} < 0$) when micro- or nano-structured; ϵ_{SiC} is given in Fig. 6.1 (a). Schuller et al. [91] use SiC where $\epsilon_{\mathrm{SiC}} > 0$ and calculate $Q_{ext} \sim 8$ for a long 2D whisker, but the TM_0 mode's broad extinction results from large scattering, showing that both material selection and 3D structuring are critical to IR antenna design.

Here, attention is focused not on the bulk metamaterial but on the individual antenna: by engineering a fully subwavelength (sub-λ) 3D structure

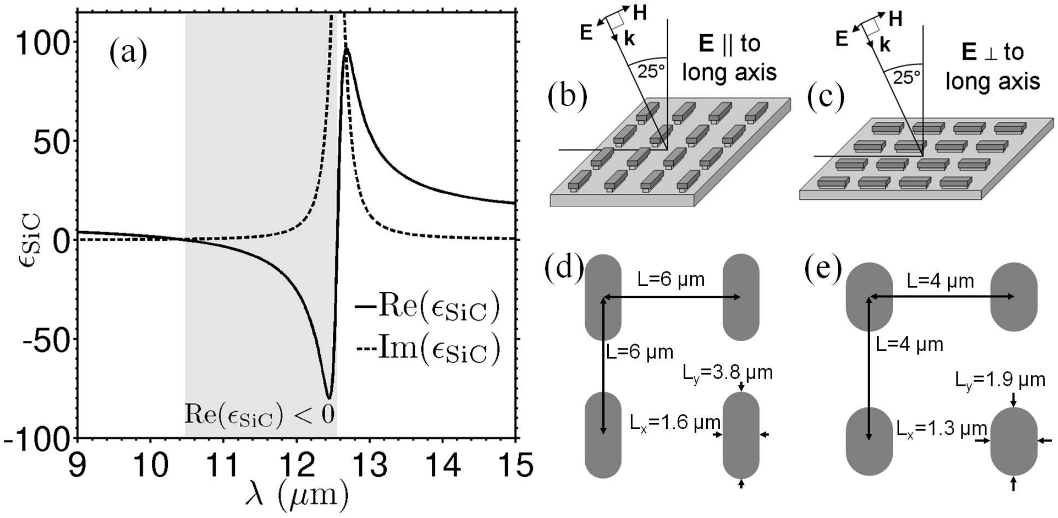

Figure 6.1: (a) SiC permittivity, with the region $\epsilon_{\mathrm{SiC}} < 0$ shaded. Spectroscopy schematics for **E**-field polarized (d) || and (e) ⊥ to the long axis. Antenna schematics for the (f) 6-μm-pitch and (g) 4-μm-pitch arrays.

from polar crystal, it is shown that (i) cutting long antennas to sub-λ size reduces scattering and impedance (Fig. 6.3), and that (ii) proper design of the antenna/pedestal/substrate cross-section can make weakly absorbing materials (e.g., SiC) strongly absorbing by generating magnetoelectric bianisotropy-induced tunable absorption in individual antennas (Fig. 6.4). Organizing isolated IR antennas [91] into metamaterial arrays then enables effective constitutive parameter extraction [64] (for bulk response modeling) and practical, large-scale IR applications [49, 5]. These properties and methods are experimentally verified with a novel, metal-free metamaterial array of densely packed SiC antennas (Fig. 6.2 (a)) with an asymmetric antenna/pedestal cross-section (Fig. 6.2 (b)). Resonance engineering in 3D sub-λ antennas allows for meta-

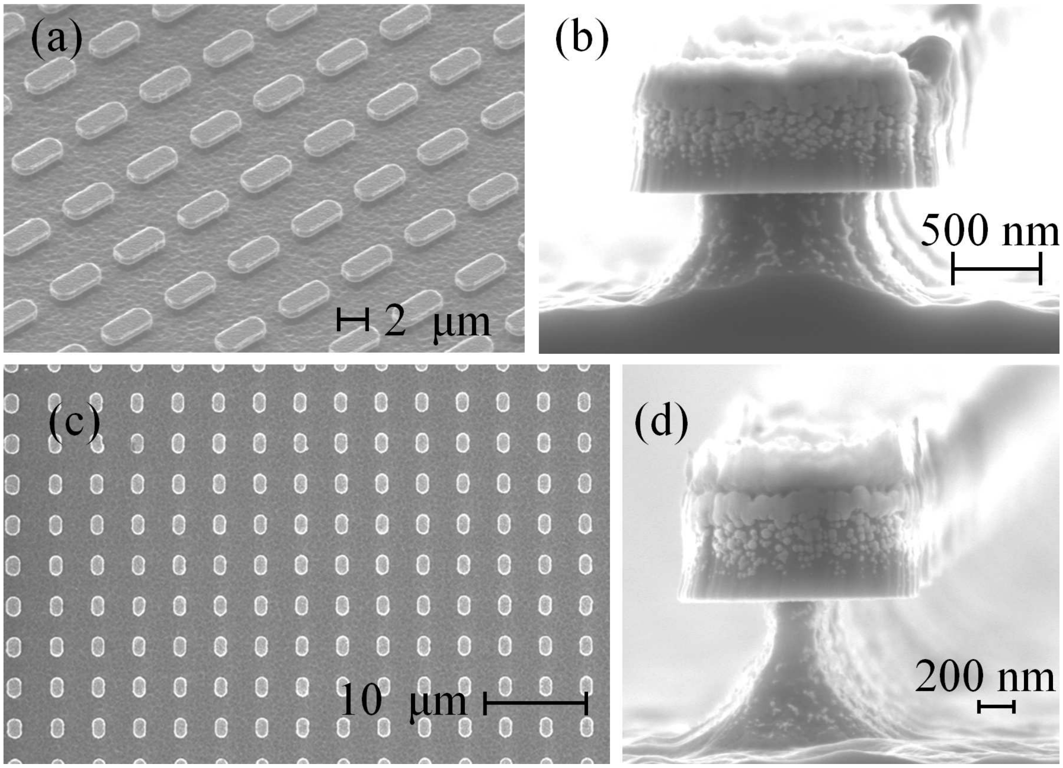

Figure 6.2: SEM images of (a) the 6-μm-pitch antenna array and (b) a single SiC antenna (viewing the short axis and the prominent Si undercut, with Ni etch mask included for contrast). (c) A micrograph view normal to the 4-μm-pitch antenna array is given, with the cross-sectional view of a single antenna shown in (d).

material performance optimization. Finally, direct emission measurements validate Kirchhoff's law of thermal emission, and display good agreement with absorption spectra.

In this work, nanoscale sample fabrication was performed at Sandia National Laboratories (NM) by Igal Brener et al., and theoretical calculations and numerical modeling were performed Chihhui Wu. The author performed Fourier transform IR micro-spectroscopy, the coordination of theory with experiment, and the interaction of all activities between the two institutions. Finally, direct measurements of IR emission were collected at Sandia National Laboratories.

6.2 Effective Medium Theory of Metamaterials

Long, dielectric ($\epsilon_{\mathrm{SiC}} > 0$) SiC particles support TM_0, TM_1, and TE_0 modes that induce electric and magnetic resonances, and the TM_1 and TE_0 modes can be used for thermal emission [90]. The long-antenna TM_0 mode doesn't efficiently emit because the induced electric resonance is strong, resulting in a large scattering cross-section. Furthermore, the mode is leaky, allowing free waves to easily couple to and from the mode.

To demonstrate that reducing antenna length to sub-λ scale indeed suppresses scattering, we retrieved effective parameters from 3D scattering matrix calculations of short and long SiC antenna/Si pedestal structures (no substrate), accounting for magnetoelectric coupling through the constitutive relations [64]:

$$\mathbf{D} = \bar{\bar{\epsilon}} \cdot \mathbf{E} + \bar{\bar{\xi}} \cdot \mathbf{H} \tag{6.1a}$$

$$\mathbf{B} = \bar{\bar{\mu}} \cdot \mathbf{H} + \bar{\bar{\zeta}} \cdot \mathbf{E}. \tag{6.1b}$$

Impedance is given as $z = \mu/(n + i\xi)$, and refractive index as $n = (\epsilon\mu - \xi^2)^{1/2}$, with ξ representing magnetoelectric bianisotropy.

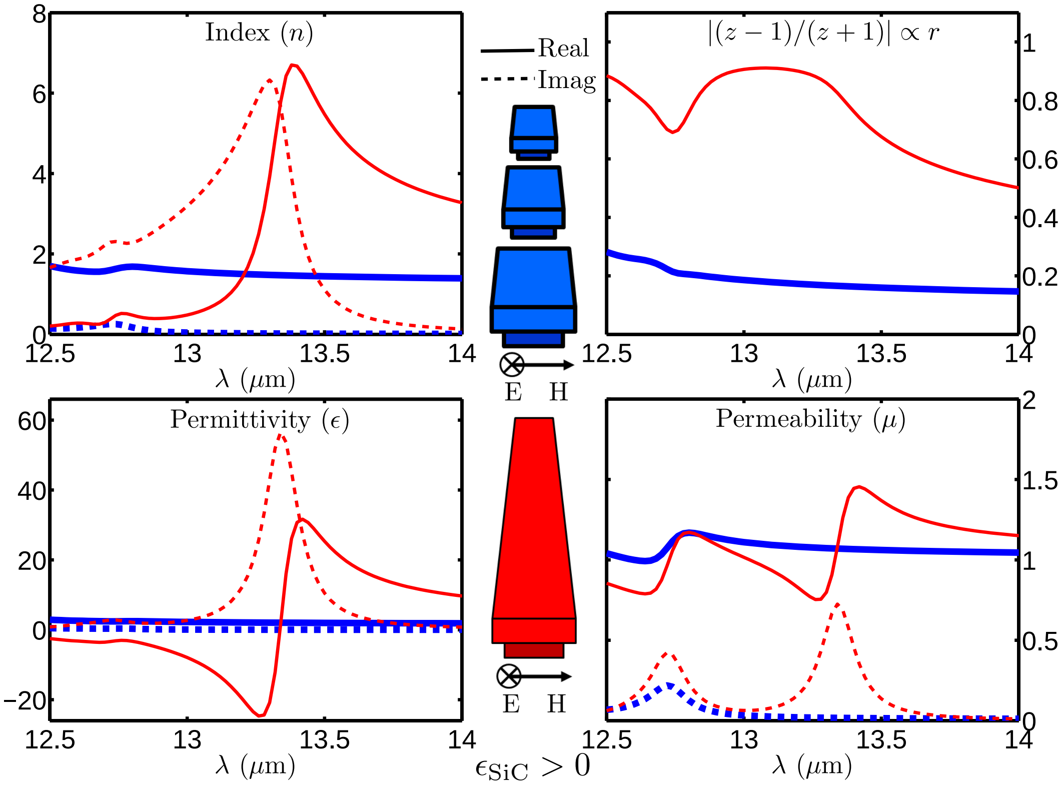

Figure 6.3: Short SiC antennas (thick blue lines) vs. infinitely-long antennas (thin red lines): effective parameters were retrieved from 3D scattering matrix calculations of the antenna/pedestal for $E_{||}$ polarization, with real (solid) and imaginary (dash) components. Cutting antennas to sub-λ size suppresses electric resonance. Effective impedance (z) is used to approximate reflectivity: through proper design, short antenna impedance can be reduced toward that of air.

6.2.1 Impedance Control through Reduced Electric Resonances

In long strips, there is a strong TM_0 electric resonance at 13.4 μm, resulting in large, lossy ϵ and impedance mismatch (Fig. 6.3). Scattering and z mismatch are visualized through $|z-1|/|z+1|$, which is proportional to the

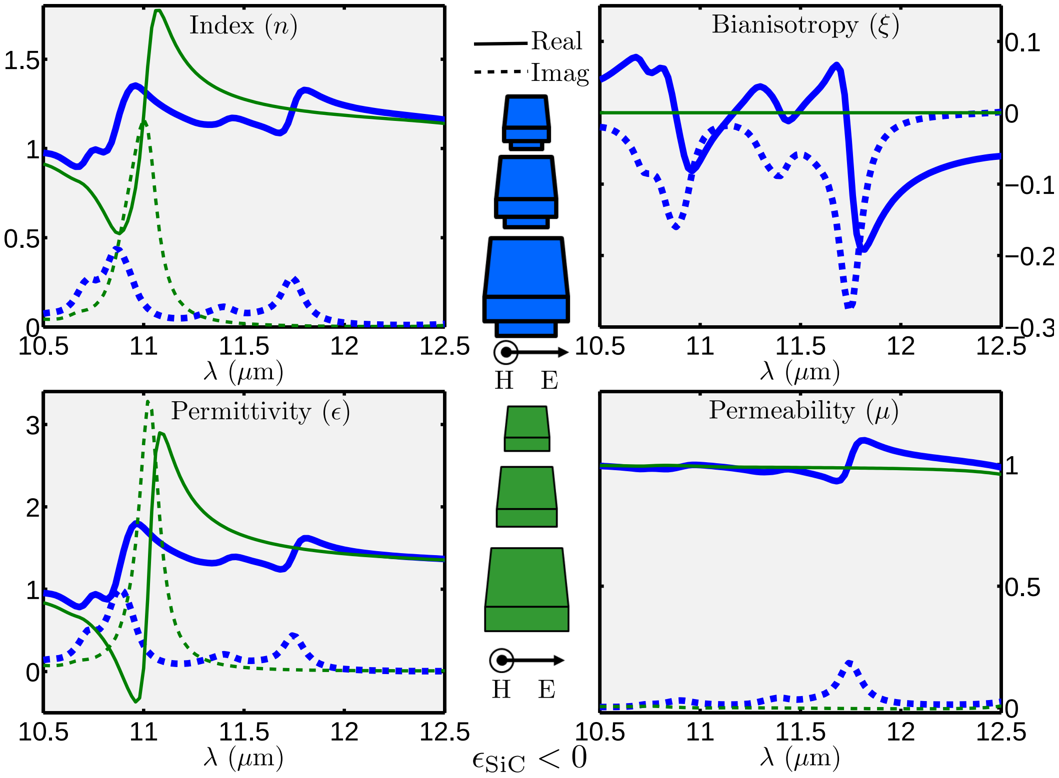

Figure 6.4: SiC antennas with (thick blue lines) and without (thin green lines) the Si pedestal: effective parameters were retrieved from 3D scattering matrix calculations using $E_\perp$ polarization, with real (solid) and imaginary (dash) components. The asymmetric antenna/pedestal structure generates strong bianisotropy (ξ) and absorption (Im(n), 8× increase) at 11.75 μm; this resonance can be tuned by adjusting geometry or pedestal index.

reflectivity amplitude r: as seen in Fig. 6.3, sub-λ antennas suppress the electric resonance, reducing impedance and reflectivity from the air side. Proper antenna design allows for the reduction of scattering/reflection to values below the substrate baseline; this was experimentally verified (Fig. 6.6 (b)) and will be discussed below.

6.2.2 Absorption Tunability through Metamaterial Bianisotropy

With impedance control possible, a method to modify absorption without dramatically changing z is considered, which is key because while many electric-resonant metamaterials exhibit large absorption ($\mathrm{Im}(n)$), mismatched z induces reflection. But when both electric and magnetic resonances exist, $\mathrm{Im}(n)$ remains large while z can be matched to air by tuning ϵ, μ, and ξ. The role of bianisotropy and its contribution to absorption (A) is explored by comparing antennas with and without pedestals. The extracted constitutive parameters of Fig. 6.4 show that while both structures exhibit a surface mode resonance at 10.90 μm, the antenna/pedestal structure alone generates strong bianisotropy ξ and absorption at 11.75 μm, which is manifested through an 8× increase in complex refractive index, $\mathrm{Im}(n)$. A change in pedestal index, antenna geometry, or antenna/pedestal interface area or cross-section can modify the relative magnetic/electric resonance intensity as needed. The large absorption peak in Fig. 6.6 (d) at $\lambda \sim 11.90$ μm provides experimental proof that the asymmetric antenna/pedestal structure's bianisotropic TE_0 mode can induce tunable absorption (the slight λ shift results from substrate presence).

6.3 Experimental Analysis of SiC Antenna Arrays

The antennas used to demonstrate mode engineering were fabricated from 625-nm-thick polycrystalline 3C-SiC [115], grown on a double-polished Si(100) wafer. The structure was patterned using contact photolithography. The inverse pattern was used with liftoff to create a metal hard mask of 100-

nm-thick Ni/Cr islands. The SiC was etched at room temperature with SF_6 using a Unaxis ICP rf plasma system. A 10-percent over-etch ensured complete removal of SiC and led to the 300-nm Si isotropic undercut etch (visible in Fig. 6.2 (b,d)). The Ni/Cr mask was removed with HCl. This work focuses on an array with square pitch $L_6 = 6$ μm, antenna widths of $L_x = 1.6$ μm, heights of $L_y = 3.8$ μm, and rounded corners (shown in Fig. 6.2 (a)). A second array, which will be discussed briefly, has a square pitch of $L_4 = 4$ μm, with $L_x = 1.3$ μm and $L_y = 1.9$ μm (shown in Fig. 6.2 (c)). Scale schematics are shown in Fig. 6.1 (d,e).

To characterize ϵ_{SiC}, FTIR micro-spectroscopy was performed on an air-bridged SiC membrane [108] cut from the same SiC used for antenna experiments. The polaritonic function [35], plotted in Fig. 6.1 (a), describes polar crystal permittivity for SiC, and was given in Eq. 2.15. This film possesses the following values for $\epsilon_{\text{SiC}}(\omega)$: the infinite-frequency permittivity $\epsilon_\infty = 6.7$, the longitudinal optical phonon frequency $\omega_{LO} = 955$ cm^{-1} ($\lambda_{LO} = 10.47$ μm), the transverse optical phonon frequency $\omega_{TO} = 796$ cm^{-1} ($\lambda_{TO} = 12.56$ μm), SiC damping $\gamma = 10$ cm^{-1}, and conductivity from unintentional doping $\sigma = 151$ cm^{-1}. These parameters were fit to thin-film transmission (T) and reflection (R), as discussed in Sec. 4.3.2. Antenna T and R spectra were collected with a Thermo Scientific Continuum microscope coupled to a Nicolet 6700 FTIR spectrometer using s-polarized radiation and a 2 cm^{-1} wavenumber resolution in the 1800 cm^{-1}–650 cm^{-1} (5.6 μm–15.4 μm) spectral range.

Experimental deviation from simulation occurs because the rapid etch creates slightly nonuniform antenna size, the rough-etched Si scatters light not accounted for by simulation, and convergent incident radiation (NA=0.58) contributes to wavevector averaging responsible for smooth extrema. Spectroscopy schematics for **E**-field parallel ($E_{||}$) and perpendicular ($E_{\perp}$) to the antenna's long axis are shown in Fig. 6.1 (b,c). Antennas were simulated with the finite element method package COMSOL. The 3D unit cell domain contains a single antenna, a Si pedestal, and a lossless Si substrate ($\epsilon_{\mathrm{Si}} = 11.6$) with periodic boundary conditions.

For $\lambda < 11.5$ μm, resonances exist in simulations but are less prominent in experimental data, appearing as a single peak in place of two closely spaced peaks, e.g., $E_{||}$ peaks at 10.85 μm and 10.95 μm. Such higher frequency modes correspond to plasmonic waves confined to the SiC sides and SiC/Si/air junctions, and while useful in optical device design, roughness can diminish the resonances, as the experiment demonstrates. Nevertheless, the most important modes are resolved and will be discussed below.

6.3.1 Results and Discussion: Extinction, Absorption and Reflection

A sample's extinction ratio is expressed in relation to the substrate and is given by the equation

$$EXT = 1 - \frac{T_{\mathrm{array}}}{T_{\mathrm{Si}}}. \tag{6.2}$$

The extinction efficiency, which accounts for the antenna's physical cross-section, is given by the equation

$$Q_{ext} = EXT\frac{a_{cell}}{a_{ant}}, \tag{6.3}$$

where the unit cell area $a_{cell} = 36\ \mu\text{m}^2$, and the antenna area $\text{a}_{ant} = 5.52\ \mu\text{m}^2$. These expressions, which are plotted in Fig. 6.5 for the 6-μm-pitch antenna array, describe antenna absorption and scattering [22], with the latter expressing the ability to scatter or absorb more light than impinges upon the antenna when $Q_{ext} > 1$. The near-circular Au antennas explored by Crozier et al. [22] with mid-IR radiation have similar a shape and peak Q_{ext} ($\sim$4) to this work's structure, but metal antennas are nearly PECs ($\epsilon \rightarrow -\infty$) in this range, so Q_{ext} will be dominated by scattering. Schuller et al. [91] use SiC with finite ϵ to avoid this problem and calculate Q_{ext} $\sim$8 for very long whiskers, but scattering often dominates in 2D particles, resulting in broad extinction peaks.

Sub-λ SiC antenna absorption ($A = 1 - R - T$) was calculated to determine if it instead dominates scattering in Q_{ext}. Reflection and absorption spectra are given in Fig. 6.6 (b,d) and show good agreement with 3D simulations Fig. 6.6 (a,c). Antennas exhibit strong A for both polarizations and for both signs of ϵ_{SiC}, reaching values of 50 percent (35-percent more than that from the substrate). Experimental reflection and absorption spectra from the 4 μm pitch array (Fig. 6.7) are included to show that a change in antenna geometry can tune resonant peak location: at $\lambda = 11.8\ \mu$m, $A \sim 50$ percent for this more circular antenna ($L_y = 1.9\ \mu$m for L_4 using $E_{||}$). Tunability is further demonstrated by changing polarization: a blueshift to 11.1 μm is achieved

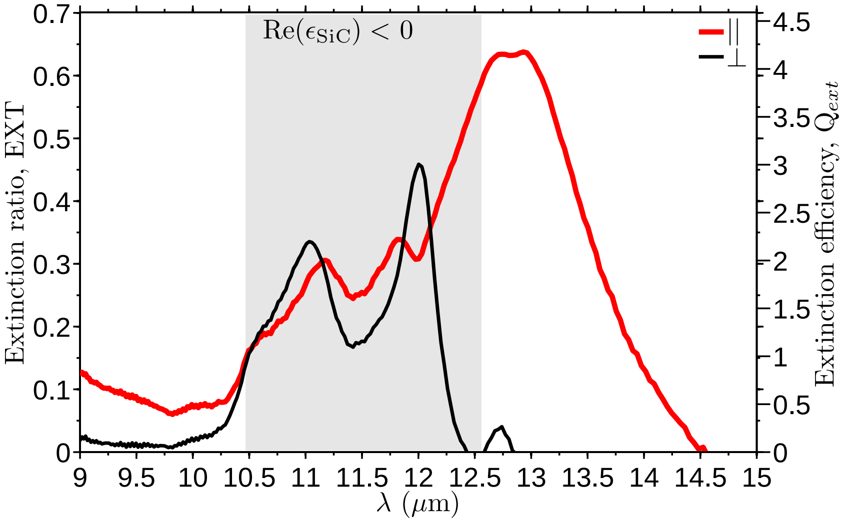

Figure 6.5: Experimental extinction ratios (EXT=$1 - T_{\mathrm{array}}/T_{\mathrm{Si}}$) and efficiencies ($Q_{ext} = \mathrm{EXT} * a_{cell}/a_{ant}$) for the 6-$\mu$m-pitch antenna array. The unit cell area $a_{cell} = 36\ \mu\mathrm{m}^2$ and the antenna area $a_{ant} = 5.52\ \mu\mathrm{m}^2$. Antennas scatter or absorb more light than impinges upon them when $Q_{ext} > 1$.

with very short antennas ($L_x = 1.3\ \mu$m for L_4 using $E_\perp$) while maintaining $A \sim 50$ percent.

6.3.2 Electromagnetic Mode Identification through 2D Modeling

Three-dimensional antennas can often be modeled in lower dimensions [74]: to understand A peaks and confirm that antenna standing waves (e.g., “plasmons”) are excited in the 6-μm-pitch array, a hybrid-mode 2D eigenvalue simulation was performed by modeling the antenna’s short axis cross-section (x, z), allowing for infinite length. The simulation resulted in propagation constants ($\beta = 2\pi/\lambda_r$) in the long axis (y) direction, where λ_r is the resonant

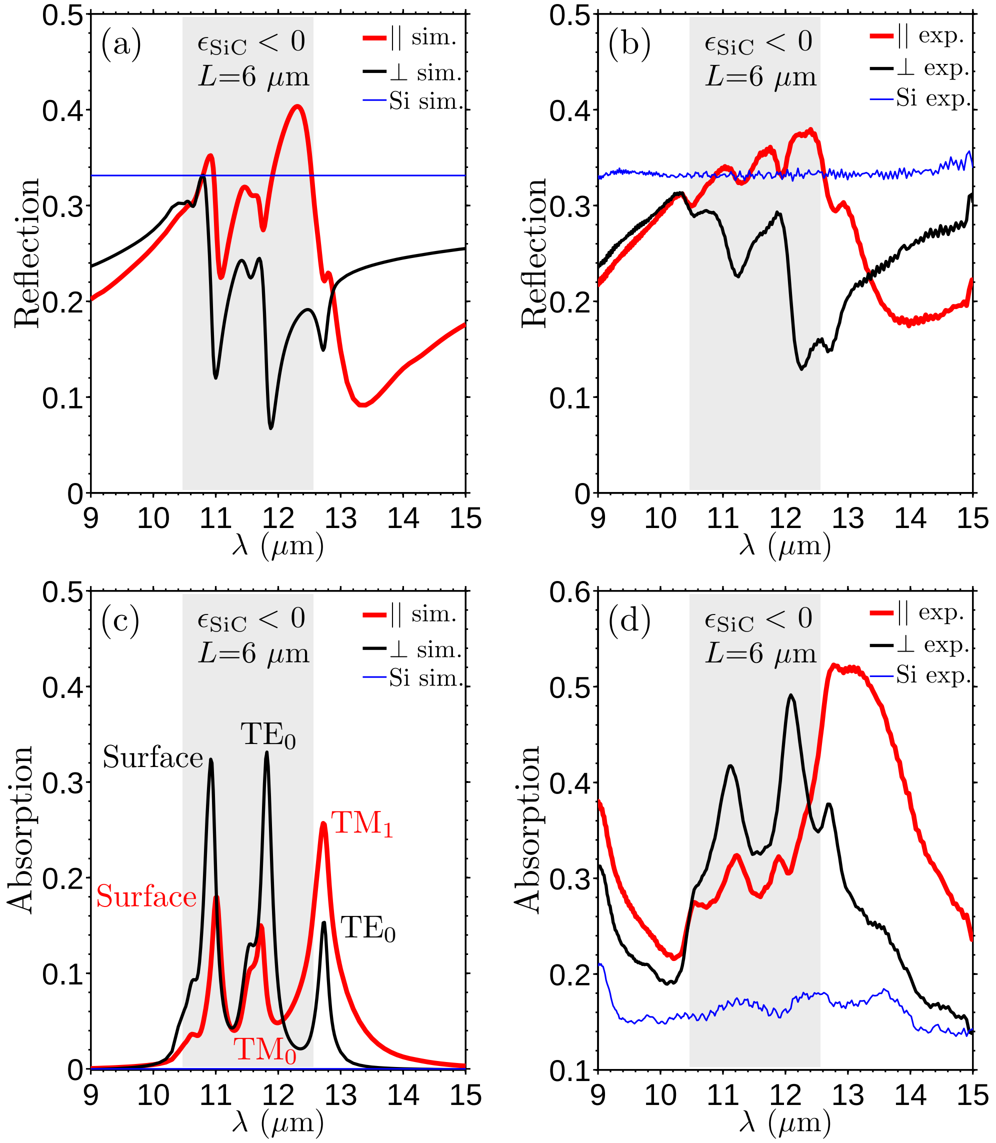

Figure 6.6: (a-b) Reflection (R) and (c-d) absorption ($A = 1 - R - T$) spectra from the 6-μm-pitch antenna array. (a,c) Simulations are compared to (b,d) experiments. Modes are identified when eigenvalues intersect with antenna resonant lengths (Fig. 6.8), and peaks are labeled in (c).

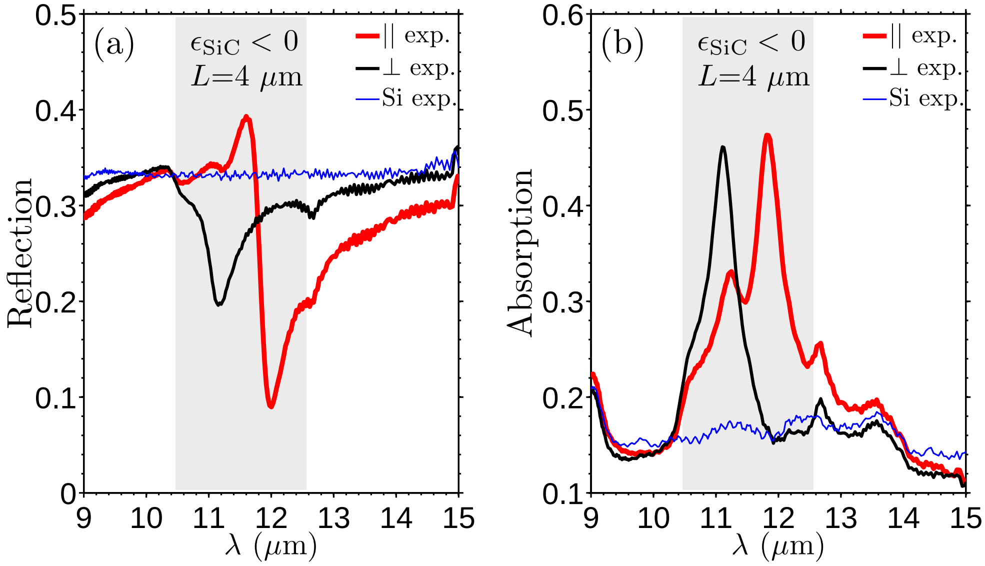

Figure 6.7: Experimental 4 μm pitch antenna (a) reflection and (b) absorption spectra. Tunability is demonstrated by observing the $E_{||}$ absorption peak in (b): blueshifted with respect to the 6 μm pitch array, $A \sim 50$ percent at $\lambda = 11.8$ μm for this more circular antenna ($L_y = 1.9$ μm).

wavelength, and the Fig. 6.8 dot size proportional to decay length. Resonances occur when matched to the real antenna length as

$$L_c = (2m+1)\frac{\lambda_r}{2} \tag{6.4}$$

where integer $m = (0, 1, 2, ...)$. The antenna's half circumference $L_c = 4.8$ μm accounts for width contributions.

The 3D simulation results are then confirmed: with a long and narrow antenna, resonances occur when the propagation constant

$$\beta = (2m+1)\frac{\pi}{L_c}. \tag{6.5}$$

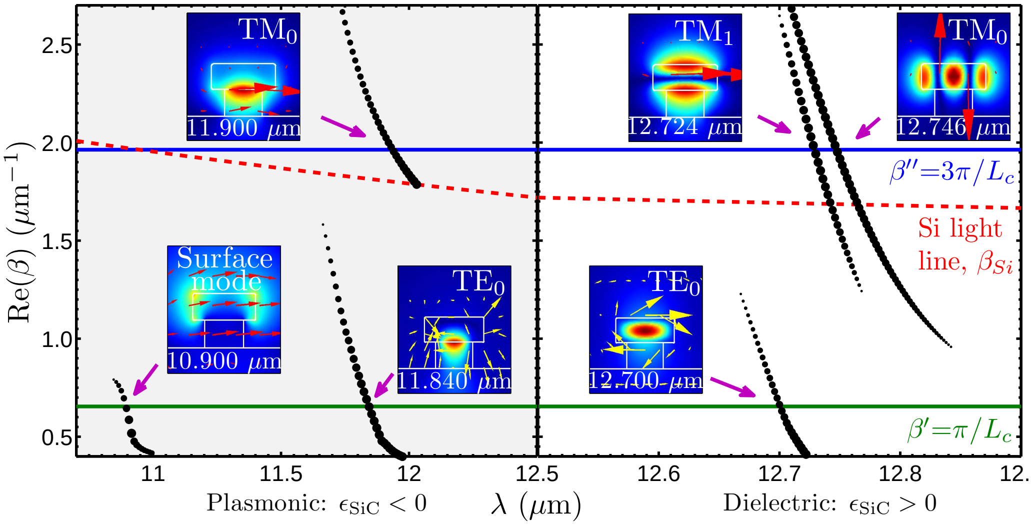

Figure 6.8: In-plane mode propagation constants (β) are plotted for the hybrid-mode eigenvalue simulation of 2D, infinitely long, periodic SiC antennas; dot size is proportional to decay length. Solid lines: resonant lengths matched to antenna length, where $\beta' = \pi/L_c$ and $\beta'' = 3\pi/L_c$ (L_c is circumference/2). Modes are identified when eigenvalues intersect with antenna resonant lengths, and peaks are labeled in Fig. 6.6 (c). The TM-dominant modes correspond to $E_{||}$ polarization, TE-dominant modes to $E_{\perp}$, and the surface mode to both polarizations. Note that because only evanescent ($\beta > \omega/c$) plasmonic TM$_0$ modes exist [74], the interaction is mediated by the substrate and therefore terminated by the Si light line. The TM and surface modes show in-plane electric field $|E_z|$ with color and **H** with red arrows. The TE shows $|H_z|$ with color and **E** with yellow arrows.

The two lowest resonances β' and β'' ($m = 0, 1$) are plotted in Fig. 6.8: intersections with eigenmodes indicate $\lambda_r/2$ and $3\lambda_r/2$ resonances, validating A peaks, as labeled in Fig. 6.6 (c). Modes are given as Fig. 6.8 insets: TM-dominant modes correspond to $E_{||}$ polarization, TE-dominant modes to $E_{\perp}$, and the surface mode to both polarizations (modes around the circumference are equivalent). The TM and surface modes show in-plane electric field $|E_z|$ with color and **H** with red arrows; TE modes show magnetic field $|H_z|$ with color and **E** with yellow arrows.

The antenna's length dependence that was seen in Fig. 6.3 is experimentally verifed. Using $E_{||}$ to excite an electric TM_0 mode gives an evanescent propagation constant ($\beta > \omega/c$) and a confined, canceling "+/-/+" field profile (12.746 μm in Fig. 6.8), resulting in scattering/reflection of only 18 percent (15 percent below substrate reflection in the 12.5 μm–15 μm range). Effective ϵ induced by TM_0 is now reduced and comparable to μ induced by the magnetic TE_0 (12.700 μm in Fig. 6.8) and TM_1 modes (12.724 μm in Fig. 6.8), allowing for impedance control ($z \rightarrow 1$).

With impedance control possible, the bianisotropy-induced tunable absorption ($\mathrm{Im}(n)$) that was observed in Fig. 6.4 is demonstrated. In the plasmonic region ($\epsilon_{\mathrm{SiC}} < 0$), simple side-surface and electrostatic TM_0 [90] "plasmon" modes exist (10.9 μm and 11.9 μm in Fig. 6.8). But introducing an asymmetric large-index Si pedestal below the antenna generates the needed magnetoelectric bianisotropic response: excited by $E_\perp$ radiation, the magnetic TE_0 resonance is induced by an electric response and generates R minima (Fig. 6.6 (a,b)) and A maxima (Fig. 6.6 (c,d)) at $\lambda \sim 11.75$ μm.

6.3.3 Direct Emission from SiC Antenna Arrays

As a test of Kirchhoff's law of emission and a demonstration of the antenna array's utility as an emission source, the 6-μm-pitch array was placed

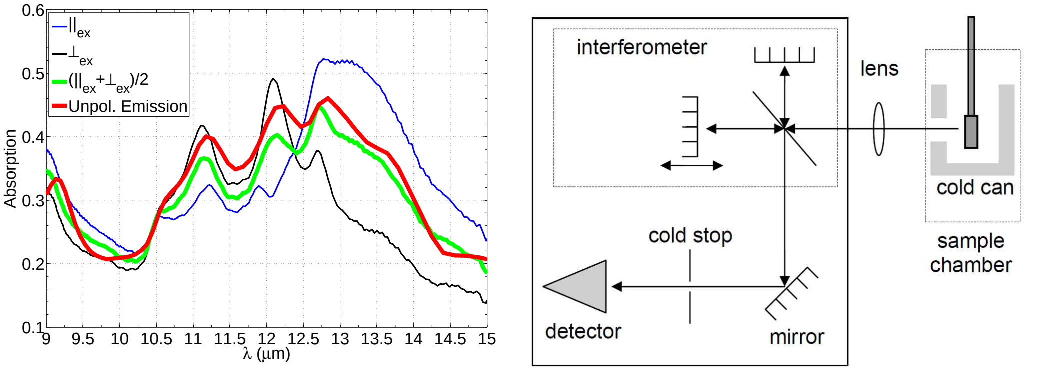

Figure 6.9: (Left) Experimental 6-μm-pitch antenna absorption and emission spectra. Unpolarized emission measurements were performed at Sandia National Laboratories (Albuquerque, NM). To properly compare emission (red) to absorption, a linear combination of two absorption polarizations (parallel and perpendicular) was calculated (green). (Right) Schematic for the novel emission setup.

inside an emission-source vacuum-pumped FTIR spectrometer (Fig. 6.9, right panel) located at Sandia National Laboratories in Albuquerque, NM. Unpolarized emission was detected from the sample, and is presented in the left panel of Fig. 6.9. To compare absorption to unpolarized emission, a linear combination of parallel and perpendicular polarization absorption was calculated. The agreement is excellent, proving that (i) materials that efficiently absorb will efficiently emit, and that (ii) sharp, resonant, and tunable emission is possible in SiC antenna arrays.

6.4 Conclusions

In conclusion, by engineering individual sub-λ infrared antenna modes, the metamaterial properties of impedance and absorption can be controlled and optimized: (i) cutting infinitely long antennas to sub-λ size reduces electric resonance and scattering which allows for impedance control, and (ii) large, tunable absorption is created by generating a magnetoelectric bianisotropic response in an asymmetric antenna/pedestal structure. Control was experimentally verified with a novel metal-free metamaterial array of 3D SiC infrared antennas. Emission measurements agree with absorption spectroscopy, validating Kirchhoff's law and demonstrating the metamaterial's potential as a source. The flexibility of antenna mode engineering through 3D structuring paves the way to more efficient tunable metamaterial absorbers and infrared emission sources.

Chapter 7

Fourier Transform Infrared Micro-Spectroscopy

7.1 Introduction

The Fourier transform infrared (FTIR) spectrometer is a powerful tool with which scientists and engineers from all backgrounds can analyze the interaction of incident radiation with matter over a wide frequency range. A typical FTIR system spans a near-IR to mid-IR wavelength range from approximately 2 μm–15 μm, but as this range depends on multiple internal components, the range is highly customizable. Many modes of operation are possible, which include standard transmission and reflection, extinction (a deficit of transmitted light that is absorbed or scattered), and attenuated total reflection (total internal reflection attenuated by evanescent coupling to a material). A discussion on FTIR spectroscopy in general and on ATR specifically can be found in Ref. [95] and Ref. [40], respectively.

Infrared spectroscopy is particularly useful to those who seek to identify unknown bulk liquids or gasses; the IR beam is focused to a sub-centimeter spot and interacts with fluid that has been placed in a transparent cuvette. In transmission mode, for example, IR absorption lines that correspond to molecular vibration and rotation modes will be observed as frequency-dependent transmission minima. A collection of absorption peaks, with specific frequencies and relative intensities, comprise the identifying “molecular fingerprint.” These methods can also determine the optical response of solids, from simple dielectric slabs to complicated 3D structured metamaterials.

The main limitation of the FTIR spectrometer is that of focal size. Submillimeter-scale samples require microscopic techniques. One FTIR micro-spectroscopic method discussed in this chapter utilizes a commercial IR microscope (Sec. 7.3), which was used for projects that include SiC hole array spectroscopy (Ch. 4) and the optical analysis of SiC antenna arrays (Ch. 6). While this micro-spectroscopic technique is powerful, limitations such as fixed incidence and poor polarization control exist, motivating the development of the external FTIR beamline (Ch. 8). In this chapter, however, FTIR spectroscopy and the IR microscope will be presented and analyzed.

7.2 Fourier Transform Infrared Spectroscopy

7.2.1 The Michelson Interferometer and the Fourier Transform

At the heart of the FTIR spectrometer is a broadband light source and a Michelson interferometer. As shown in Fig. 7.1, the “point source” (typically a small, electrically powered filament) emerges in one primary direction. The elliptical mirror M_1 focuses light through aperture J (known as the Jacquinot stop) to control divergence and partially define the system’s resolution (the other limiting factor is the mirror’s movement). Parabolic mirror M_2 colli-

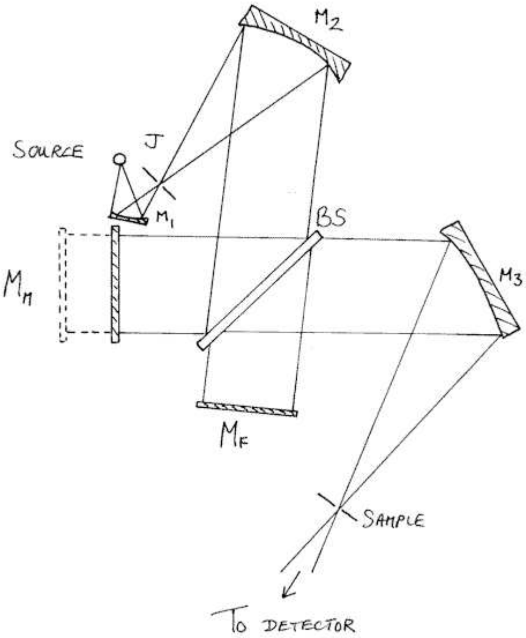

Figure 7.1: A schematic sketch of a Fourier transform infrared spectrometer. Elliptical mirror M_1 focuses broadband light through aperture J to define the system's resolution. Parabolic mirror M_2 collimates the light before passing it through the beamsplitter BS. Light is then reflected off planar fixed (M_F) and moving (M_M) mirrors. The resulting interfered light is focused by parabolic mirror M_3, interacts with the sample (in transmission or reflection mode), and is focused onto a detector element by an elliptical mirror (not shown). Figure courtesy of Ref. [66].

mates light before passing it through the beamsplitter BS. The beamsplitter directs approximately 50 percent of the incident light to each of the two subsequent mirrors. After the light reflects from the planar fixed (M_F) and moving (M_M) mirrors, it interferes at the BS: constructive or destructive interference occurs as a function of wavelength and moving mirror position. Typically, the resulting interfered light is focused by parabolic mirror M_3, interacts with the sample (in transmission or reflection mode), and is finally focused onto a detector element by an elliptical mirror (not shown). At this point, the detected signal, called the interferogram, simply relates the detector's signal voltage to absolute mirror position; the method that employs the Fourier transform to convert IFGs into an interpretable spectra [55] now follows.

Starting from the simple case of a monochromatic EM wave, the electric field strength E is given as

$$E = Ae^{i(\mathbf{k}\cdot\mathbf{r}-\omega t)}, \tag{7.1}$$

where the wave's amplitude is A, $\mathbf{k}$ is the wavevector, $\mathbf{r}$ is the coordinate vector, ω is the angular frequency, and t is time. The wavevector's magnitude

$$k = |\mathbf{k}| = \frac{2\pi}{\lambda} = 2\pi\nu, \tag{7.2}$$

where λ is the EM wave's free-space wavelength, and ν is the frequency. The scalar k is referred to as the wavenumber and is typically expressed in units of inverse centimeters (cm^{-1}). Two monochromatic plane waves propagating along x with phase difference δ and amplitude A_i take the form of $E_1 = A_1e^{i(k_x x-\omega t)}$ and $E_2 = A_2e^{i(k_x x-\omega t+\delta)}$. Once interfered, the resulting amplitude observed is

$$A^2 = A_1^2 + A_2^2 + 2A_1A_2\cos\delta. \tag{7.3}$$

If the two waves have equal intensity ($I \propto A^2$), where $I_1 = I_2 = I_0$, then the intensity of the interfered waves is

$$I = 2I_0(1+\cos\delta). \tag{7.4}$$

At normal incidence, rays propagate along the optical axis, and the phase difference is $\delta = kx$, where x is the optical path length difference. Therefore, the monochromatic output intensity is

$$G = 2I_0(1 + \cos(kx)). \tag{7.5}$$

Of course, the spectrometer's source is broadband and continuous, so the spectrum in the interferometer is $E(k)$. Therefore, the total signal from the entire spectrum is

$$G(x) = 2\int_0^\infty E(k)[1 + \cos(kx)]dk. \tag{7.6}$$

The expression $G(x)$ is the interference record of the spectral band as a function of path length difference x. Subtracting the constant term

$$\frac{1}{2}G(0) = 2\int_0^\infty E(k)dk \tag{7.7}$$

from the interference record $G(x)$ yields the interferogram

$$I(x) = G(x) - \frac{1}{2}G(0) = 2\int_0^\infty E(k)\cos(kx)dk. \tag{7.8}$$

The interferogram (IFG) now has a baseline intensity of zero, as evident in the example provided by Fig. 7.2 (a).

For simplicity of computation, the definition $E(-k) = E(k)$ is used, and the IFG becomes

$$I(x) = \int_{-\infty}^\infty E(k)\cos(kx)dk = \int_{-\infty}^\infty E(k)e^{ikx}dk = F\{E(k)\}, \tag{7.9}$$

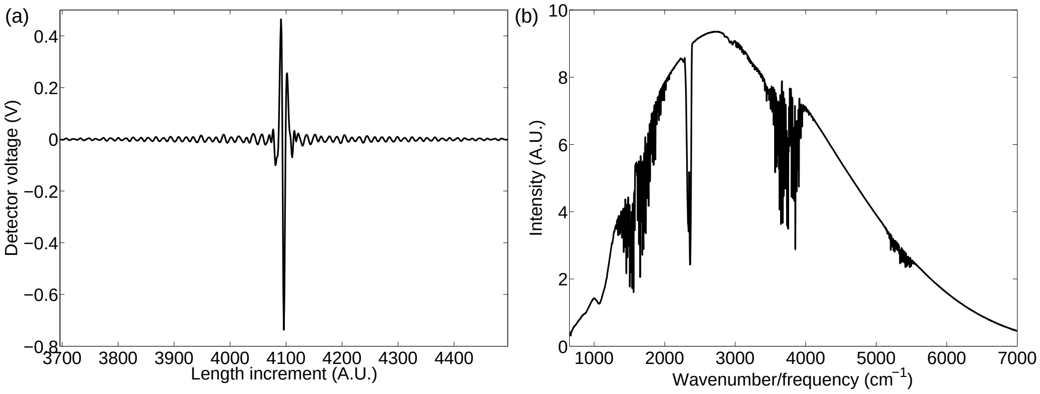

Figure 7.2: (a) A raw interferogram (IFG) of open transmission from the Continuum microscope/Nicolet 6700 FTIR spectrometer; the x axis (arbitrary units) belongs in the mirror's length domain. Software relates the moving mirror position to relative mirror displacement (in centimeters) and performs the Fourier transform (FT) to convert the IFG into frequency space. (b) A result of the FT, open transmission intensity (arbitrary units) is given as a function of wavenumber (cm^{-1}), which is proportional to frequency.

where F is the Fourier transform. Therefore, $I(x)$ and $E(k)$ form the Fourier pair

$$I(x) = \int_{-\infty}^{\infty} E(k) e^{ikx} dk = F\{E(k)\}, \tag{7.10a}$$

$$E(k) = \int_{-\infty}^{\infty} I(x) e^{-ikx} dx = F^{-1}\{I(x)\}. \tag{7.10b}$$

The moving mirror places the IFG in the length domain (x), so the desired frequency spectrum $E(k)$ is calculated by the spectrometer software via the inverse Fourier transform. As an example, an open-transmission IFG was collected (Fig. 7.2 (a)) and converted via the inverse Fourier transform into the recognizable frequency spectrum (Fig. 7.2 (b)). With an understanding of how the instrument operates, the system components that determine the spectral range are now considered.

7.2.2 Operational Range

The reflecting optics within the FTIR make the instrument useful to spectral ranges from the UV ($\lambda \sim 350$ nm) to the far IR ($\lambda \sim 500$ μm) because their focal properties are largely independent of frequency. But this flexibility is restricted to the mirrors alone: the source, beamsplitter, and detector all play critical roles in defining the device's spectral range. The Shvets Laboratory operates a Thermo Scientific Nicolet 6700 FTIR spectrometer. The device has multiple operation ranges, which are defined by the three components above, and are given in Fig. 7.3. Because the group is currently interested in studying near-IR and mid-IR photonic materials with high sensitivity, an Ever-Glo IR source, XT-KBr beamsplitter, and MCT-A (mercury cadmium telluride, or HgCdTe) detector were chosen. Visible range spectroscopy is possible, for example, with the addition of a second detector (silicon) and beamsplitter (quartz), and servicing by Thermo Scientific. In its current state, the FTIR spectrometer can be used to study samples in the range of 7000 cm^{-1}–600 cm^{-1} (1.4 μm–16.7 μm). Free-space wavelength and wavenumber are related by the following simple expression:

$$\lambda\ (\mu\mathrm{m}) = \frac{10^4}{\omega\ (\mathrm{cm}^{-1})}, \tag{7.11}$$

where λ is the wavelength in microns (μm) and ω is the wavenumber in inverse centimeters (cm^{-1}). The wavenumber ω, which should not be confused with

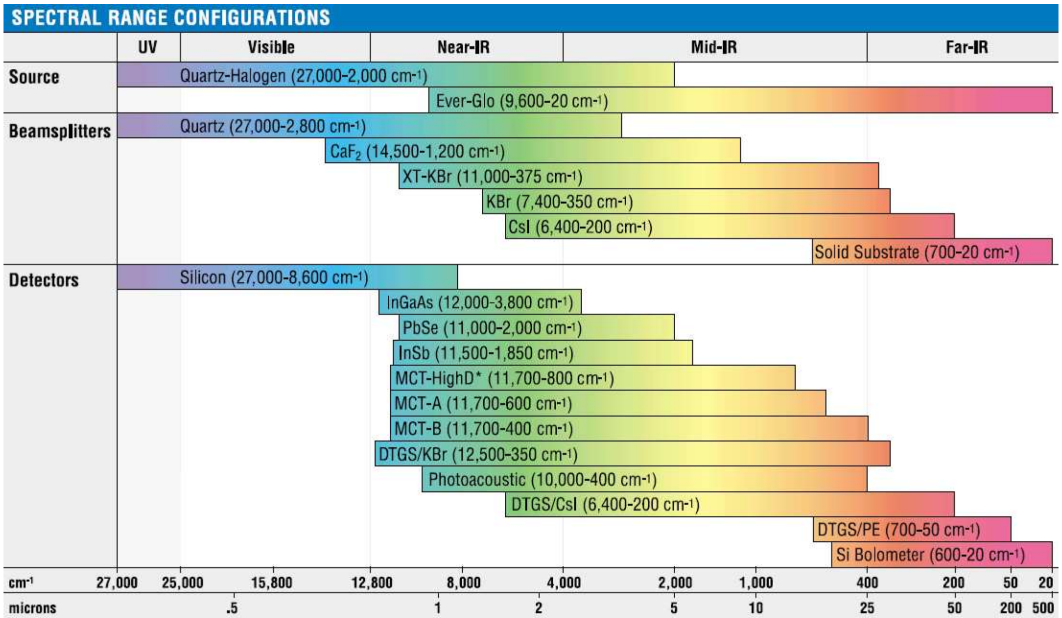

Figure 7.3: Spectral range configurations of the Nicolet 6700 FTIR spectrometer, as defined by the source, beamsplitter, and detector. Courtesy of Thermo Scientific.

angular frequency, is related to photon frequency ν through the expression ν (Hz) $= \omega$ (m^{-1}) c (m s^{-1}), where $c = 3 \times 10^8$ m s^{-1} is the speed of light.

The typical FTIR radiation power delivered to a sample is less than 1 mW [97]. This power is many orders of magnitude less than that delivered by CO$_2$ lasers (P $>$ 1 W), but by using ultra-sensitive, liquid nitrogen-cooled detectors, lock-in signal processing, and multi-hundred-scan averaging, high-quality spectra result from FTIR spectroscopy.

The FTIR spectrometer meets the Lab's broadband IR spectroscopy needs. But, as discussed above, the analysis of sub-mm samples is impossible because light is not focused to such dimensions. Polarizing and analyzing light is not natively integrated into the system, and reflection measurements would require additional equipment. For these reasons, an IR microscope was purchased and is currently in use.

7.3 Infrared Microscopy

Microscopy is a powerful method because it enables the study of microscale optical samples (typically $(50\ \mu\mathrm{m})^2$ to $(100\ \mu\mathrm{m})^2$). But with such resolving power, understanding the incidence angle and divergence properties of an IR microscope becomes critical to proper sample analysis. The Perkin Elmer Spectrum GX AutoImage microscope is located at the University of Texas at Dallas and was used from 2004–2008 for such projects as those presented in Refs. [59, 108]. The Thermo Scientific Continuum microscope was purchased by the Laboratory in 2008; the instrument was used to analyze many samples, including those presented in Refs. [58, 68], and will be discussed below.

7.3.1 IR Microscope Imaging Capabilities

Infrared microscope beams are directed by Cassegrain optics as schematically shown in Fig. 7.4, solely comprised of reflective surfaces. In practice, the incident beam, once focused, propagates into the page (i.e., left to right when facing the instrument) in reflection mode. The objective (located above) and condenser (located below) consist of larger primary and smaller secondary reflecting mirrors that, by their geometric configuration, determine the average

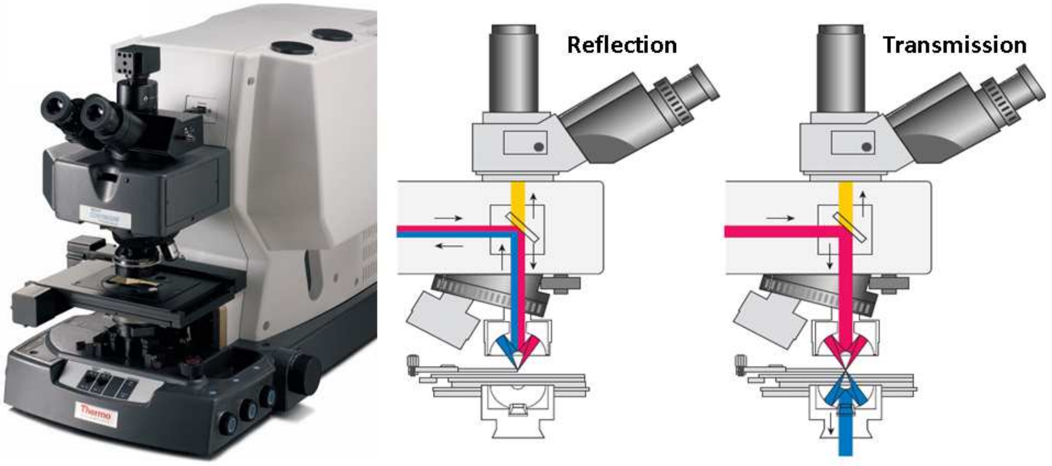

Figure 7.4: A photograph (left) and schematic views of the Thermo Scientific Continuum IR microscope. The reflection and transmission modes are given as labeled. Courtesy of Thermo Scientific.

angle of incidence, the numerical aperture (which describes the light-gathering power), and the final magnification (M). The numerical aperture (NA) is a dimensionless value that represents the angular range over which an optical element can accept radiation [11]:

$$NA = n\sin(\theta) = n\sin\left(\arctan\left(\frac{D}{2f}\right)\right) \approx n\frac{D}{2f}, \tag{7.12}$$

where n is the refractive index of the medium between the optical element and the focus, θ is the half-angle of the light cone that can enter or exit the element, D is the element's diameter, and f is the element's focal length.

The Continuum microscope has an angle of incidence of $\theta = 25°$, $NA = 0.58$, and $M = 0.067$ (or "15×," where objects are magnified fifteen times). The large NA and M result in a tightly focused beam—as small as

$(50\ \mu\text{m})^2$. Nearly all radiation transmitted through the aperture at the first (inner) focal plane is delivered to the sample at the second (outer) focal plane. In fact, radiation is so efficiently delivered to the detector that attenuation is needed to prevent saturation. Attenuation is typically achieved by reducing the J-stop iris to a minimal value and, if needed, placing a perforated-metal neutral density filter in the beam path between the FTIR spectrometer and the microscope. Although the detector monitors signals from 0–12, a raw signal of ≤ 1.0 has given reliable, non-saturated data. The resulting high signal-to-noise ratio and small spot size of the microscope come at the expense of strong convergence (wavevector averaging) and a short working distance, however. These limitations will be addressed below.

Radiation is polarized when its electric field $\mathbf{E}$ is aligned in and oscillates along only one dimension, as depicted in Fig. 7.5. A wire-mesh polarizer (e.g., ISP Optics, 2400 lines/mm) is used to "polarize" radiation before the sample or "analyze" after the sample. The polarizer is located just above the objective, and the analyzer just below the condenser. In both cases, the radiation passing through the polarizer is collimated. In transmission mode, polarized/analyzed studies have be performed, e.g., to explore the chirality or polarization-rotating ability of a metamaterial (as discussed in Ch. 5). But such studies are not currently possible in reflection mode because the 1" diameter polarizer encounters the entire beam, thus polarizing the incident radiation *and* analyzing the reflected radiation; this is one reason for the expansion of an external beamline.

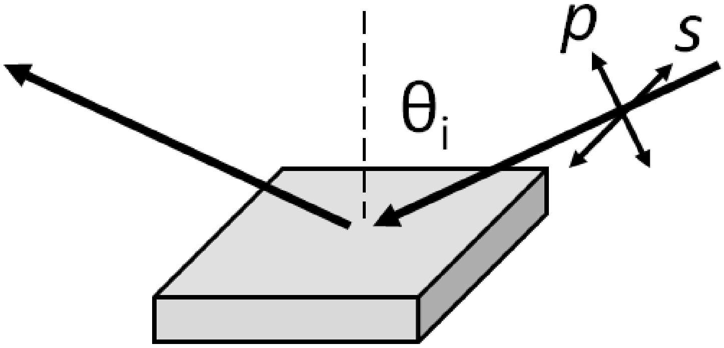

Figure 7.5: A schematic of s and p polarization, where the arrow represents the electric field vector. For s polarization, the electric field $\mathbf{E}$ is parallel to the x–y surface for all angles θ. For p polarization, the magnetic field $\mathbf{H}$ is parallel to the surface, while the $\mathbf{E}$ component into the plane surface z is referred to as E_z and is finite for non-zero θ.

7.3.2 Raw Output Polarization Analysis

When fixed-incidence-angle, polarization-rotating reflection studies are required, they can be *indirectly* performed with the IR microscope. Ideally, a direct measurement of radiation rotated through otherwise crossed polarizers is preferred. But rotated reflection intensity may be required if the substrate is thick or excessively absorptive, and it can be indirectly inferred by collecting the following reflection spectra: unpolarized/unanalyzed (u/u), p-polarized/p-analyzed, and s-polarized/s-analyzed. Assuming incident radiation is totally unpolarized, subtracting the average of p/p and s/s from u/u yields the intensity deficit because any rotated light will not be screened in the u/u case. But radiation is not completely unpolarized: careful steps were taken to account for s and p polarization mixing delivered to the microscope's focal plane. With

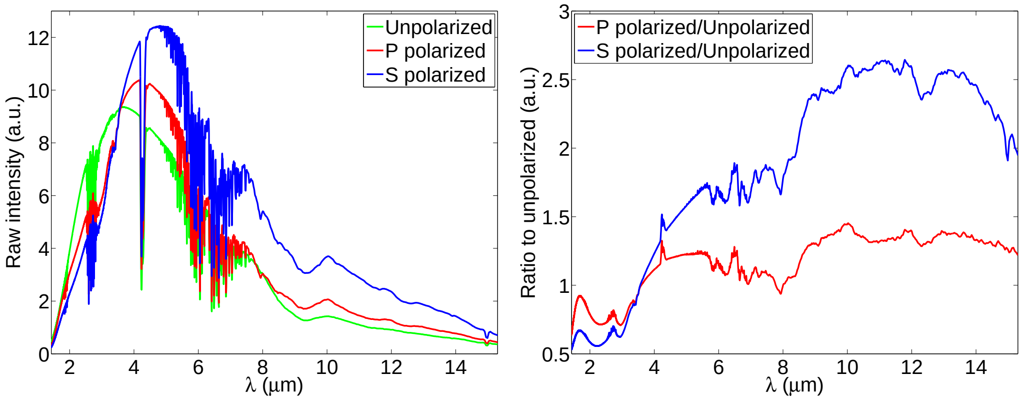

Figure 7.6: Left: Raw, open transmission spectra collected with the FTIR microscope. While *s* and *p* polarized data were collected using one fixed incident radiation intensity, the unpolarized spectrum was attenuated to ensure that intensity-dependent detector nonlinearities would not affect results. Right: polarized spectra normalized to the unpolarized spectrum (in arbitrary units; only relative values are of interest).

this mixing known, a more accurate calculation can be performed.

To determine the relative distribution of *s* and *p* polarization in unpolarized light, three raw mirror reflection spectra and three raw open transmission spectra were collected with the microscope. While the raw reflection results (not shown) will be used for calculating reflection rotation in future samples, the transmission results will be presented here (Fig. 7.6, left) because a comparison can then be made between direct and indirect polarization rotation results, as given below. The data presented consists of an unpolarized and unanalyzed spectrum, a *p*-polarized and *p*-analyzed spectrum, and an *s*-polarized and *s*-analyzed spectrum. The polarized and analyzed transmission collection (i.e., two polarizer passes) is required because both incident and reflected radiation interacts with the objective polarizer in reflection mode (also two polarizer passes). The intensity of the unpolarized spectrum was attenuated with the J-stop iris to match the two-polarizer-case intensity to ensure that detector nonlinearity, which depends on incident power, does not affect the polarization tests. As shown in the right panel of Fig. 7.6, the two polarized cases are normalized to the unpolarized case. Note that in both Fig. 7.6 panels, arbitrary units are used because only the relative balance of power between s and p polarizations is desired.

It should be noted that an analysis on the FTIR spectrometer's output power distribution was done. The unpolarized transmission spectrum of Fig. 7.6 was converted back into the native frequency scale (cm^{-1}) where spacing between data points is uniform. The spectrum was integrated over frequency, and the data point that bisected the distribution was noted. The frequency $\omega = 3192\ \text{cm}^{-1}$ (and wavelength $\lambda = 3.13\ \mu\text{m}$) thus corresponds to the spectral position at which half of the total IR power lies to either side: i.e., the power spectrum's central frequency has been identified. This numerical finding becomes more important in Ch. 8.

The polarization balance was found by calculating each polarization's deviation (above or below) from the average of the two. The final results of these experiments are presented in Fig. 7.7: the left panel gives each polarization as a fraction of unpolarized light as a function of wavelength (μm). The right panel gives the same as a function of wavenumber (cm^{-1}) to show how the system is more balanced (i.e., 50/50) in frequency space. With this

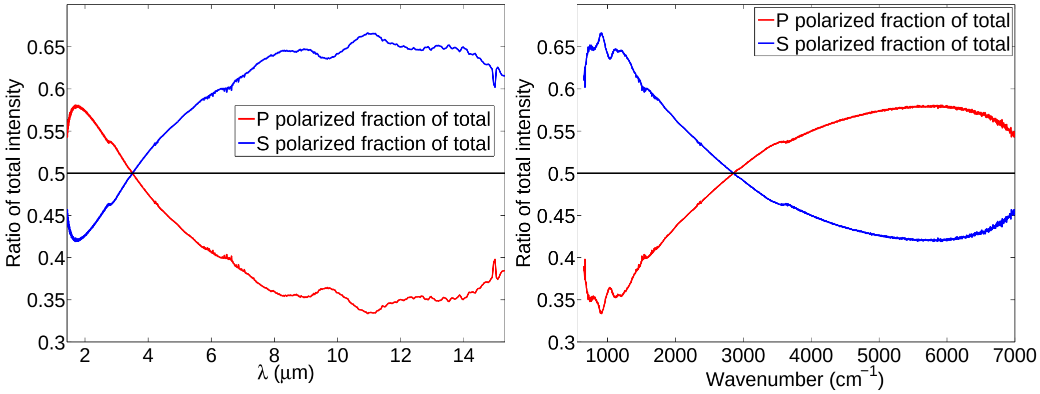

Figure 7.7: Intensities of s and p polarization as a fraction of unpolarized light delivered to the microscope in transmission mode, presented as a function of wavelength (left) and wavenumber (right). Spectra are plotted vs. wavenumber to show that polarization is approximately balanced in frequency space.

understanding, polarization rotation calculations now follow.

The indirect method of determining polarization rotation was tested on the rectangular aperture-based spoof surface plasmon structure of Ch. 5, which is known to rotate polarization in transmission mode. Therefore, indirect and direct methods could be compared (Fig. 7.8). To analyze polarization-rotating properties, the light polarization and array orientations remain fixed while the rectangle's rotation within the unit cell varies. Angles θ refer to the displacement from the rectangle's long axis to the radiation's electric field direction. Variations were therefore performed not by physical rotations but by fabricating multiple structures. A detailed analysis on this work is underway [57] with the support of S. Hossein Mousavi and Alexander B. Khanikaev.

As observed in Fig. 7.7, light emitted from the FTIR is not perfectly unpolarized, but instead s or p polarization may dominate at certain frequencies. The method of indirectly determining polarization rotation must then take frequency-dependent mixing into account through the following expression:

$$I_{rotated} = I_{u,u} - (I_{p,p} * f_p + I_{s,s} * f_s) \, , \tag{7.13}$$

where I is the reflection or transmission intensity, $I_{u/p/s,u/p/s}$ is the intensity of light interacting with a sample that has been *un*-, p-, or s-polarized and analyzed, and $f_{p/s}$ is the fraction of p or s polarization in the incident radiation. The resulting $I_{rotated}$ yields the total polarization rotation exhibited by a sample, and can be directly compared to the chiral structure spectra. Since the calculation describes all possible rotations, the mean of two experiments is used for comparisons: p-polarized and s-analyzed spectra, and s-polarized and p-analyzed spectra. Figure 7.8 shows the direct (top) and indirect (bottom) polarization results: it is clear that quantitative agreement is poor, as the baseline is shifted by a few percent, and the peak positions do not perfectly agree, but the procedure is useful for an initial qualitative understanding. Indeed, indirect measurements would be improved by a higher signal-to-noise ratio (increasing incident power) and more scans (additional averaging for smoother curves).

Again, this technique is currently imperfect, yielding results better for qualitative analysis, but improvements are possible. The more obvious choice, however, motivates the construction of an external FTIR beamline to explore polarization rotation. But now, a description of the IR microscope's focusing capabilities, as determined through experiments, follows.

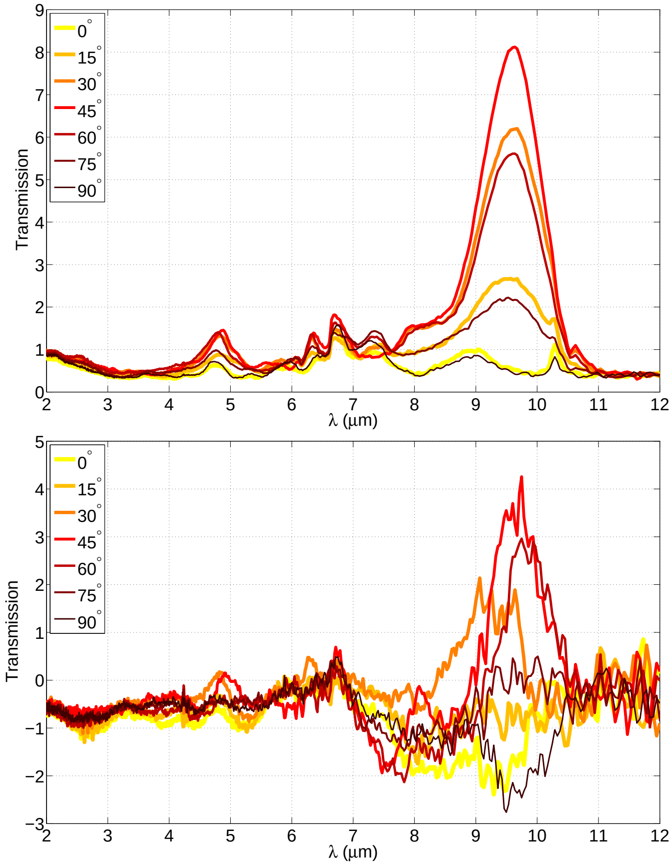

Figure 7.8: Direct (above) and indirect (below) experimental transmission polarization rotation within a metamaterial structure, presented as an example of the microscope's capabilities. The structure consists of a 100-nm-layer of Au on a 1000-nm-layer of 3C-SiC air-bridged membrane. The Au film is patterned with multiple square arrays of rectangular holes whose long axes are oriented at variable angles with respect to the lattice (see Ch. 5).

7.3.3 IR Microscope Focusing Performance

To determine the actual geometrical characteristics of the probing IR microscope beam, its cross-section was analyzed using a pinhole in two focal planes. The internal square aperture was set to (50 μm)^2, and the pinhole

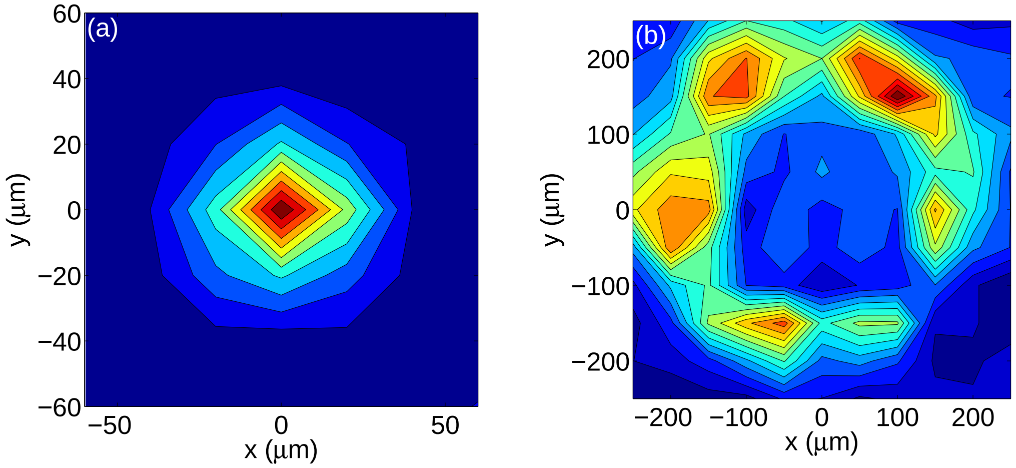

Figure 7.9: Infrared radiation profiles for the Shvets Laboratory Thermo Scientific Continuum microscope in transmission mode. An aperture of (50 μm)^2 was set, and a 40 μm-diameter pinhole was manually scanned (a) in the focal plane and (b) 400 μm above the focal plane. Radiation is contained as specified in (a); deviation from the expected square profile results from manual (non-electronic) stage alignment. (b) The six-lobed converging annulus above the focal plane results from the objective's inner-mirror mechanical support structure.

was scanned in (x,y) to determine focal dimensions and divergence properties of the Continuum microscope. Figure 7.9 (a) shows the result of transmission through a 40-μm-diameter pinhole scanned in the focal plane: radiation is indeed focused to the specifications. The non-square profile results from (i) using an aperture that is not much smaller than the beam and (ii) from manually scanning the pinhole with low resolution and accuracy; an electronic stage would enhance positioning.

The same pinhole was then scanned 400 μm above the focus: Fig. 7.9 (b) maps the microscope beam distribution. Clearly, radiation propagates toward the focus with an annular profile. This profile leads to an imperfectly defined polarization. With convergence from the 360° annulus, perfect polarization is not possible. The six observed regions coincide with the inner mirror's support structure. Polarization is marginally better defined in reflection mode: shown schematically in Fig. 7.4, incident light propagates through the left half of the objective, reflects from the sample, and is collected in the opposing right half. Light is more localized to one propagation direction, but still converges with a non-circular (e.g., non-laser-like) profile.

7.4 Conclusions

The benefits of Fourier transform infrared (FTIR) spectroscopy have been presented. By rapidly collecting low-power signals over a broad spectral range—from the near-IR to the terahertz—the FTIR spectrometer coupled to the IR microscope has proven its utility in optical sensing and material characterization. In Sec. 7.3, it was shown that the use of an infrared microscope gives users the ability to quickly collect reflected and transmitted radiation from samples as small as $(50\ \mu\text{m})^2$. Rapid analysis is enabled because the reflecting objective also focuses visible light, which is directed through an IR/visible beamsplitter (Fig. 7.4), and allows for quick visual sample alignment. But the IR microscope's unconventional convergence may contribute to (i) unpredictable wavevector averaging in the focal plane and (ii) imperfectly defined polarization (i.e., not purely *s*- or *p*-polarized radiation). When additionally considering the inability to vary incident angle, the need for advanced beam control is motivated. In the next chapter, the external beamline based on FTIR spectroscopy is detailed.

Chapter 8

Angle-Resolved Optical Beamline Based on FTIR Spectroscopy

8.1 Introduction

The infrared microscope's unconventional convergence, atypical polarization state, and fixed angle of incidence makes the analysis of certain optical metamaterials difficult or impossible. To gain advanced control of the infrared beam, a novel beamline external to the FTIR spectrometer was proposed. Serving as the main experimental objective of this dissertation work, the beamline demonstrates (i) wavelength-tunability from 1.4 μm–16.7 μm, (ii) incidence angle-variability from 0° to nearly 90°, (iii) better polarization control than the microscope (i.e., more clearly defined s and p polarization), and (iv) the ability to probe samples as small as 200 μm in diameter (or smaller, with numerical renormalization).

In Sec. 8.2, an overview of the beamline will be presented, followed in Sec. 8.3 by a description of the methods used to control and direct the beam with respect to the optical table. The off-axis parabolic mirror, which focuses radiation onto an intermediate pinhole, will be presented in Sec. 8.4, along with procedures used for mirror alignment. The setup and usage of the object-defining pinhole and the aspherical ZnSe lens are detailed in Sec. 8.5 and Sec. 8.6, respectively. After an analysis on total transmitted power is presented (Sec. 8.7), beamline properties as characterized through polarization, focal diameter (Sec. 8.8), and chromatic dispersion (Sec. 8.9) are given. In Sec. 8.10, the process of numerical renormalization—which accounts for beam/substrate interaction—is presented and verified using a $(150\ \mu\text{m})^2$ metamaterial array of "pi" structures. Finally, Sec. 8.11 presents a verification of the external beamline's ability to resolve angle-dependent metamaterial resonances through the analysis of an array of Au antenna pairs.

In this work, all beamline design, setup, characterization, and usage were performed by the author, but much useful advice was given by many group members. The "pi" structure metamaterial of Sec. 8.10 was fabricated by Nihal Arju, modeled by Chihhui Wu, and spectrally analyzed with the IR microscope and the external beamline by the author. The array of Au antenna pairs in Sec. 8.11 was fabricated by David Fozdar, numerically modeled by S. Hossein Mousavi and Alexander B. Khanikaev, and spectrally analyzed by the author.

8.2 Overview of the Novel FTIR Beamline

Past articles [47] have discussed similar experimental setups where the FTIR spectrometer beam is focused onto a sample for angle-dependent studies, but samples have been larger (mm-scale), and it is unclear whether small spot sizes ($\leq 200\ \mu$m) are demonstrated with such setups. Similar to the IR microscope, the usage of an intermediate optical “object” aperture can provide a controllable “image” spot size in the target focal plane. When the optical system provides magnification, the resulting image is scaled by the factor M; for $M > 1$, the image is expanded in size, while for $M < 1$, the image is reduced in size, as desired in microscopy. In this work, the object’s image will be reduced in size, resulting in a 200-μm-diameter focal spot.

As depicted in Fig. 8.1 and shown in Fig. 8.2, the external optical setup begins with the IR beam. At this point, the beam has been collimated, passed through the interferometer (so that software can correlate mirror position with time to deduce frequency dependence), and directed to the side of the FTIR spectrometer mainframe. The beam is $\leq$ 1.5" in diameter, and must be further directed to (i) optimize the layout of the optical table and (ii) ensure the beam propagates parallel to the table surface. Steering is achieved with a large 3"-diameter mirror, designated as M_4. Note that where possible, large optics have been used to maximize light collection (or throughput), because only a small fraction of incident light is actually delivered to the target; total power will be analyzed in Sec. 8.7. The design, setup, and characterization of the novel beamline now follow.

8.3 Beam Control and Divergence

The infrared beam emerges from the FTIR spectrometer collimated, and propagates co-linear with a red ($\lambda = 632.8$ nm), low-power HeNe laser. The internal HeNe laser is used by the system during fixed mirror (M_F in

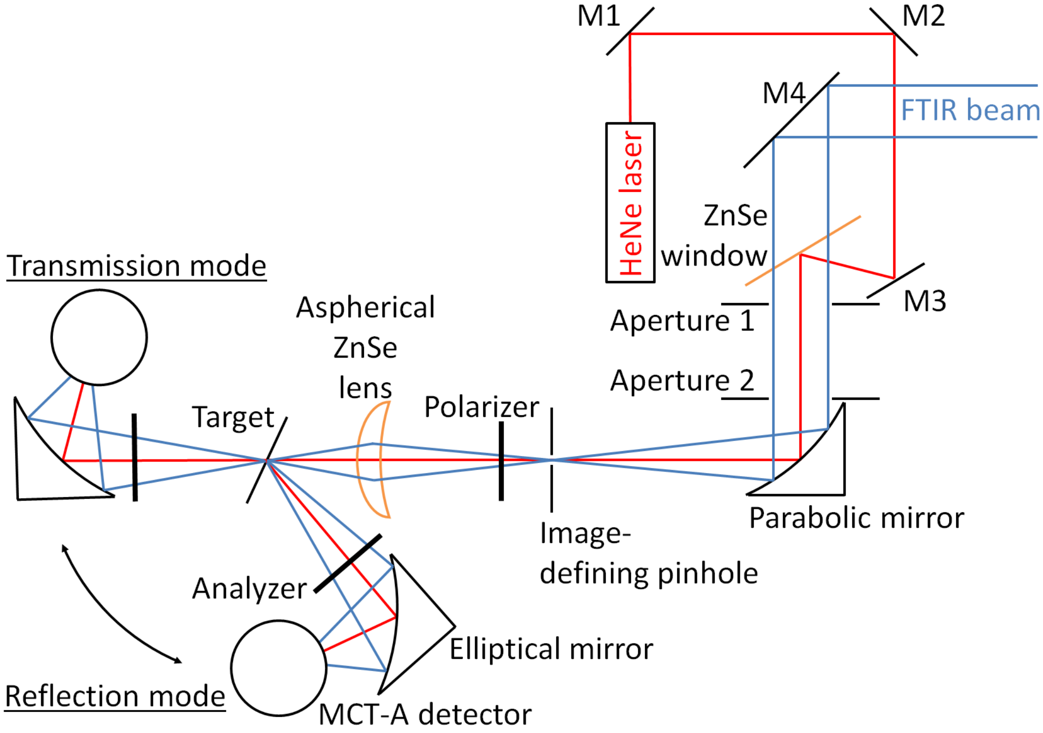

Figure 8.1: A schematic representation of the external optical setup (not to scale). External IR beamline manipulation permits sub-mm spot sizes, with polarization control, divergence control, and variable-incidence-angle control not available with the FTIR spectrometer or IR microscope.

Fig. 7.1) calibration to achieve optimal interferograms. To make the IR beam parallel to the table, the internal HeNe laser is monitored as it passes through an iris; the IR beam is parallel to the table when the laser passes through the center of the iris when the iris is located both near (<1") and far (>24") from M_4. The mirror M_4 resides on a translation stage to permit linear translations toward or away from the IR beam source.

The IR beam passes through a ZnSe planar window that is set to a

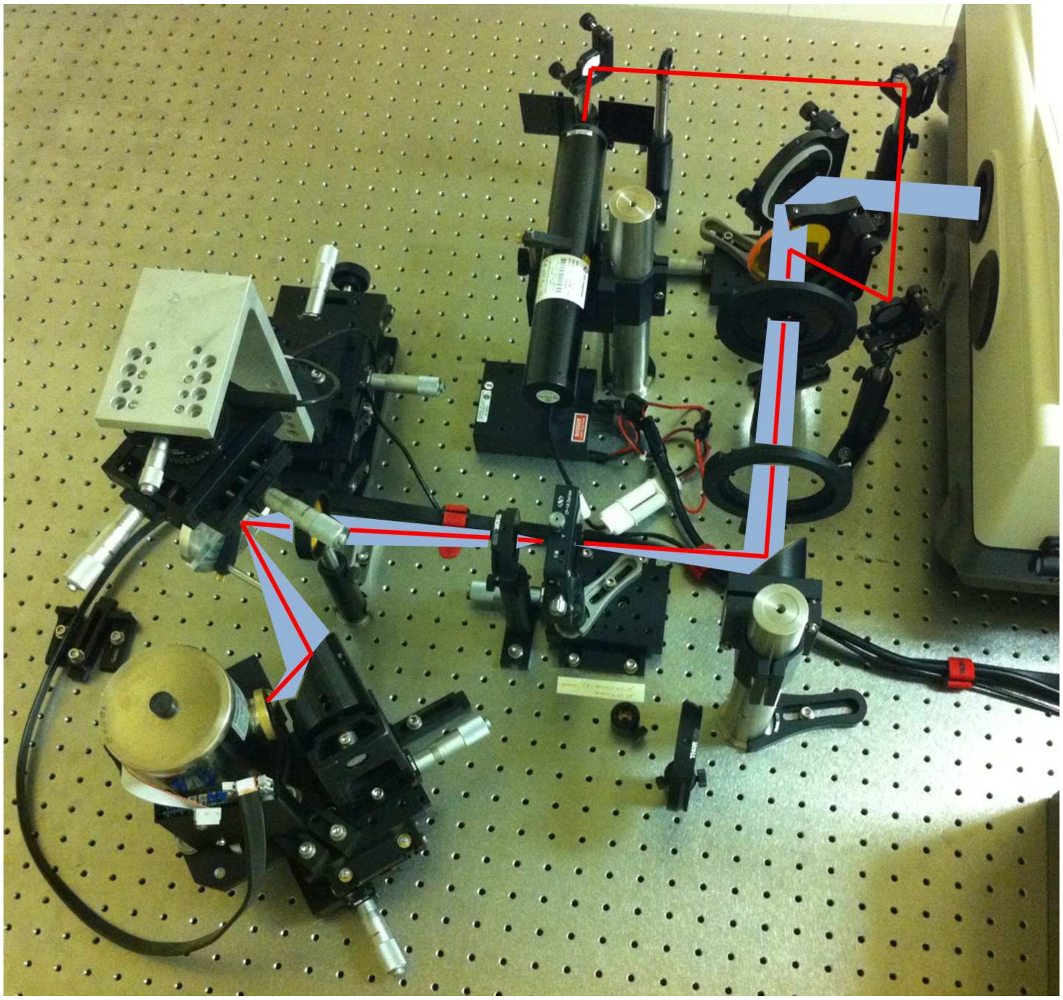

Figure 8.2: A photograph of the external optical setup based on the FTIR spectrometer. A red HeNe laser is combined with the invisible IR beam for alignment purposes.

shallow angle (∼30°). The window allows a more powerful external HeNe laser to propagate along the same path as the IR beam. With the beam parallel to the table's surface, it must now be aligned with the array of optical table holes for straightforward alignment of other optics. Large apertures 1 and 2, which vary from 0.0"–2.5" in diameter, are directly screwed into the table to ensure their alignment with the hole rows. After the aperture heights are matched to the IR beam, the beam can be horizontally steered with M_4 thumbscrews to pass through the aperture centers. The M_4 stage then allows for horizontal translations to achieve optimal aperture alignment.

With the large apertures in place and the beam aligned through their centers, collimated IR beam divergence can be experimentally determined. The apertures are exactly 6" apart in the optical table, and aperture 1 is set to $D_1 = 0.70$" diameter, defining the beam's width. As shown in Fig. 8.3, aperture 2 is then reduced from large to small diameters, and the threshold beyond which transmitted energy is blocked is noted. This threshold occurs at $D_2 = 0.75$" and corresponds to the beam's expanded diameter that results from divergence. Angular divergence is calculated as

$$\phi_{exp} = 2\tan^{-1}\left(\frac{[0.75\text{"} - 0.70\text{"}]/2}{6\text{"}}\right) \tag{8.1}$$

which results in moderate divergence of $\phi_{exp} = 8$ mrad, or 0.5°.

With collimated external beamline divergence determined, a comparison to theory can be made. The Jaquinot stop is the internal FTIR spectrometer iris that, in conjunction with mirror translation, sets the resolution of the system: as the iris is reduced to its smallest value of 0.75 mm, divergence is also reduced, permitting higher resolution interferograms. Divergence is related to the iris diameter ($D_i = 0.75$ mm) and to the focal length of the optical element (within the spectrometer) that collimates radiation (a

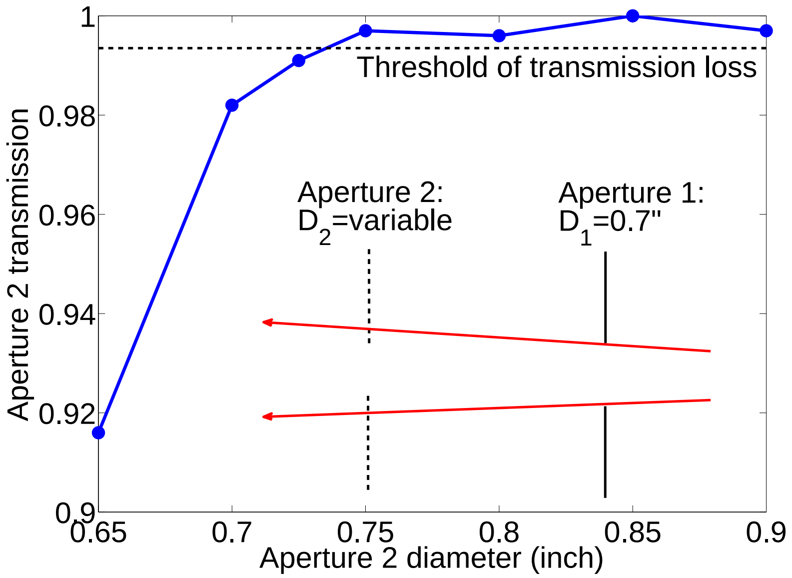

Figure 8.3: Transmission through fixed aperture 1 and variable aperture 2 is used to determine infrared beam divergence. The apertures are separated by 6", and the horizontal dashed line indicates the threshold after which radiation is blocked by aperture 2. Expansion of the 0.70" beam to 0.75" over a 6" propagation distance corresponds to a maximum angular divergence of 8 mrad, or 0.5°.

parabolic mirror of $FL_{pm} = 6" = 152$ mm). Predicted divergence is then $\phi_{th} = 2\tan^{-1}(0.5D_i/FL_{pm})$ [53], so $\phi_{th} = 5$ mrad, or 0.3°. As expected, experimental divergence is slightly larger than theoretical divergence ($\phi_{exp} > \phi_{th}$).

The diameter of a diffraction-limited focal spot is represented by

$$D_{dl} = \frac{1.22\lambda}{n\sin(\theta)}, \tag{8.2}$$

where λ is the free-space wavelength, n is the refractive index of the medium between the focusing element and the focal plane, and θ is the half angle of converging incident radiation [11]. For $\lambda = 5\ \mu$m (approximate center of the wavelength spectrum), and assuming a 0.5"-diameter beam (which leads to a $\sim 2.5^\circ$ half-angle using the parabolic mirror), diffraction-limited focusing yields $D_{dl} \sim 150\ \mu$m. In contrast, moderate experimental divergence (8 mrad), coupled with the usage of 6"-focal length mirrors lead to focal spot diameters larger than the diffraction limit. The external beamline parabolic mirror (Sec. 8.4) focuses IR radiation to a 1.2-mm spot (a product of experimental divergence and mirror focal length), nearly an order of magnitude worse than that predicted by diffraction-limited focusing. Lower experimental divergence and shorter focal length optics would provide focusing closer to the diffraction limit, but these options are not readily possible: divergence cannot be further reduced, and shorter focal lengths would result in larger angular beam spread (focal convergence). With such limitations known, geometrical principles [11] are best suited for the optical calculations performed in the remainder of this chapter, and it will be shown that a small focal spot size (200 μm) is nevertheless achieved.

With collimated beam divergence understood, the external HeNe alignment laser is considered. The laser is significantly brighter than the FTIR spectrometer's internal alignment laser, making it better suited for target alignment. The mirrors M_1, M_2, and M_3 of Fig. 8.1 direct the laser to the ZnSe window, from which it reflects and continues along the same path as the IR beam. The external HeNe laser undergoes final alignment with the IR beam by closing the two large apertures to small diameters and adjusting M_2 and M_3 for optimal throughput. The diameter of aperture 2 is then set 0.5", which defines the (i) collimated beam width and (ii) angular beam spread for the remainder of the system (shown in Fig. 8.4 and discussed in Sec. 8.6 and Sec. 8.7). The IR beam and HeNe alignment laser are now co-linear; setup and alignment of the first focusing element—the off-axis parabolic mirror—is now addressed.

8.4 Off-Axis Parabolic Focusing Mirror

Reflecting focusing optics have one main advantage over dielectric refracting lenses: because focal properties are only determined by geometry, there is no chromatic aberration. But reflective focusing optics require extremely complex and expensive procedures for near-perfect alignment—the type of alignment required when focusing radiation into a sample's target plane. Indeed, complicated methods to align off-axis parabolic (OAP) mirrors to near-perfect conditions using interferometry have alone resulted in article publications [13]. However, when less-exacting alignment and focusing is adequate, simplified procedures can be used, and OAP mirror use is desirable. The OAP mirror employed in the external beamline focuses IR radiation to a spot larger than 1 mm, which is greater than the 400-μm-diameter pinhole placed at this intermediate focus, thus explaining why slight misalignment will not greatly affect system performance.

The external setup's OAP mirror (Janos Tech, Keene, NH) directs focused radiation 90° from the incident beam. The mirror's specifications (6" focal length, 2" diameter) match those of the parabolic mirrors within the FTIR spectrometer, which implies that they all have the same numerical aperture (NA) and light-gathering power. For the external OAP mirror, the maximum numerical aperture (which was defined in Eq. 7.3.1) is $NA = 0.16$. Larger NA therefore refers to optical elements that intercept a larger solid angle of light. But with larger NA and light-gathering power come limitations. The resulting large convergence/divergence leads to (i) significant wavevector averaging (one problem identified with the IR microscope) and (ii) the requirement to match all subsequent optics with the same NA (unmatched optics result in uncollected radiation). Conversely, longer focal lengths and more distant sample placements will result in reduced divergence, but intensity will be lost. Because each optical element affects the total system throughput, a power analysis will be presented in Sec. 8.7.

While small deviations from perfect lens alignment do not typically generate large optical aberrations or beam misalignments, mirror alignment, as stated above, is more critical. The aberration *coma* is generated when off-axis rays illuminate the mirror [62], and can severely distort the image. Rotating 1° from perfect alignment would displace a lens' focal position by a negligible distance, but such a rotation would likely displace the mirror's focal position on the order of millimeters. To minimize aberrations, laser alignment was performed on the OAP mirror. The novel method requires two parallel HeNe beams [62]: by passing two laser beams (which are parallel to each other and to the optical table) into the OAP mirror, far field iris measurements can be performed to ensure that the mirror's axis is aligned with respect to the incident radiation. The setup for this procedure is detailed in Ref. [62], but the implementation will be briefly discussed here.

A beamsplitter optimized for HeNe radiation was placed after the laser (not shown in Fig. 8.1). Additional steering mirrors are placed near M_1 and M_2 to make the new, secondary HeNe beam parallel to the table and to the primary HeNe beam. Both beams then reflect from M_3 and the ZnSe window, and propagate toward the parabolic mirror. The procedures outlined in Ref. [62] are then followed and result in sufficient alignment and focusing of (i) the IR beam and (ii) the external HeNe alignment laser.

8.5 Object-Defining Intermediate Pinhole Alignment

The OAP mirror, now aligned, will focus IR radiation to a spot approximately equal to or larger than the internal FTIR spectrometer J-stop diameter because all focal lengths up to this point are equivalent (which yields a geometrical-optics magnification $M = 1$, as discussed in Sec. 8.3). The J-stop iris diameter ranges from 0.75 mm (software setting "APT 0") to 8.75 mm ("APT 100"), but the smallest value will be used in most or all experiments. A small x-y translation mount for 1"-diameter optics holds and aligns an optical object-defining pinhole, and resides on a z translation stage. The z stage places the pinhole at the mirror's focus (Fig. 8.1). The coordinates x and y refer to directions horizontal (in the plane of the table) and vertical (out of the plane of the table) to the IR beam, respectively. The coordinate z refers to the propagation/focal direction. The pinholes are ultra-thin (12.5 μm) steel films with sub-mm apertures, mounted on 1"-diameter disks. Through experiments it was found that a 400-μm pinhole provides an appropriate object size for the lens to image, while still transmitting sufficient power (pinhole selection will be further addressed in Sec. 8.8). Therefore, perfect OAP mirror alignment (which is difficult) is not required: light will be focused to a spot larger than the 400-μm pinhole, so small mirror misalignments will not dramatically alter throughput. A 1"-diameter wire-grid polarizer (0.7" clear aperture) is placed after the pinhole; it resides in a 360° rotation mount, providing any degree of polarization required, and can be removed when unpolarized light is desired (with the added benefit of increased intensity). Additionally, a second, removable polarizer resides between the sample plane and the detector, serving as an "analyzer" for cross-polarized studies.

The 400-μm pinhole must be properly aligned in x, y, and z to establish an ideal optical object. To do so, the detector apparatus monitors transmitted power as the pinhole's position is optimized. As discussed above, MCT-A detectors were originally installed in (i) the FTIR spectrometer and (ii) the IR microscope. Spectrometer components are "plug and play;" they are constructed with steel dowel pins and thumbscrews for simply removal and replacement. Furthermore, the spectrometer sample chamber and detector were unused, so the detector was reassigned to the external experiment. Because the detector's single-pixel active element is sub-mm in scale, a focusing element must be used.

An elliptical mirror (Fig. 8.1) included with the spectrometer focuses radiation onto the detector. Such mirrors are ideal for translating one focal point to another; in the case of the external beamline experiment, the mirror is placed $\sim$ 6" from the pinhole, which focuses light $\sim$ 2.5" away onto the detector element. The mirror–detector assembly resides on an x-y-z stage of its own (Fig. 8.2) so that small adjustments can be made to optimize the detected signal. It should be noted that software problems arise if both external beam and IR microscope detectors are simultaneously connected: when using the microscope, the external-beam detector should be unplugged at its circuit board; when using the external beamline, the microscope's accessory cable located at the rear of the spectrometer should be unplugged. With the detector assembly in place, the pinhole's position is optimized in three dimensions. With a 400-μm optical "object" established, the task of imaging the object into the target plane was undertaken.

8.6 ZnSe Aspherical Focusing Lens

A 2"-diameter, 2"-focal length aspherical ZnSe lens was chosen to focus the image into the target plane because lenses (i) tolerate alignment imperfections better than OAP mirrors and (ii) greatly simplify initial alignment and realignment procedures. The yellow-tinted ZnSe lens is transmissive in the visible and IR ranges, making it an ideal material for IR spectroscopy with visible beam alignment. It is slightly dispersive (frequency-dependent index of refraction), which leads to chromatic aberration, or dependence of the focal position on frequency; this will be fully characterized in Sec. 8.9. The

2" diameter was chosen to maximize its numerical aperture, as it is desired to collect as much light as possible. Standard biconvex or plano-convex lenses are typically used in laser experiments because their simple geometry (a spherical section) allows for low-cost manufacturing. But in cases where (i) the entire lens may be illuminated (large off-axis rays) or (ii) ideal, aberration-free focusing is required, a more expensive aspherical lens—which has a higher-order polynomial deviation from a spherical profile—is useful. Both (i) and (ii) are present in this experiment and benefit from the aspheric design.

As the lens' object distance is increased, the focal spot (image) will be reduced in size, but the lens will intercept a smaller solid angle of radiation. The relationship between the focal length, object distance, and image distance can be approximated by the thin lens formula [11]:

$$\frac{1}{f} = \frac{1}{p} + \frac{1}{q}, \tag{8.3}$$

where f is the lens' focal length, p is object distance (object-to-lens distance), and q is the image distance (lens-to-image distance). It was determined that the optimal conditions (small focal spot with sufficient intensity) were achieved using $p = 8"$, which yields an image distance $q = 2.66"$ and a magnification $M = 0.33$, as depicted in Fig. 8.4. The magnification can be determined via two relations as

$$M = \left|\frac{q}{p}\right| = \left|\frac{i}{o}\right|, \tag{8.4}$$

where i is the size (diameter) of the image and o is the size of the object. Using the pinhole diameter of $o = 400$ μm, the image should be $i = 133$ μm,

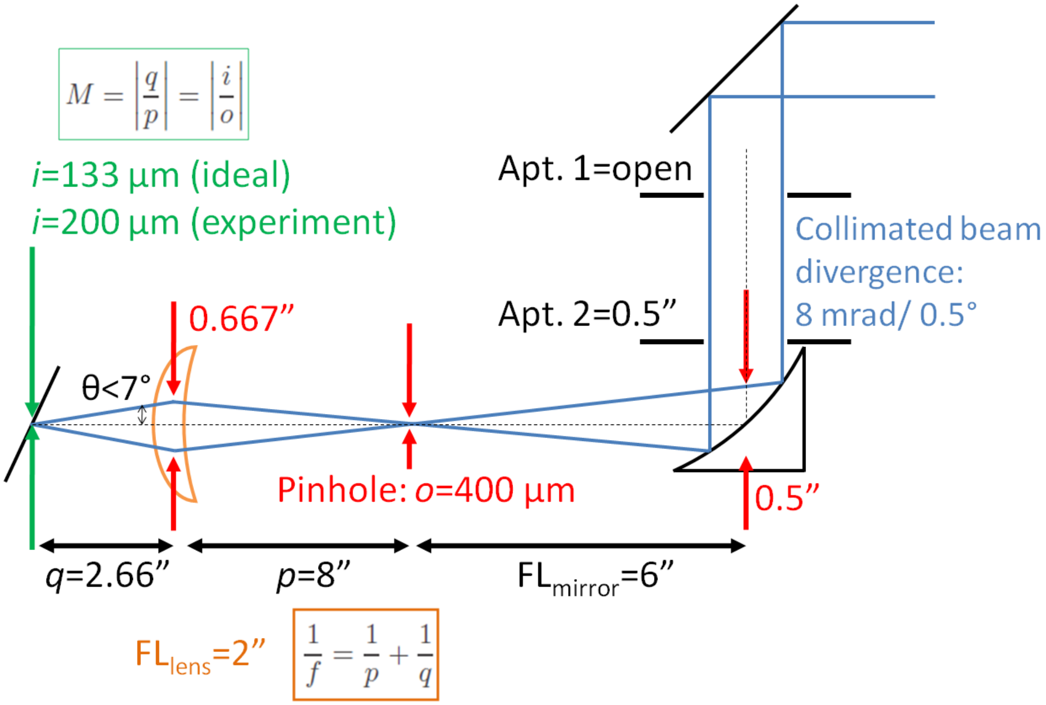

Figure 8.4: External beamline schematic with focal property-defining dimensions specified. Moderate beam divergence prevents diffraction-limited focusing, but through geometrical optical principles, it is shown that a sufficiently small focal spot (200 μm) is achieved. The collimated beam diameter determines the focal convergence angle (and thus the numerical aperture) in the target plane.

absent of all aberrations and misalignments. An analysis on focal properties follows in Sec. 8.8.

It this point in the setup, the target stage, which appears in Fig. 8.2, was constructed and aligned. The procedures used to align the stage are detailed in Appendix 1, and example data collected during alignment are given in Table A.1 and Table A.2, respectively.

8.7 Geometrical Optics Summary and Transmitted Power Analysis

With the optical beamline components installed and aligned, a summary of the geometrical optical calculations is presented to (i) characterize beam properties and (ii) quantify the expected (and observed) low-power signal. The size, location, and constituent material of each optical component were carefully chosen because each element influences focal properties and the final power delivered to the detector. This section illustrates the compounding effect of optical loss, and may guide future system upgrades if needed. Beginning with the FTIR spectrometer's output beam, each major optic that determines focal properties and power transmission will be addressed, as illustrated in Fig 8.4 and Fig. 8.1.

The planar-slab ZnSe window combines the IR and HeNe beams, has a refractive index of $n = 2.4$, and is placed 30° from the incident IR radiation. At 30°, the transmission coefficient through one air/ZnSe interface is $T_{p,1} = 0.870$ and $T_{s,1} = 0.787$ (with polarization denoted). Through the planar slab, two dominant rays are considered: (i) the single-pass ray, and (ii) the ray that transmits through the first surface, reflects from the second, reflects again from the first, and is transmitted through the second. All other transmitted ray intensities are negligible. Thus, the total transmission is $T_p \sim 0.77$ and $T_s \sim 0.65$. The spectrometer's output is approximately unpolarized (when averaged over the full range), so the average window throughput is $T_{\mathrm{ZnSe}} \sim 0.71$.

The beam then encounters the 2" OAP mirror, which focuses light to the intermediate pinhole. Since the beam's diameter is presently 0.5", all power is collected by the mirror. The moderate beam divergence leads to an intermediate infrared focal size of $\sim$ 1.2 mm. Using the 400-μm-diameter pinhole as the optical object, the fraction of transmitted radiation is proportional to area, so $T_{pinhole} \sim (0.4 \text{ mm}/2)^2/(1.2 \text{ mm}/2)^2 \sim 0.11$. The polarizer will then extinguish approximately half of the unpolarized incident radiation, so $T_{polarizer} \sim 0.5$.

The beam diameter at the ZnSe lens (D_l) is easily calculated through a proportionality relating the lens' distance from the object pinhole ($p = 8$"), the beam diameter at the OAP mirror ($D_m = 0.5$"), and the OAP mirror's distance from the pinhole ($p_m = 6$"): $D_l/p = D_m/p_m$. Therefore, $D_l = 0.667$", which is below the lens' 2" diameter. But reflectivity loss at the ZnSe lens occurs, as it did at the window; at normal incidence, single-interface transmission is $T_p = T_s = 0.83$. Lens focusing strongly refracts IR radiation, so only single-pass rays are collected and considered: lens transmission is therefore $T_{lens} \sim 0.69$.

Radiation then propagates toward the target; the next step will analyze the fraction of radiation collected by the detector's elliptical focusing mirror. Following the same proportionality argument given above, the beam diameter at the elliptical mirror (D_e) is calculated relating the mirror's distance from the target ($p_e = 6$"), the beam diameter at the ZnSe lens ($D_l = 0.667$"), and the lens' distance from the target ($q = 2.66$"): $D_e/p_e = D_l/q$. Therefore,

$D_e = 1.5"$, which is also smaller than the mirror's 2" diameter. The fraction of radiation intercepted by the elliptical mirror is thus $T_e = 1$. This fraction will be reduced if the collimated beam diameter is expanded to $\geq 0.67"$.

Here, it is important to note that (using D_l and q) the convergent half-angle $\theta = 7^\circ$, as depicted in Fig. 8.4, and the corresponding numerical aperture of the focusing lens is $NA \leq 0.13$ (which is only 22 percent of that delivered by the microscope). This small angular spread of the focused external beam is beneficial to experiments that require low convergence for the resolution of sharp, resonant features. Again, the collimated beam diameter can be increased or decreased at aperture 2 to modify beam convergence/power throughput as needed.

Concluding the power calculation, the final fraction of power delivered to the detector through the system is thus a product of each transmission coefficient: $T_{total} = T_{\mathrm{ZnSe}} * T_{pinhole} * T_{polarizer} * T_{lens} * T_e$, or $T_{total} \sim 0.03$. Therefore, only 3 percent of initial radiation is delivered to the target. Indeed, experiments show that the external beam signal is much weaker than that provided by the IR microscope, but the experimental flexibility of the external IR beamline compensates for this power limitation, and meaningful spectra are nevertheless collected with the external beam system. In the next section, the polarization and focal properties of the beamline are experimentally characterized.

8.8 Polarization and Focal Characterization

To begin characterization of the external FTIR spectrometer beamline, a polarization efficiency analysis was performed. The tests utilize two wire-grid polarizers, denoted “polarizer” before the sample, and “analyzer” after the sample. Vertical electric field alignment (with respect to the optical table) corresponds to s polarization at the target, and horizontal field to p polarization. Such tests analyze (i) the efficiency of the polarizers and (ii) the degree of polarization conversion by the focusing optic; the latter is likely small when using a low-convergence lens but may be larger for Cassegrain reflecting optics. Two spectra were collected: s-polarized and p-analyzed radiation, and s-polarized and s-analyzed radiation. The former was normalized to the latter, resulting in the extinction ratio presented in Fig. 8.5: the ratio is approximately 0.25 percent. A line is included to provide a visual guide because the low signal-to-noise ratio produces an unstable, noisy spectrum. This ratio leads to a polarization efficiency of ~ 400, which is nearly optimal.

As a first step in characterizing the system’s focal properties, mounted pinholes with various diameters were placed in the IR beam’s focus to quantify power transmission. Absolute transmission through each pinhole was normalized to open transmission, resulting in a ratio from 0 (no transmission) to 1 (complete transmission). Pinhole diameter was converted into area (μm^2) and then plotted against total transmitted power (Fig. 8.6). The data are connected by a shape-preserving piecewise cubic Hermite interpolant that was calculated using MATLAB.

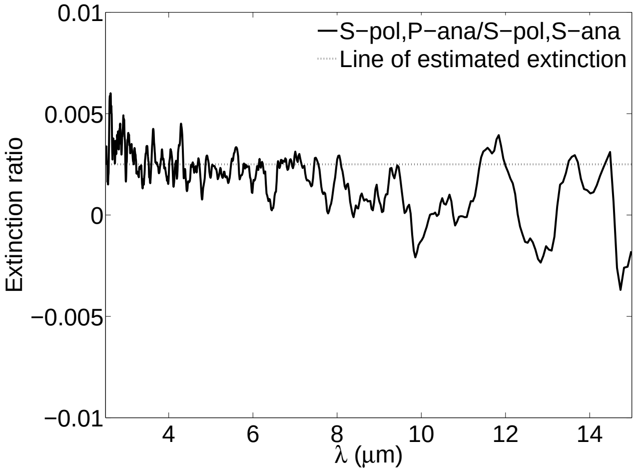

Figure 8.5: The extinction ratio of s-polarized radiation is plotted versus wavelength. The dotted line provides a visual guide, since efficient extinction results in a low signal-to-noise ratio. Extinction is calculated as radiation transmitted through an s polarizer/p analyzer pair, normalized to an s polarizer/s analyzer pair. The extinction ratio is ~ 0.25 percent, which gives an efficiency of ~ 400.

Lasers have Gaussian profiles and are considered focused with beam waist w when their intensity drops by $1/e^2$ from the central axis. Therefore, a Gaussian beam is focused to diameter w when $1 - 1/e^2$ or ~ 87 percent of incident radiation is transmitted through a hard aperture with the same diameter. Deviation from a pure Gaussian profile, as is the case with an incoherent IR beam, will result in reduced focusing ability. Lens dispersion and alignment imperfections further degrade focusing, so a focal waist of $i > 133$ μm is expected. As shown in Fig. 8.6, the external FTIR spectrometer setup yields a focal beam diameter of $i = D_f = 200$ μm (indicated by the black line), using the strict Gaussian condition of 87-percent transmission. Therefore, it

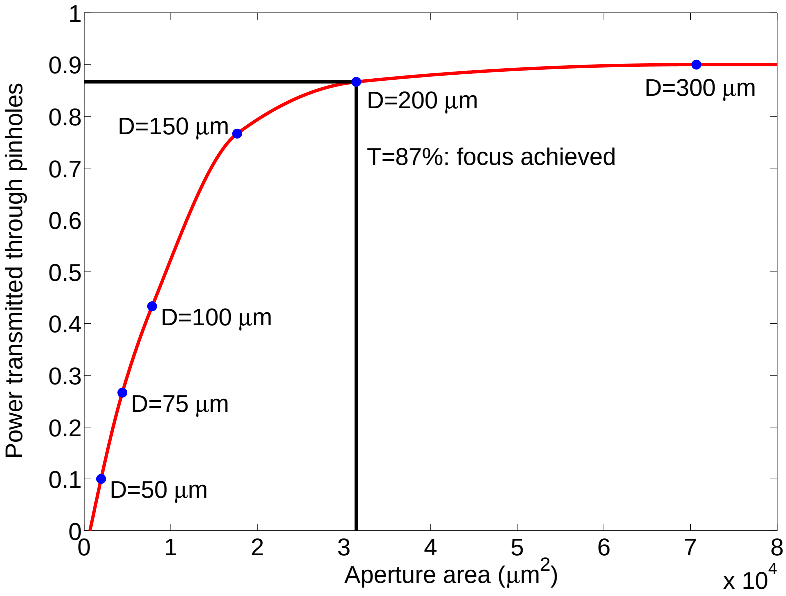

Figure 8.6: Normalized total IR power transmitted through mounted pinholes of various diameter. Gaussian focusing of a beam with waist w is achieved when $1-1/e^2 \sim 87$ percent is transmitted through a hard aperture of diameter $D_f{=}w$ in the focal plane.

is concluded that the optical setup focuses *total* IR radiation output to a spot of $D_f \leq 200$ μm; this total spectrum spans 1.4 μm–16.7 μm, but has a central power wavelength of 3.13 μm. With the pinhole transmitting maximal IR, the HeNe laser is slightly adjusted at M_3 to ensure ideal alignment with the IR beam at focus. This type of focal diameter analysis is better suited to chromatic-aberration-free sources (e.g., monochromatic lasers): indeed, initial spectroscopic tests indicated discrepancies between the external beamline and the IR microscope spectra. Therefore, advanced experiments were performed to diagnose chromatic aberration and the resulting effect on spot size.

Section 7.3.2 reported that the power spectrum's central wavelength is $\lambda = 3.13$ μm; thus, when the pinhole's transmitted power is collected (and integrated) by the detector, the focal position will correspond to the entire spectrum, the majority of which resides in the near-IR. It was determined that chromatic aberration, while moderate, prevented ideal focusing in other IR ranges (e.g., mid-IR range). To characterize this aberration, pinholes were placed in optimal IR beam focus and were then scanned in the focal direction, Z_{out}. The results found using the 150-μm and 200-μm pinholes are given in Fig. 8.7 (a) and (b), respectively. Spectral results obtained using the 300-μm and 500-μm pinholes are given in Fig. 8.8 (a) and (b), respectively. Through these advanced pinhole experiments, it is confirmed and concluded that radiation is indeed confined to a 200-μm diameter (for a finite wavelength range).

Note that target pinholes of diameter 100 μm or smaller were not included in beam-characterization experiments: as evident in Fig. 8.6, less than 50 percent of incident radiation is transmitted through such apertures, which would induce considerable error when performing the numerical renormalization of Sec. 8.10. Furthermore, metamaterials are typically fabricated with dimensions larger than 100 μm, rendering such data unnecessary. But in the event that data on the confinement of radiation to 100 μm or less is needed, experiments can be performed.

Also note that the intermediate-focus pinhole diameter selected was 400 μm. Additional experiments (available to the laboratory) exhaustively analyzed all combinations of the four primary pinholes listed above (i) for use

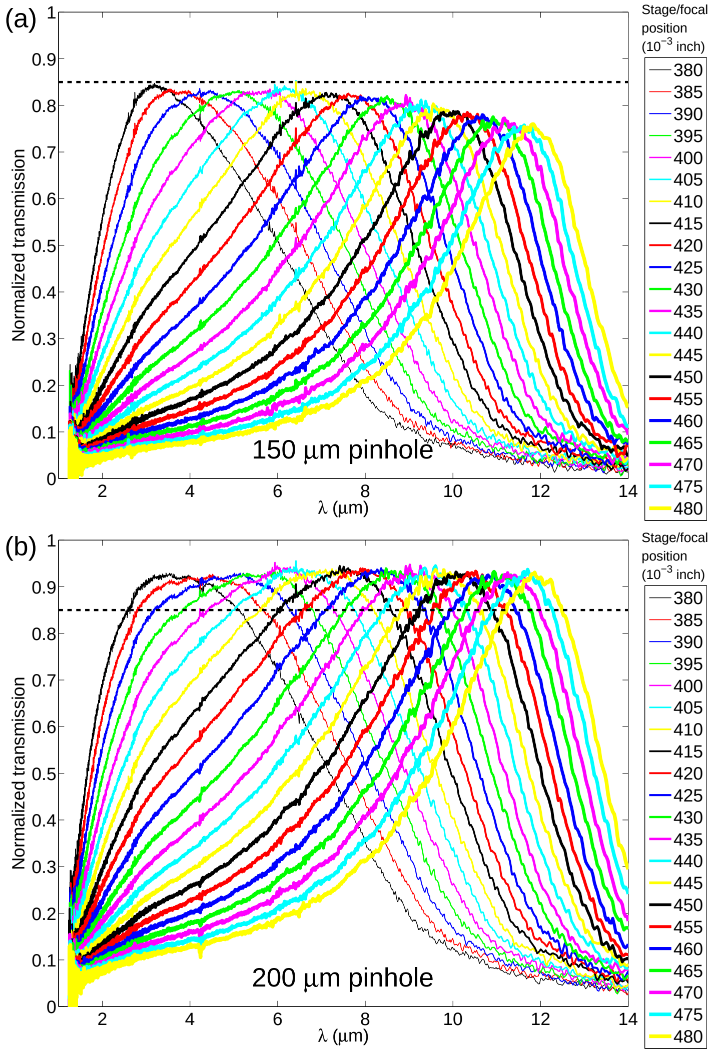

Figure 8.7: Infrared chromatic aberration (wavelength dispersion) is mapped out using pinholes of diameter (a) 150 μm and (b) 200 μm by scanning in the focal direction, z. Intensities above the dashed lines indicate well-confined wavelengths for the corresponding focal positions. Radiation is indeed confined to a 200-μm spot in (b) for a range of λ. Metamaterial spectra can be renormalized using these data sets, giving results equivalent to a 100-percent beam/sample interaction.

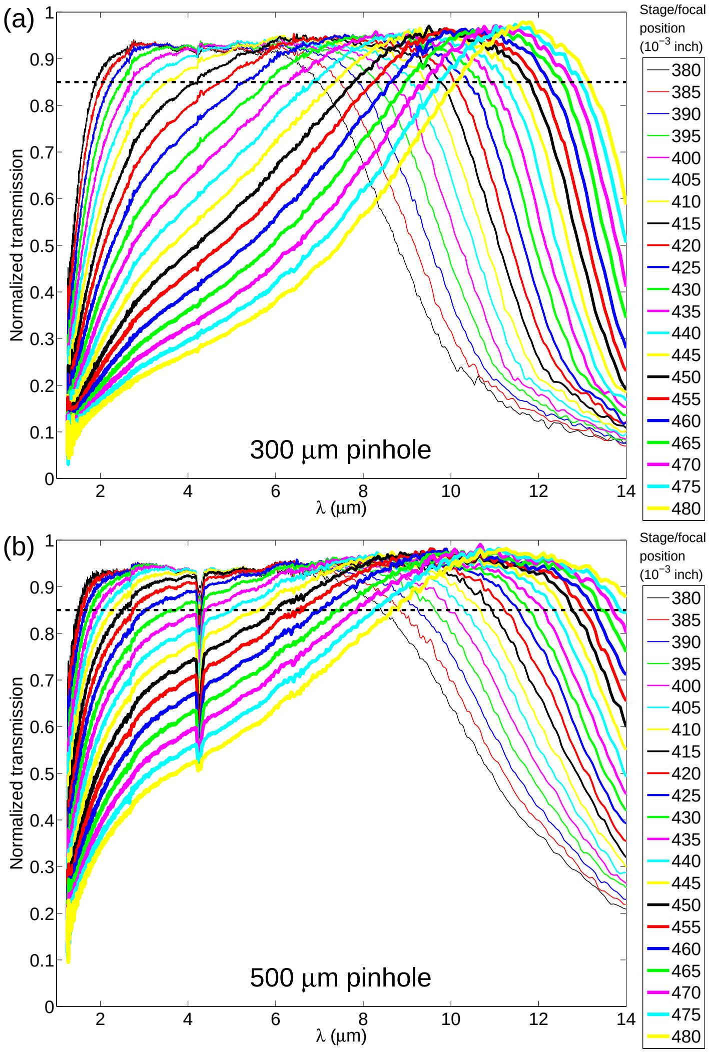

Figure 8.8: Infrared chromatic aberration (wavelength dispersion) is mapped out using pinholes of diameter (a) 300 μm and (b) 500 μm by scanning in the focal direction, z. Intensities above the dashed lines indicate well-confined wavelengths for the corresponding focal positions.

in the intermediate focus as the optical object, and (ii) for use in the target plane for image diagnostics. Take, for example, a case where the 200-μm and 300-μm pinholes were used as optical objects. To quantify the system's focusing ability, a 150-μm-diameter pinhole was scanned in the target plane for both objects. When using the 300-μm object pinhole, radiation was confined to 150 μm (using the Gaussian focusing condition of $T \sim 87$ percent) for a range of $\Delta\lambda = 0.95$ μm. When using the 200-μm object pinhole, radiation was confined to 150 μm for a range of $\Delta\lambda = 2.15$ μm. Confinement was thus improved by $\sim 2.2\times$. Correspondingly, a reduction of pinhole area from 7.06×10^4 μm to 3.14×10^4 μm results in an image-area reduction by $2.25\times$, in good agreement with experimental observation. Finally, it must be noted that the 400-μm object pinhole, while slightly reducing radiation confinement, dramatically increases power throughput. Indeed, object pinholes smaller than 400 μm (e.g., 150 μm–300 μm) can be used to reduce focal diameter, but power throughput and signal stability will be degraded (an effect that can be partially rectified by a time-consuming increase in scans).

8.9 Analysis of Chromatic Aberration

The refractive index of ZnSe, which is presented in Table 8.1, slightly decreases with wavelength, from $n(3.75\ \mu\text{m}) = 2.434$ to $n(12\ \mu\text{m}) = 2.393$. These wavelengths correspond to maximal transmission at $Z_{out,1} = 0.380"$ and $Z_{out,2} = 0.480"$ in Fig. 8.7 (b), respectively. The experimental focal displacement/chromatic aberration for this configuration is therefore $\Delta Z_{out}^{exp} = 0.100"$.

$\lambda(\mu\text{m})$	n_{ZnSe}	$\lambda(\mu\text{m})$	n_{ZnSe}
0.54	2.6754	7.40	2.4201
0.58	2.6312	7.80	2.4183
0.62	2.5994	8.20	2.4163
0.66	2.5755	8.60	2.4143
0.70	2.5568	9.00	2.4122
0.74	2.5418	9.40	2.4100
0.78	2.5295	9.80	2.4077
0.82	2.5193	10.20	2.4053
0.86	2.5107	10.60	2.4028
0.90	2.5034	11.00	2.4001
0.94	2.4971	11.40	2.3974
0.98	2.4916	11.80	2.3945
1.00	2.4892	12.20	2.3915
1.40	2.4609	12.60	2.3883
1.80	2.4496	13.00	2.3850
2.20	2.4437	13.40	2.3816
2.60	2.4401	13.80	2.3781
3.00	2.4376	14.20	2.3744
3.40	2.4356	14.60	2.3705
3.80	2.4339	15.00	2.3665
4.20	2.4324	15.40	2.3623
4.60	2.4309	15.80	2.3579
5.00	2.4295	16.20	2.3534
5.40	2.4281	16.60	2.3487
5.80	2.4266	17.00	2.3438
6.20	2.4251	17.40	2.3387
6.60	2.4235	17.80	2.3333
7.00	2.4218	18.20	2.3278

Table 8.1: Wavelength-dependent index of refraction for CVD-grown ZnSe at room temperature (20°C). Data courtesy of ISP Optics.

To estimate if such displacement is expected, dispersion can be calculated. To begin, the thin lens approximation can be applied to the lensmaker's equation [11]:

$$\frac{1}{f} \approx (n-1)\left[\frac{1}{R_1} - \frac{1}{R_2}\right], \tag{8.5}$$

where R_1 and R_2 represent radii of curvature for the first and second spherical surfaces. For simplicity, two approximations are assumed: (i) the aspherical surfaces can be represented by spheres, and (ii) the lens thickness d is much smaller than the radii. For the stated focal length of $f_1 = 2"$, optimal IR focus occurs at image distance $q_1 = 2.66"$, $\lambda_1 = 3.75\ \mu$m, and $Z_{out,1} = 0.380"$ (optimal focusing of the FTIR beamline was defined by a maximal transmission of total IR radiation power). The relative IR beam displacement in z is sought, so R_1 and R_2 are held constant while varying index from $n(\lambda_1)$ to $n(\lambda_2)$ in Eq. 8.9. The resulting focal length $f_2(\lambda_2 = 12\ \mu\text{m}) = 2.059"$. Returning to the thin lens formula of Eq. 8.6, and maintaining a fixed object distance p, the new image/focal distance is found to be $q_2 = 2.772"$. Thus, total estimated theoretical displacement is $\Delta q = \Delta Z_{out}^{th} = 0.112"$, in good agreement with the experimentally observed $\Delta Z_{out}^{exp} = 0.100"$; the discrepancy between experiment and theory is only 0.012", or about 300 μm.

8.10 Numerical Renormalization for Small-Area Spectroscopy

With dispersion understood and characterized, beam interactions with small metamaterial samples can be considered. While IR radiation is well-confined to 500-μm diameters for large wavelength ranges ($\Delta\lambda \sim 8$ μm, visible in Fig. 8.8 (b)), reflection from and transmission through samples smaller than 500 μm will contain information about the surrounding substrate, at least for some part of the IR spectrum. But a renormalization procedure can be performed to correct this problem: for a fixed light polarization, spectra collected from the sample, the surrounding smooth substrate, and a background reference (mirror for reflection, open space for transmission) can be used to calculate the 100-percent beam/sample interaction. It is, of course, ideal to fabricate samples large enough to be accommodated within the beam and within the wavelength range of interest, thus circumventing additional mathematics and experimental error, but cost, time, and nanoscale resolution often preclude large sample creation.

For a metamaterial sample with array size d, the spectrum that results from mixing between the sample and the substrate is described by

$$S^{mix} = S_m^{pure}(r_d) + S_s^{pure}(1 - r_d), \tag{8.6}$$

where S^{mix} is the spectrum collected from the optical system, r_d is the λ-dependent ratio of radiation contained within a region of diameter d (into the path of which the sample is placed), and S_s^{pure} is the substrate spectrum resulting from a 100-percent beam interaction (simple to collect because substrates are large). The term S_m^{pure} is the metamaterial spectrum that results from a 100-percent sample/beam interaction; this is numerically calculated.

As a demonstration of this renormalization procedure, a (150 μm)^2

metamaterial array of Au "Π" structures was analyzed in the external FTIR spectrometer beam's reflection mode. The sample is composed of unit cells that resemble the Greek letter Π, as evident in the SEM image of the Fig. 8.9 (b) inset. External beam spectra from the Π sample are given in Fig. 8.9 (a) for multiple focal positions, and are compared to an IR microscope spectrum that exhibits a true 100-percent beam/sample interaction. In both cases, $\theta = 25°$, and light is s-polarized and aligned along the vertical (y) direction of the Π structure. Clearly, initial agreement in Fig. 8.9 (a) is poor, but with the renormalization of Eq. 8.10 (which takes into account CaF_2 substrate reflectivity), the spectra converge, as shown in Fig. 8.9 (b). The beamline's peak reflectivity of 80 percent is supported by theory; the suppressed maximum revealed by the microscope is likely caused by its larger numerical aperture, which leads to wavevector averaging. Therefore, with numerical calculations, the beamline has been shown to spectrally analyze samples as small as 150 μm.

In general, Z_{out} should be set to match the expected spectral position of the metamaterial resonance, because focused intensity decreases for wavelengths far from the ideal Z_{out} position, inducing increased signal noise. Finally, additional renormalization (not shown) can be performed that accounts for (i) significantly oblique incidence (e.g., $\theta = 60°$) and (ii) sample sizes not matched to pinhole diameters used in laboratory analysis (150 μm, 200 μm, 300 μm, and 500 μm) by introducing additional geometric factors into Equation 8.10.

Of course, samples that possess dimensions larger than the FTIR beam

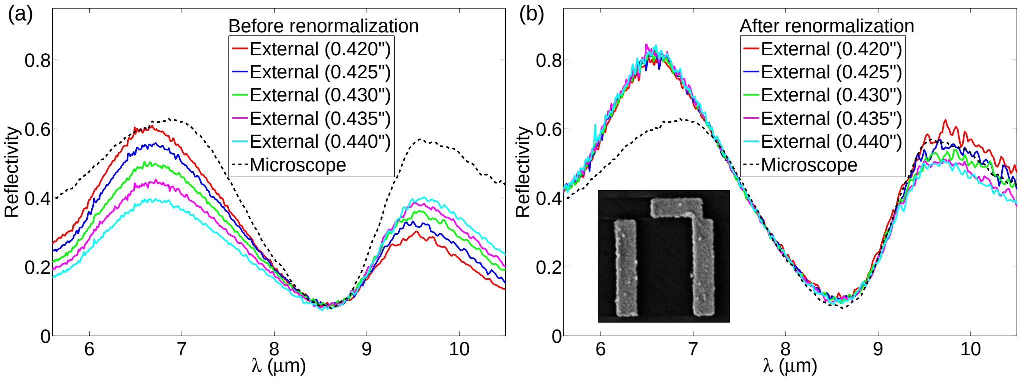

Figure 8.9: Reflection spectra from the (150 μm)^2 periodic array of Au "Π" structures (depicted in SEM inset). Radiation is s-polarized, the electric field is aligned along the vertical direction of the Π structure, and $\theta = 25°$. (a) External FTIR spectra are compared to that from the IR microscope; reflection from CaF_2 (not shown), which is used for renormalization, is flat and $\sim$ 4 percent. Dispersion is evident in (a), as the beam's interaction with the sample depends on focal position. (b) After renormalization, all external spectra show agreement. At $\lambda = 6.5$ μm, external beam reflectivity reaches 80 percent, in agreement with theory.

are ideal and do not require renormalization, and can be analyzed at large incident angles without concerns of substrate interaction. For example, a large-area structure is explored that was predicted to show wide-angle infrared absorption. The sample was fabricated with the assistance of Nanohmics (Austin, TX), theoretically modeled by Chihhui Wu, and experimentally analyzed by the author. The sample, which will be discussed in detail in Ch. 9, consists of a Si substrate, a smooth layers of Au and dielectric films, and a 1D periodic Au grating that was structured via step and flash imprint lithography. When the Au strips are aligned perpendicular to the electric field vector, the structure exhibits angle-*independent* near-perfect IR absorption for a specific wavelength that depends on the design. Previous absorber samples were successfully analyzed with fixed-incidence FTIR microscopy, but the wide-angle characteristics can only be explored with a beamline that allows for variable-angle incidence.

8.11 Verification of Angle-Dependent IR Spectroscopy of Small-Area Metamaterials

As a final verification of the external beamline's spectroscopic capabilities, a metamaterial with strongly angle-*dependent* features was fabricated and analyzed. The sample's unit cell (left panel of Fig. 8.10) consists of Au antenna pairs that are each 1800-nm long, 300-nm wide, 75-nm thick, and have a center-to-center antenna spacing of 800 nm. The unit cells are arrayed with 2.25-μm pitch in the x and y directions, and reside on a CaF_2 substrate ($n \sim 1.4$). The sample is given in the right panel of Fig. 8.10. Fabrication employed electron beam lithography (EBL) to write the antenna structures in polymer resist. After chemical development, a 75-nm Au film was thermally evaporated, and the surrounding resist was chemically stripped via lift-off, leaving the antennas arrayed on the substrate with an area of $(300\ \mu\text{m})^2$.

Transmission spectra were collected with the external beamline under s and p polarizations for incident angles from 0° to 50° in steps of 5°, as (selectively) presented in Fig. 8.11, with corresponding theory. For visual clarity, line spectra are vertically displaced 5 percent with increasing angle. The dots for p polarization are visual cues to show the spectral positions of the $(0,-1)$ Wood's anomalies (periodicity-based diffraction resonances), which

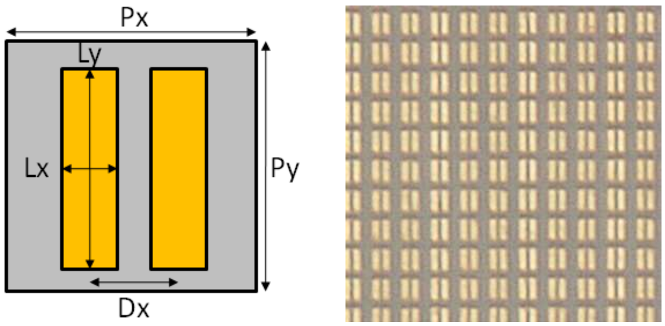

Figure 8.10: (Left panel) Schematic of the Au antenna pair unit cell. The antennas are 75-nm thick, and possess the following dimensions: length $L_y =$ 1800 nm, width $L_x = 300$ nm, the center-to-center spacing $D_x = 800$ nm, and x and y pitch $P_x = P_y = 2.25$ μm. (Right panel) Optical micrograph of the metamaterial array.

correspond to transmission maxima before the dipolar electric SPP resonance and minima after the resonance. The dots for s polarization show the positions of the (-1,0) Wood's anomalies (WAs): the WAs are clearly suppressed in the spectra, which results from having two antennas in the unit cell separated in the x direction by a spacing close to half the periodicity. Therefore, the diffraction order along the x direction is almost completely suppressed.

In Fig. 8.11, all major angle-dependent resonances are resolved; discrepancies between theory and experiment are attributed to (i) experimental antenna dimension variations, (ii) the non-plane-wave profile of incident IR radiation, (iii) the modeling of 2D (not 3D) structures, and (iv) the calculation's solution, which is obtained from the semianalytic method that accounts for only the first few fundamental current modes of the antennas [23]. The model can be improved if increasingly higher-order current modes are considered.

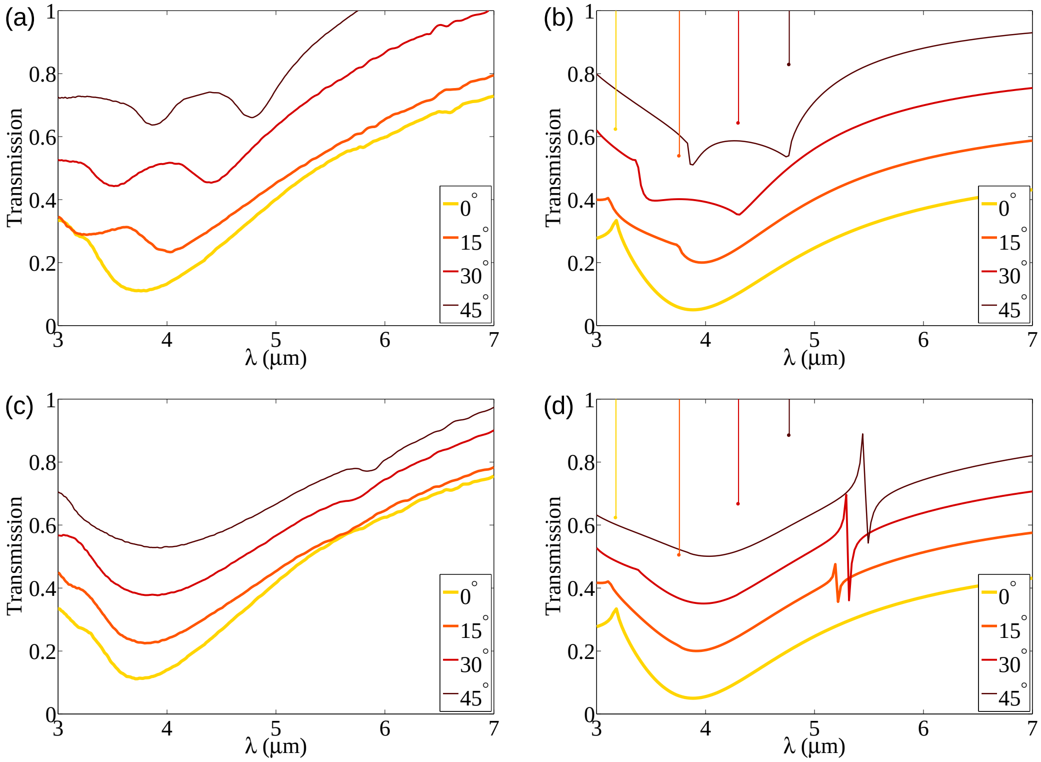

Figure 8.11: (Left panel) Experimental and (right panel) theoretical antenna pair transmission plots for (a,b) p and (c,d) s polarizations. Spectra are offset 5 percent in T with increasing angle for clarity. The p-polarized dots indicate the position of the (0,−1) Wood's anomaly and correspond to maxima before the dipolar electric SPP resonance and to minima after the resonance. The s-polarized (−1,0) Wood's anomalies are suppressed and do not manifest in spectra.

The s-polarized magnetic dipole resonance at $\lambda \sim 5.5$ μm is less resolved by experiments than by theory; after a thorough experimental investigation that reduced angular beam spread and incrreased spectral resolution, it was found that these two factors do not account for the discrepancy. Furthermore, these factors were accounted for in analytical theory, but the discrepancy

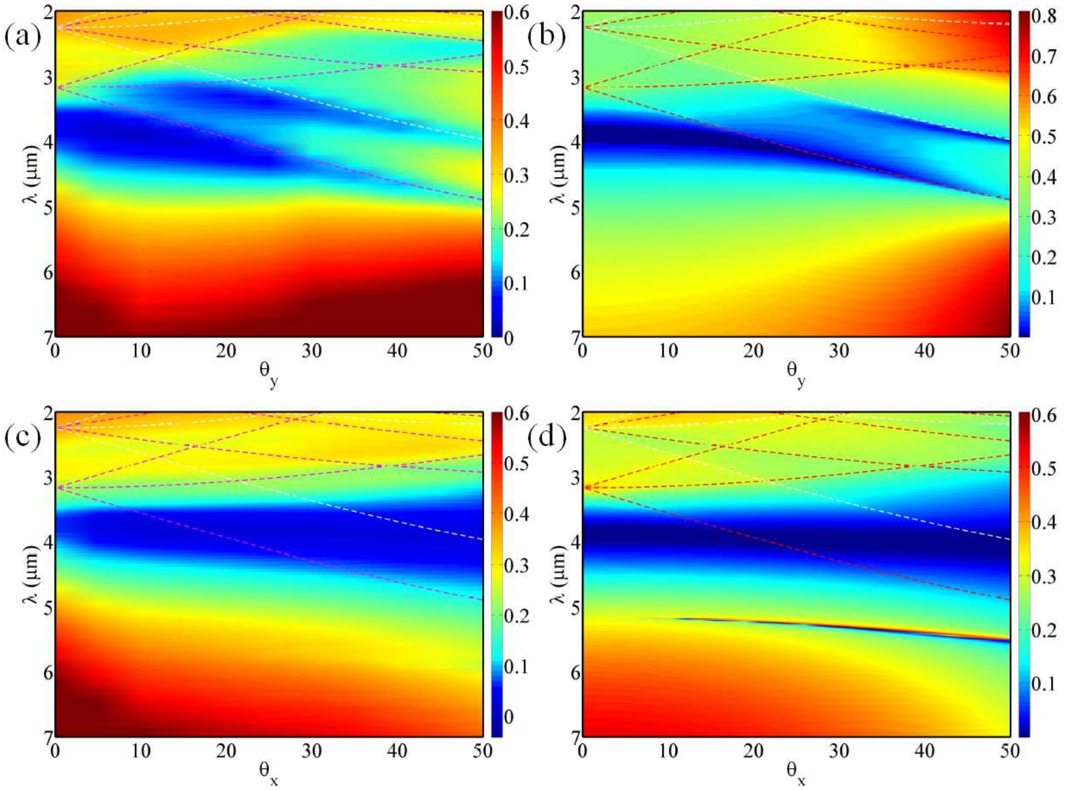

Figure 8.12: (Left panel) Experimental and (right panel) theoretical transmission spectra for (a,b) *p*-polarized and (c,d) *s*-polarized radiation. The electric field is aligned along the antennas for both polarizations. Experimental plots are interpolated from line spectra collected from 0° to 50° in steps of 5°. Theoretical mode dispersion is represented by dotted lines, as described in the text.

remained. Therefore, it was concluded that size and quality variations among the fabricated antenna pairs—and not the experimental infrared beamline—cause the weak experimental resonance.

The 2D color plots of Fig. 8.12 show zero-order transmission spectra for the Au antenna pair array. The right panel (a,c) gives experimental results, with corresponding theory in the left panel (b,d). Radiation is *p*-polarized in (a,b) and *s*-polarized in (c,d); in both cases, electric field is aligned along the antenna. White dotted lines correspond to air-side Wood's anomalies (periodicity-based diffraction resonances), and the red dotted lines to CaF_2-side WAs. The numerical calculation method is based on work by Dawes et al. [23], which describes a semianalytical method to solve for the optical response of periodic structures. As evident in Fig. 8.12, experiment and theory are in excellent agreement.

As shown in Fig. 8.12 (d), *s*-polarized radiation excites a collective electric-dipolar resonance that follows the (0,±1) diffraction order/WA (middle, red dashed line originating from $\lambda = 3.1$ μm) and a collective magnetic-dipolar resonance (sharp feature at $\lambda = 5.1$ μm) that tracks along side the (-1,0) diffraction order/WA (negative-sloped red dashed line originating from $\lambda = 3.1$ μm). The magnetic mode cannot be excited by *s*-polarized radiation when $\theta = 0°$ nor by *p*-polarized radiation for any angle (indeed missing in Fig. 8.12 (a,b)) because these cases lack the surface-normal magnetic field required to excite the mode. The *s*-polarized magnetic resonance at $\lambda = 5.9$ μm is visible in Fig. 8.11 (c), but subtle in Fig. 8.12 (c), as discussed above.

The *s*- and *p*-polarized Wood's anomaly intensities differ because the two polarizations experience different degrees of destructive interference of radiated antenna waves. The *s*-polarized WAs are suppressed by this destructive interference, and calculations verify that the asymmetric cladding (air/CaF_2) further suppresses WAs, when compared to symmetric cladding. A detailed experimental and theoretical study of this antenna pair structure is ongoing, but it is presently verified with the Au antenna sample that the external FTIR spectrometer beamline correctly resolves strongly angle-dependent resonances of small-scale metamaterial arrays.

8.12 Conclusions

In conclusion, the external beamline based on the FTIR spectrometer was designed, built, characterized, and demonstrated to achieve a 200-μm spot size, serving as the major experimental objective of this dissertation work. Modest chromatic aberration in the ZnSe lens limits ideal focusing to a select spectral range, but the effect was characterized and theoretically verified. While all aberrations are undesirable, a numerical renormalization procedure was developed that compensates for chromatic aberration, and even enables the spectroscopy of samples smaller than the beam diameter. Renormalization was used to successfully analyze a sample that is strictly smaller than the beam yet was spectrally verified by IR microscopy—a 150-μm metamaterial array of Au "Π" structures. A small-area array of Au antenna pairs was then used to verify the system's ability to analyze angle-dependent metamaterial resonances.

The external beamline solves the major problems encountered with the IR microscope. Most importantly, a target rotation stage and a movable detector now permit angle-resolved reflection and transmission studies, and the focusing optics permit better polarization and divergence control. Light control is demonstrated with, for example, the array of Au "Π" structures, the Au antenna pair metamaterial, and the wide-angle perfect IR absorber of Ch. 9 that requires polarization control and large angle variations to verify its broad-angle absorptivity characteristics. The external beamline apparatus will continue to provide a robust platform for the analysis of IR metamaterials.

Chapter 9

Wide-Angle, Frequency-Tunable, Perfect Infrared Absorbing Metamaterials

9.1 Introduction

Electromagnetic metamaterials have been rapidly developing in recent years, promising to deliver new composite media with exotic properties generally unattainable in nature [110, 96, 79, 92]. These metamaterials are not interesting solely as a fundamental science: the ability to engineer electric and magnetic responses enables many possible applications, such as perfect lenses [79], cloaking devices [92], subwavelength transmission lines and resonators [4], and agile antennas [19]. Metamaterials also show great promise as efficient subwavelength absorbers [117, 5, 26, 39, 65] in which EM fields are confined within a subwavelength region, demonstrating how light can be manipulated with engineered structures.

The subwavelength absorber finds various technological applications. Such devices include miniature sensors such as photodetectors and microbolometers, which would exhibit enhanced sensitivity through the absorber's native strong field confinement. According to Kirchhoff's law, an efficient absorber is also an efficient thermal emitter; tunable emission sources would be possible with perfect absorbing structures. This is important for thermophotovoltaics (TPVs), where an efficient narrow-band thermal emitter is desired: by matching the emission spectrum of the thermal emitter to the bandgap of the TPV converter, one can dramatically improve the efficiency of current generation [21] without the additional complication [61] of placing the TPV cell in the near field of the emitter. In photovoltaic (PV) applications [107], the efficiency of solar cells can be enhanced by strong field enhancement inside the absorbing metamaterial.

High absorptivity in the near-IR has been demonstrated, but devices have been limited in scale (on the order of $(100\ \mu\text{m})^2$), and wide-incidence-angle absorption has been proposed [117, 5, 26, 39, 65] but not experimentally verified. A simple, ultra-thin infrared absorber that exhibits wide-angle functionality is presented. The FTIR microscope (Ch. 7) was used to demonstrate the spectral tunability of In_2O_3-based absorbers and is presented in Sec. 9.3.2, while the angular dependence of SiO_2-based samples was verified using the novel FTIR beamline (Ch. 8) and is presented in Sec. 9.3.3. The samples presented are the first known to be prepared with step and flash imprint lithography, which is low-cost and works for large areas (up to $(2.5\text{ mm})^2$) compared with electron beam lithography. Furthermore, samples comprised of both (i) gold (Au) and silicon dioxide (SiO_2) and (ii) Au and indium oxide (In_2O_3) are demonstrated, showing the flexibility of dielectric choice. This metamaterial absorber encompasses all the advantages mentioned above: an extremely high absorption rate that approaches 100 percent, a wide range of incident angle operation, tunability of the absorbing frequency, subwavelength size, and large field enhancement inside the metamaterial.

In this work, nanoscale sample fabrication was performed by Andrew Milder et al. of Nanohmics (Austin, TX), and theoretical design and modeling were performed by Chihhui Wu. The author performed spectroscopic analysis using both FTIR micro-spectroscopy and the external IR beamline, and coordinated research activities between institutions.

9.2 Theoretical Description of the Absorbing Structure

The geometry of the proposed structure and the corresponding parameters are illustrated in Fig. 9.1 (a). An SEM image of a SiO_2-based absorber is shown in Fig. 9.1 (b). The structure is uniform in the y direction, and repeating in the x-direction with periodicity L. Each unit cell consists of an infinitely long metallic strip with 20-nm thickness, width W, and gap $D \equiv L - W$ on top of a 17-nm layer of dielectric (SiO_2 or In_2O_3). The structure is backed by a thick, 100-nm metallic wall that blocks transmitted radiation. Thus, the absorptivity of the structure is determined by its reflectivity: $A \equiv 1 - |r|^2$, where r is the reflection coefficient. The metal is Au and has dielectric permittivity given by the Drude model:

$$\epsilon_{\mathrm{Au}}(\omega) = 1 - \frac{\omega_p^2}{\omega(\omega + i\gamma)}, \tag{9.1}$$

where the effective plasma frequency is $\omega_p = 1.32 \times 10^{16}\ \mathrm{s}^{-1}$, and the collision frequency $\gamma = 1.2 \times 10^{14}\ \mathrm{s}^{-1}$ [27]. Depending on the application of the absorber,

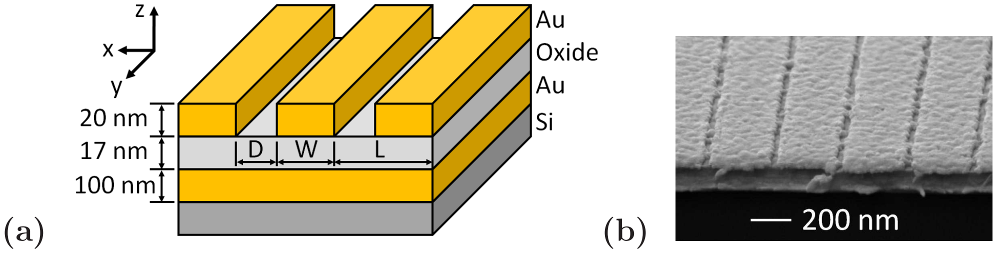

Figure 9.1: (a) Schematic of the perfect IR absorbing metamaterial. This 2D structure is continuous in y and periodic in x. The oxide layer represents SiO_2 or In_2O_3, depending on the sample. (b) An SEM image of the SiO_2-based absorbing structure with $L = 300$ nm and $W = 260$ nm.

different materials can be used. For example, high-melting-temperature metals (such as tungsten) can be used for TPV applications. For sunlight harvesting or infrared imaging, the dielectric would be replaced with a semiconductor whose bandgap matched the absorption wavelength.

Perfect absorption is attributed to critical coupling in a two-channel system. The transmission or forward scattering is prohibited by the thick mirror; therefore, the only two channels into which energy can flow are backscattering and absorption. When the leaky mode hosted by the structure has the same scattering and resistive cross sections, an incoming field can couple through the scattering channel, excite the mode, and then decay into the absorptive channel without reflection back through the scattering channel. The result is near-perfect absorption, and because these processes are geometry-dependent, the effect is frequency-tunable.

9.3 Fabrication and Spectroscopy of Wide-Angle Perfect IR Absorbers

9.3.1 Step and Flash Imprint Lithography Fabrication

Samples were prepared by step and flash imprint lithography (S-FIL, Molecular Imprints) [52]. Imprint lithography delivers feature resolutions (< 50 nm) competitive with electron beam lithography (EBL) but in a cost-effective, parallel process. The EBL process requires slow and costly serial beam scanning to define every feature, typically resulting in sample arrays on the order of $(10\ \mu\text{m})^2$ to $(100\ \mu\text{m})^2$. The S-FIL imprint mask, however, is made once made via EBL but is then reused a near-limitless number of times to create features in parallel on large scales, with arrays up to $(25\ \text{mm})^2$.

First, a Cr-Au-Cr multilayer (3 nm–94 nm–3 nm) was deposited on a Si substrate by electron beam evaporation; Cr is used as a sticking layer, resulting in an effective 100-nm metal film. For indium-based samples, a 16-nm layer of In_2O_3 followed by a 1-nm SiO_2 layer was then deposited by PECVD as the dielectric spacer. For silicon dioxide-based samples, a 17-nm film of SiO_2 was deposited. Layers of Cr (3 nm) and Au (30 nm) were subsequently deposited on top. To begin S-FIL, a planarizing layer of TranSpin was applied followed by a dispensation of the UV curable liquid, MonoMat. The template required for imprint lithography was constructed of quartz and was formed by an etch process using a mask exposed by EBL to obtain the required strip pattern. After the pattern is imprinted on the MonoMat layer with the quartz mask, the MonoMat residue and TranSpin layers under the imprinted area

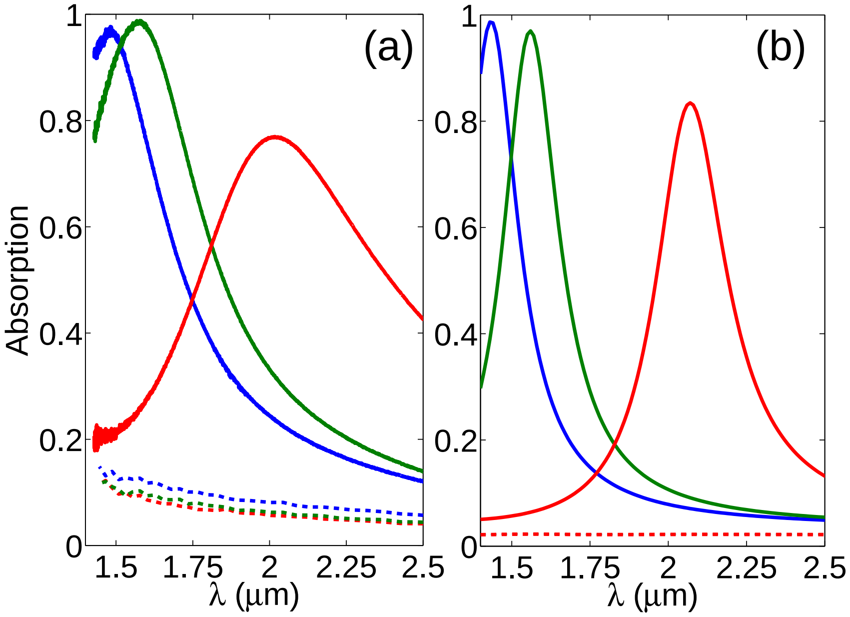

Figure 9.2: Plots of absorption as a function of wavelength (λ) for the In_2O_3-based perfect IR absorbing structure. Incident radiation is p-polarized. (a) Experimental absorption spectra are compared to (b) COMSOL simulations. Blue lines correspond to $[L,W]$ = [300 nm, 230 nm], green lines to [330 nm, 250 nm], and red lines to [450 nm, 350 nm]. Theory courtesy of C. Wu.

are removed by reactive ion etching. The exposed Au is then removed with Ar sputter etching. After finishing the Au pattern, the polymers are removed with O_2 plasma resist strip. An SEM image of the SiO_2-based sample is shown in Fig. 9.1 (b). Each final array size was $(1.2\text{ mm})^2$.

9.3.2 FTIR Micro-Spectroscopy of Absorber Structures

When the incident wave is p-polarized, the wavenumber and the electric field are in the x-z plane, and the magnetic field is aligned in the y direction (along the strips). The sample was also analyzed under s polarization, where the magnetic field is in the y-z plane, and the electric field is aligned in the x direction. In both cases, the electric field is perpendicular to the strips. When the electric field is parallel to the strips, absorption is minimal.

The first set of experiments analyzed the In_2O_3-based samples and rapidly verified that the metamaterial structures were indeed perfectly absorbing. Reflectance (R) spectra were collected with the Thermo Scientific Continuum microscope coupled to the Nicolet 6700 FTIR spectrometer using s- and p-polarized radiation and a 2 cm^{-1} wavenumber resolution in the 7000 cm^{-1}–650 cm^{-1} (1.4 μm–15.4 μm) spectral range. The incidence angle was $\theta = 25°$. A wire-grid polarizer defined electric field polarization. Since thick Au prohibits transmission, absorption is defined as $A = 1 - R$. Figure 9.2 shows A for samples of different dimensions. Finite element method simulations were performed with COMSOL to verify the experimental results. Calculations used the Drude model of Eq. 9.1 for the permittivity of Au, an index of refraction $n_{\mathrm{SiO_2}} = 1.5$ for silicon dioxide, and an index $n_{\mathrm{In_2O_3}} = 1.8$ for indium oxide, where $n = \sqrt{\epsilon}$. It was noticed from SEM images that metal residue between the strips was left from the etching process. To account for this residue in calculations, an extra 2-nm layer of Au was added on top of the spacer, between the strips. It was found that the extra layer of thin Au blueshifts the absorption peak.

It is clear from Fig. 9.2 that the In_2O_3-based structures are efficient absorbers, can be optimized to reach nearly $A \sim 100$ percent, and can be accurately modeled with simulation software. As absorption properties depend on dimensions, it can be seen that the variants $[L, W] = [300\text{ nm}, 230\text{ nm}]$ (blue lines) and $[L, W] = [330\text{ nm}, 250\text{ nm}]$ (green lines) are nearly ideal absorbers, while the sample with $[L, W] = [450\text{ nm}, 350\text{ nm}]$ (red lines) is farther from the ideal parameters. In all cases, inhomogeneous broadening of the experimental spectra compared to theoretical predictions most likely results from the absorber's structural imperfections. However, as demonstrated, resonances are robust against imperfections, and therefore the peak absorptivity remains large. Further details of perfect absorber device design will be presented elsewhere [118].

9.3.3 Wide-Angle Absorption Spectroscopy

An effective absorber is one that maintains a large absorption rate over a wide range of incident angles. The proposed metamaterial absorber meets this requirement because the resonance is confined within a very subwavelength domain, and variations of the incident wavevector will not alter the nature of the resonance. The In_2O_3-based samples from Sec. 9.3.2 and Fig. 9.2 were destroyed during cross-sectional SEM analysis. This presented the opportunity to demonstrate the absorbing structure with a different dielectric spacer layer—SiO_2.

Angular dependence of absorbance is presented in Fig. 9.3; the experimental spectra are shown for multiple incidence angles and for both s and p polarizations. The wide-angle data were collected using the external beamline

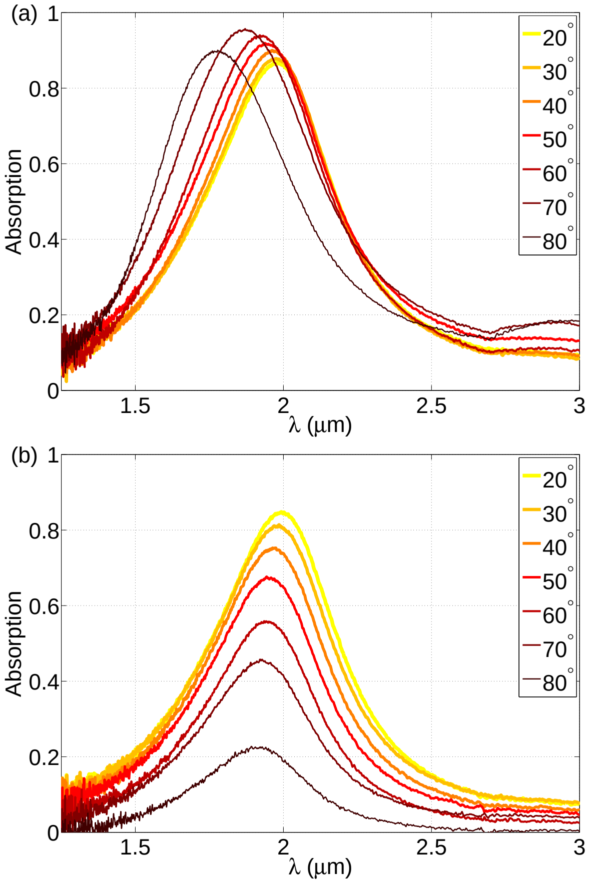

Figure 9.3: Plots of absorption as a function of wavelength at multiple incidence angles for the SiO_2-based perfect IR absorbing structure. Radiation is (a) *p*- and (b) *s*-polarized.

discussed in Ch. 8. The setup allows for variable incidence angles, polarization control, and a sub-mm spot size. The planar geometrical dimensions are $[L, W] = [300\text{ nm}, 230\text{ nm}]$. The experimental results are presented as a 2D color map in Fig. 9.4 (a,b) and can be compared to simulations in Fig. 9.4 (c,d). Radiation is *s*-polarized in the left panel (a,c) and *p*-polarized in the right panel

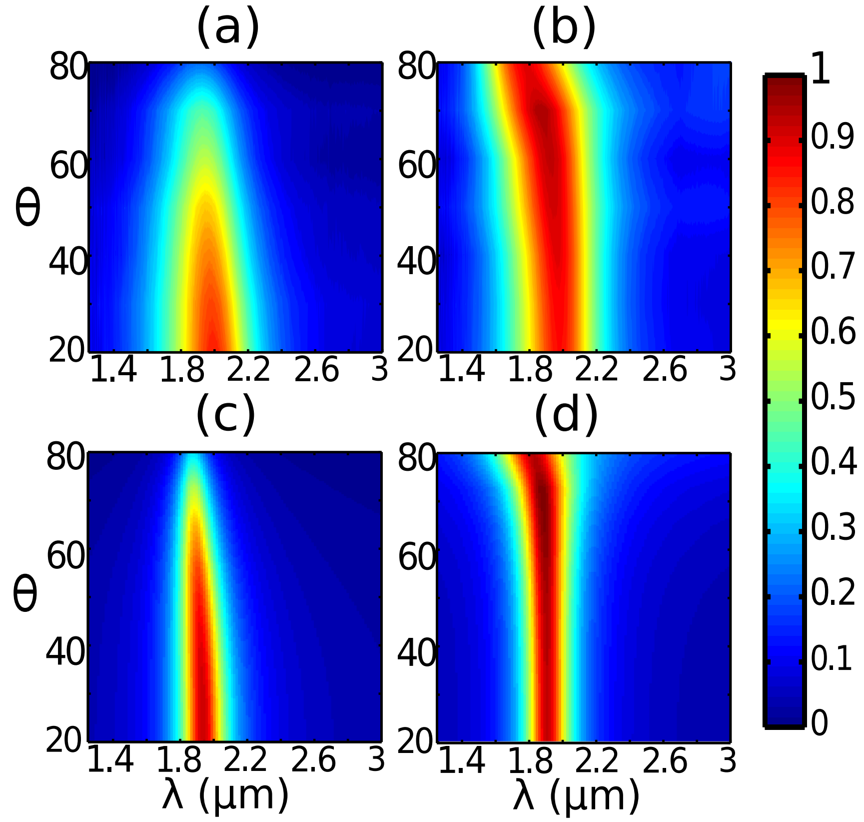

Figure 9.4: 2D color plots displaying the angular dependence of absorbance for the strip absorber. Left panel (a,c); data collected using s polarization. Right panel (b,d); data collected using p polarization. Top panel (a,b): experimental data interpolated from Fig. 9.3. Bottom panel (c,d): COMSOL simulation results on the absorbing structure. Theory courtesy of C. Wu.

(b,d). Experiments agree with theory, and large absorption persists for wide incident angles.

In principle, the radiative and resistive losses are also functions of the in-plane wavevectors k_y and k_z. Therefore, in addition to high absorbance over a wide range of incident angles, this metamaterial absorber can also be designed to have maximum absorbance at a specific angle. In the particular sample shown in Fig. 9.4, absorbance is a maximal 96 percent under *p*-polarized radiation and an incident angle of $\theta = 70°$, while at $\theta = 20°$, the absorbance is a slightly decreased 87 percent.

9.4 Extension of Absorbers to Advanced Structures and Devices

The metamaterial absorber proposed is polarization selective: it absorbs incident radiation with one polarization while almost completely reflecting the other. This property can be useful for such applications as thermal emitters, where controlling the polarization of emission is required. However, in other applications like solar harvesters and photodetectors, it is desired that the structure can absorb light of both polarizations. An isotropic structure absorbs incident radiation of both polarizations [65, 39]. Its design is similar to the strip absorber but consists of square patches. Because 90° rotation invariance exists, the structure absorbs with equal efficiency in both polarizations. The concept of critical coupling can still be applied, utilizing the same dependence of radiative and resistive losses on geometry.

9.5 Conclusions

In conclusion, a simple design of an ultra-thin, perfect infrared absorber was been demonstrated over a wide angular range. Its large absorbance is explained in terms of critical coupling, where the scattering cross-section is equal to the absorptive cross-section. The critical coupling perspective provides a guideline for designing metamaterial absorbers: using low-loss metals, the structure should be designed in such a way that the resonances have low radiative loss. Based on this theory, the Au strips and mirror in the proposed structure can be replaced by other metals. Furthermore, the spacer dielectric can be replaced by a semiconductor, as the application requires, as long as the radiative loss can be matched to the resistive loss. The samples in these experiments were prepared by step and flash imprint lithography, which resulted in samples as large as $(1.2\ \mathrm{mm})^2$ that demonstrated up to 96-percent absorption. Lastly, the absorbing frequency can be tuned by changing geometric parameters, a property that was demonstrated through FTIR micro-spectroscopic experiments.

Chapter 10

Prism-Coupled Surface Wave Particle Accelerator Based on Silicon Carbide

10.1 Introduction

Advanced accelerators are aimed at conserving funds and laboratory space, at the expense of ultra-high accelerating gradients (multi-GV/m). Modern lasers [83] can deliver sufficient energy to power large gradient (>100 MV/m) solid-state accelerator structures [78]. Such advanced structures are needed because laser fields are primarily transverse; the fields must be rotated into a longitudinal state to impart energy to a charged particle. The risk of electric breakdown [114], which is most severe for metal-based structures [87, 99], is decreased through the design of accelerators based entirely on semiconductors. One such design exploits the unique optical properties of SiC [93, 54]. The schematic of a near-field accelerating structure, which consists of a sub-wavelength gap between two thin SiC films grown on Si slabs [43]—is shown in Fig. 10.1. The device can be quickly and inexpensively manufactured using standard micro-fabrication techniques [93, 54], and has been experimentally implemented using a planar Si prism as a coupling device for incident radiation.

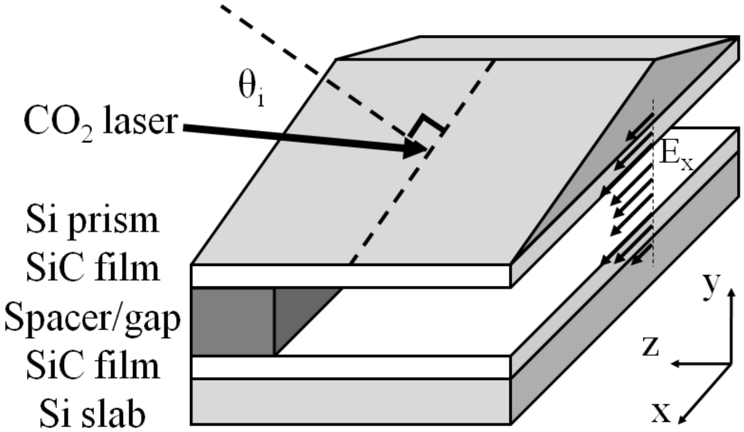

Figure 10.1: Schematic of the SiC-based accelerator (not to scale). Thin layers of SiC are grown on Si slabs that can be fabricated into prisms. The prism couples mid-IR radiation to the structure. A micro-fabricated spacer (one side shown) defines the few-micron, sub-λ gap. Electrons can then be accelerated via E_x. In the experimental sample, SiC films are 1.7-μm thick, the gap is 6.0-μm wide, and the Si slab is 5-mm thick. The prism is 1.78-mm tall, has a 15° in-coupling face slope, and a 28° out-coupling face slope.

Polar crystalline SiC exhibits a high tolerance heat loading and electrical breakdown (DC threshold $\sim$ 300 MV/m), making it an ideal choice for radio engineering devices working in hostile and high temperature (over 1000°C) environments [113]. Optically, SiC has a dielectric permittivity $\epsilon_{\mathrm{SiC}} < 0$ in the mid-IR *reststrahlen* band, which coincides with the operation range of efficient, commercial carbon dioxide ($\mathrm{CO_2}$) lasers ($\lambda \sim 10.6$ μm) and secures a widely available power source for the device. The accelerating channel is surrounded by flat, symmetric SiC surfaces and can support a near-luminous transverse magnetic (TM) mode with a multi-hundred MV/m gradient, appropriate for accelerating relativistic particles. This double-interface surface wave mode is similar to that occurring at the plasma/vacuum interface in a hollow channel plasma wakefield accelerator [89]. It can be excited from the side as shown in Fig. 10.1 using a dielectric prism. This structure is referred to as the Surface Wave Accelerator Based on SiC (SWABSiC). Both super-luminous ($v_{ph_x} > c$) and sub-luminous ($v_{ph_x} < c$) modes are experimentally demonstrated.

In this work, analytic theory was derived by Serguei Kalmykov, SiC film growth was performed by University Claude Bernard Lyon I collaborator Gabriel Ferro, and sample fabrication and laser spectroscopy were performed by Dmitriy Korobkin with the author. External-beam FTIR spectroscopy, numerical calculations, and data analysis were performed by the author.

10.2 Theoretical Description of the Multilayer Accelerator

The dispersion properties of the electromagnetic modes of an idealized SWABSiC are analytically solved. The structure consists of a flat, evacuated channel between two *infinitely thick* walls of cubic 3C-SiC [43] with complex permittivity given by Eq. 2.15, where the infinite-frequency permittivity $\epsilon_\infty = 6.7$, the longitudinal optical phonon frequency $\omega_{LO} = 970$ cm^{-1} ($\lambda_{LO} = 10.31$ μm), the transverse optical phonon frequency $\omega_{TO} = 794$ cm^{-1} ($\lambda_{TO} = 12.59$ μm), and SiC damping $\gamma = 4.75$ cm^{-1} [2]. The real and complex terms of ϵ_{SiC} will be refered to as

$$\epsilon_{\mathrm{SiC}}(\omega) = \epsilon'_{\mathrm{SiC}} + i\epsilon''_{\mathrm{SiC}}. \tag{10.1}$$

In the *reststrahlen* band, where $\lambda_{LO} < \lambda < \lambda_{TO}$ ($\lambda = 2\pi/k_0$ and $k_0 = \omega/c$), $\epsilon'_{\mathrm{SiC}} < 0$, which is valid within the entire range (10.66 μm–11.31 μm) of the line-tunable $^{13}CO_2$ laser [54].

10.2.1 Symmetric and Anti-Symmetric Waveguide Dispersion

A planar waveguide with a symmetry plane at $y = 0$ supports an accelerating transverse magnetic (TM) mode with a symmetric electric field component E_x (depicted in Fig. 10.1) and anti-symmetric E_y and H_z (referred to as "anti-symmetric TM"), when p-polarized (TM) incident radiation is used. Inside the evacuated channel,

$$H_z(|y| < a) = \frac{\sin(uy)}{\sin(ua)} e^{i\omega t - ik_x x}, \tag{10.2}$$

while in the accelerator's wall

$$H_z(|y| > a) = \pm e^{-q(|y|-a)+i\omega t - ik_x x}, \tag{10.3}$$

where the upper sign stands for $y > a$, and a is the coordinate of the interface from the symmetry plane (i.e., the gap width is $2a$). The electric field components are

$$E_x = \frac{c}{i\omega\epsilon}\frac{\partial H_z}{\partial y} \quad \text{and} \quad E_y = -\frac{ck_x}{\omega\epsilon} H_z. \tag{10.4}$$

The dispersion equation relates the complex propagation constant $k_x = k'_x + ik''_x$ (longitudinal wave number and attenuation rate, respectively) to the mode frequency ω. Applying the continuity of H_z and E_x at the interfaces

$(y = \pm a)$, the characteristic equation is obtained:

$$q = -\epsilon_{\mathrm{SiC}} \frac{u}{\tan(ua)}. \tag{10.5}$$

Writing out the wave equation, and recognizing that k_x is the same in each medium (via Snell's law), a transcendental equation is obtained that relates u and q:

$$q^2 + u^2 = (1 - \epsilon_{\mathrm{SiC}}) k_0^2 \equiv \frac{R^2}{a^2}. \tag{10.6}$$

The complex-valued quantity R^2 depends only on the physical constants of the media and the wavelength. Equations 10.5 and 10.6 determine all dispersion properties of the system; they reduce to the single equation for the complex parameter u,

$$\tan(ua) = -\epsilon_{\mathrm{SiC}} \frac{ua}{\sqrt{R^2 - (ua)^2}}. \tag{10.7}$$

Equation 10.7 was solved numerically using MATLAB to find complex $u(\omega)$, and therefore $k_x^2 = k_0^2 - u^2$, yielding the complex propagation constant.

The waveguide also supports a non-accelerating mode with symmetric H_z (referred to as "symmetric TM"). Briefly, this dispersion equation reads

$$\frac{1}{\tan(ua)} = \epsilon_{\mathrm{SiC}} \frac{ua}{\sqrt{R^2 - (ua)^2}}. \tag{10.8}$$

Equation 10.8 does not allow for near-luminous solutions; one strictly subluminous mode exists.

The anti-symmetric wave is super-luminous ($v_{ph_x} = \omega/|k_x'| > c$) when $u \approx u'$; thus, no electron can stay in phase with the accelerating field. The

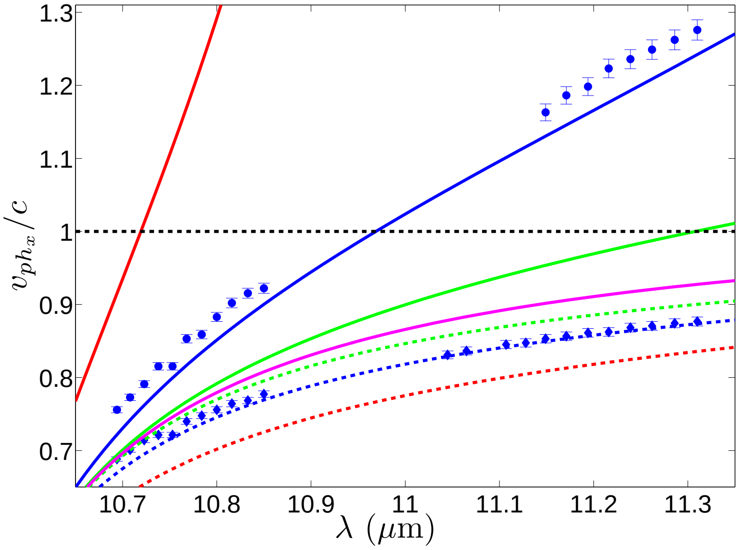

Figure 10.2: The longitudinal phase velocity, v_{ph_x}, is plotted for vacuum gap widths $2a = 4$ μm (red), 6 μm (blue), 9 μm (green), and ∞ (single interface, magenta). Experimental phase velocities (derived from Fig. 10.3 and other data) are included for the 6-μm gap case. Solid lines: anti-symmetric accelerating modes. Dashed lines: symmetric modes. Luminous modes ($v_{ph_x} \approx c$) are possible using $\lambda = 10.72$ μm (4 μm gap), 10.97 μm (6 μm gap), and 11.31 μm (9 μm gap).

mode becomes sub-luminous ($v_{ph_x} < c$) when $u \approx iu''$, which is only possible if $\epsilon'_{\text{SiC}} < -1$, and

$$k_0 a > k_0 a_{\text{lum}} = \frac{-\epsilon'_{\text{SiC}}}{\sqrt{1-\epsilon'_{\text{SiC}}}}. \tag{10.9}$$

The equality corresponds to $u = 0$ and $v_{\text{ph}_x} = c$. This guided TM mode can be interpreted as a superposition of two surface waves (SWs) or SPPs supported by the individual SiC–vacuum interfaces. Ideally, the energy of the accelerating electric field will be a large fraction of the total energy. Hence, the ratio

$$\Delta W = \frac{\int_{-a}^{a} |E_y|^2 dy}{\int_{-a}^{a} |E_x|^2 dy} \approx \frac{(k_0 a)^2}{3} \tag{10.10}$$

should not be much larger than unity, which then implies a sub-λ channel width is required.

The dispersion equation is numerically solved over the laser's operating range, and results are shown in Fig. 10.2. It was found that for $\lambda > 10.85$ μm, modes cannot propagate in channels narrower than $a = 3$ μm because SiC increasingly behaves as a conductor for longer wavelengths, and the cutoff condition ($a > \lambda/4$) applies. Furthermore, reducing the channel width increases the losses: $k_x''/k_x' > 0.1$ for $a = 2$ μm. Wider channels and longer wavelengths correspond to longer propagation distances ($L_{prop} \approx 200$ μm) and can be useful for laboratory implementation.

Dispersion curves for the symmetric (always sub-luminous) and anti-symmetric (luminous, *accelerating*) modes shown in Fig. 10.2 correspond to $2a_{lum} \approx 4$ μm and $\Delta W \approx 0.5$ for $\lambda = 10.72$ μm ($\epsilon'_{\mathrm{SiC}} = -2.05$), $2a_{lum} \approx 6$ μm and $\Delta W \approx 1.0$ for $\lambda = 10.97$ μm ($\epsilon'_{\mathrm{SiC}} = -3.75$), and $2a_{lum} \approx 9$ μm and $\Delta W \approx 2.1$ for $\lambda = 11.31$ μm ($\epsilon'_{\mathrm{SiC}} = -7.14$). It is clear that the single interface (infinite gap) cannot support luminous, accelerating modes. Experimental data for the 6 μm gap, which were derived from Fig. 10.3, are plotted with theory and show agreement.

10.3 Experimental Realization of the SiC Accelerator

10.3.1 Device Fabrication and Optical Setup

A schematic of the SiC-based accelerator is given in Fig. 10.1 (not to scale). Thin 1.7-μm-thick layers of SiC were grown [43] on Si slabs (5-mm thick). Dielectric Si is chosen for its compatibility with SiC growth and its capability of handling thermal and mechanical stress. One slab was fabricated into a planar prism (ISP Optics): the prism is 1.78-mm tall, has a 15° slope at the in-coupling face, and a 28° slope at the out-coupling face (refracted ray used for diagnostics). The prism surface couples mid-IR radiation to the accelerating structure. With the single prism/SiC structure, Kretschmann configuration SPPs can be excited [84], whereas a bare Si prism brought close (few microns) to a SiC surface can excite Otto-configuration SPPs [69]. The gap is defined by a micro-fabricated SiO_2 spacer with 6.0-μm thickness. The two sides were placed in contact, making a symmetric structure with a subwavelength-scale opening between the films. The structure is designed to permit electron acceleration in the x-direction.

In the prism-coupling scenario, a planar prism is fabricated from the Si slab and is used to excite accelerating modes inside the vacuum channel of the SWABSiC, as shown in Fig. 10.1. The Si prism has an index $n_{\mathrm{Si}} = 3.42$ ($\epsilon = n^2$) and supports a planar EM wave with a longitudinal wave number

$$k_{0x} = k_0 n_{\mathrm{Si}} \sin\theta_{\mathrm{Si}}, \tag{10.11}$$

where θ_{Si} is the incident angle within Si (and related through Snell's law to the laser's incidence angle from the prism normal, θ_i). The luminous mode corresponds to waves propagating along the interface with $v_{ph_x} \approx c$; rearranging Eq. 10.11,

$$\frac{\omega}{ck_x} = \frac{v_{ph_x}}{c} = \frac{1}{n_{\mathrm{Si}} \sin \theta_{\mathrm{Si}}}. \tag{10.12}$$

Thus, the luminous mode exists when $n_{\mathrm{Si}} \sin \theta_{\mathrm{Si}} = 1$, which, by Snell's law, occurs at the Si total internal reflection (critical) angle, $\theta_{\mathrm{Si}} = 17.0°$, or $\theta_i = 6.8°$ (θ_i is depicted in Fig. 10.1 and is used for Fig. 10.3 plots).

10.3.2 Infrared Spectroscopy and the Detection of Surface Modes

For cold tests (i.e., no particle injection), a line-tunable, CW $^{13}CO_2$ laser is used, and the reflection coefficient is measured as function of incident angle and frequency. The typical incident power was 400 mW. The $^{13}CO_2$ laser was combined with an alignment HeNe laser using a dichroic beam splitter. A 15-cm-focal length ZnSe lens focuses the 4.5-mm-diameter infrared beam. Experimental SiC accelerator reflection (i.e., prism refraction, with specular reflection excluded) spectra are shown in Fig. 10.3 with corresponding theory for selected $^{13}CO_2$ laser wavelengths: $\lambda = 10.723$ μm (red), 10.784 μm (blue), 10.850 μm (green), 11.065 μm (cyan), 11.128 μm (magenta), and 11.310 μm (black). Surface waves are marked by reflection minima as energy is converted into mode excitation. Wavelengths longer than 10.723 μm have been offset in R proportional to their $\Delta\lambda$ to smoothly show the SW transitions of the antisymmetric *accelerating* TM mode (smaller θ_i) and the symmetric TM mode (larger θ_i). Silicon prism refraction (no SiC) for 10.723 μm is included, showing

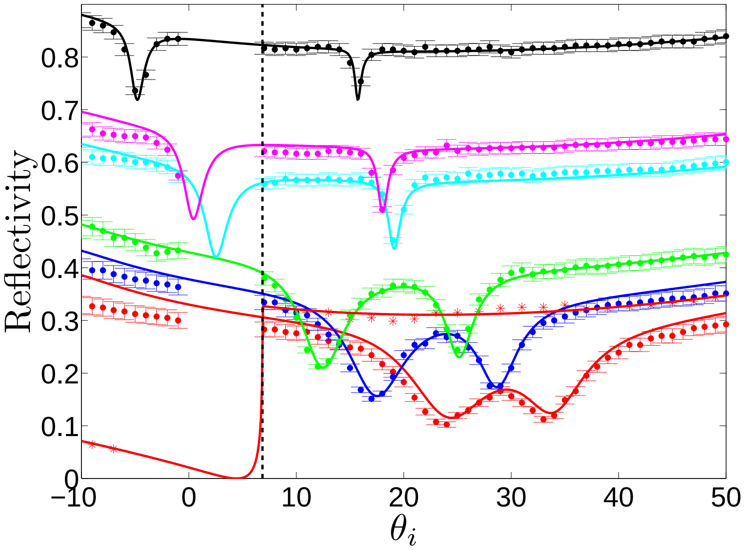

Figure 10.3: Experimental SiC accelerator reflection (i.e., prism refraction) spectra with corresponding theory for selected $^{13}CO_2$ laser wavelengths: $\lambda =$ 10.723 μm (red), 10.784 μm (blue), 10.850 μm (green), 11.065 μm (cyan), 11.128 μm (magenta), and 11.310 μm (black). Wavelengths longer than 10.723 μm have been offset in R proportional to $\Delta\lambda$ to smoothly show the behavior of the anti-symmetric *accelerating* TM mode (smaller θ_i) and the symmetric TM mode (larger θ_i). Si prism refraction (no SiC) for 10.723 μm is included, showing the angle required for the luminous mode ($v_{ph_x} \approx c$), marked by the dashed line at θ_{crit}.

the angle required for the luminous mode, marked by the dashed line at θ_{crit}.

Laser data are also shown as a two dimensional color plot in Fig. 10.4 (a), with analytical mode dispersion overlaid. It is seen that (i) reflectivity minima are in agreement with theory, and (ii) the anti-symmetric accelerating mode transition from sub-luminous to super-luminous is visible. The external FTIR beamline was also used to probe the system. The FTIR's incident power, which determines the final signal to noise ratio, was much lower than that from the laser. Also, the large beam divergence prevented the collection of refraction alone; both refraction and specular reflection were measured, reducing the SPP contrast. But the FTIR provided spectra across a wide IR range, which are plotted in Fig. 10.4 (b) as a color plot equivalent to the one depicting laser data. For reference, Fig. 10.4 (c) gives FTIR spectra for incident angles from 15° to 50°. To clearly distinguish SPP minima, p polarization scans were normalized to s polarization scans, producing a baseline ratio that decreases with angle, since p polarization vanishes when Brewster's angle (74°) is approached (Fig. 10.4 (b,c)).

One dimensional theory (solid lines) was calculated in MATLAB, uses driven EM waves, accounts for energy lost (i) by reflections at the first and second prism faces and (ii) by Ohmic loss within the Si prism, and shows excellent agreement with experiments. The prism was originally designed to maintain a separation of at least 4° between the specularly reflected ray and internally refracted ray for all incident angles $-90^\circ < \theta_i < 90^\circ$. With this flexibility comes a limitation: the luminous mode, which is excited at $\theta_i = 6.8^\circ$, is not accessible to diagnostics because the refracted ray is too close to the incident ray, resulting in the data gap (most clear in Fig. 10.3 (b)). Nevertheless, (i) sub-luminous and super-luminous modes were observed, and (ii) prisms with ideal geometries can be easily fabricated.

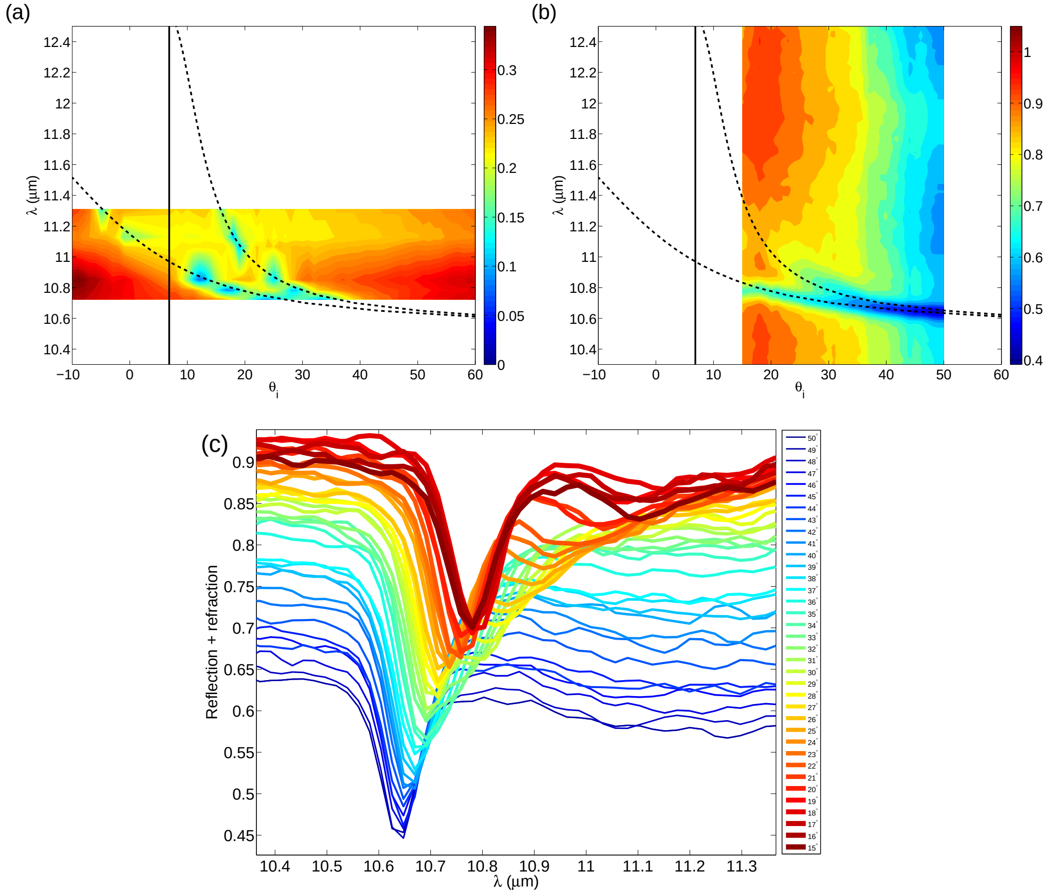

Figure 10.4: (a) Experimental data from Fig. 10.3 are plotted in two dimensions, with analytical theory overlaid showing the symmetric (upper line) and anti-symmetric (lower line) mode dispersion, in agreement with experimental reflectivity minima. (b) External beamline FTIR reflection data are plotted equivalently in 2D (*p*-polarized spectra normalized to *s* polarization). (c) External beam FTIR spectra are given in line format.

10.4 Conclusions

The electromagnetic properties of the symmetric and anti-symmetric transverse magnetic modes of the Surface Wave Accelerator Based on SiC were numerically studied and experimentally verified. The anti-symmetric accelerating mode exists in the gap between two SiC films grown on Si slabs, and is powered by a $^{13}CO_2$ laser. The accelerating cavity is a high-quality resonator with a relatively low geometrical loss factor. Therefore, moderate laser powers produce accelerating gradients on the order of a few hundred MV/m. Super-luminous ($v_{ph_x} > c$) and sub-luminous mode excitation by side-coupling through the triangular Si prism was demonstrated. Future work will seek to directly observe the luminous mode and make experimental advancement toward charged particle integration and acceleration.

Chapter 11

Conclusions

11.1 Summary of Results

The main scientific results of this dissertation will be summarized as follows.

In Chapter 2, an experimental demonstration of critical coupling to mid-infrared (IR) surface phonon-polaritons (SPPs) at the air/SiC interface in the Otto configuration was presented. Critical coupling is a maximal transference of incident radiation to propagating surface modes, and was observed by performing a double-scan of wavelength and incidence angle for two air gaps. It was theoretically shown that critical coupling occurs when coupling to and from the prism is equal to the sum of other SPP losses. Because critical coupling results in the largest electric field enhancement, mid-IR index sensing applications, which benefit from such enhancements, are made possible.

Small-volume index sensing with analyte specificity based on mid-IR SPPs at the SiC/analyte interface in the Otto configuration was presented in Chapter 3. Sensing was demonstrated by a double-scan of λ and θ for three analytes: air, mineral oil, and silicone oil. It was shown that SPP-based index sensing exploits the SPP resonance conditions and sensitivity to surrounding dielectric properties, and can probe volumes down to the pL-scale. Advanced mid-IR sensing applications are envisioned, and sensing can be tuned to specific bands for desired applications by using SPP-supporting materials such as AlN (11.2 μm–16.4 μm [73]) and GaP (24.8 μm–27.4 μm [112]).

Chapter 4 presented a theoretical and experimental investigation of extraordinary optical transmission (EOT) in mid-IR through a SiC metamaterial. The sample was a square array of round, subwavelength holes milled in an optically thin SiC air-bridged membrane. It was theoretically demonstrated and experimentally verified that EOT is accompanied by a blue shifted absorption peak, which corresponds to extraordinary optical absorption (EOA). Both EOT and EOA were shown to be caused by the excitation of surface phonon-polaritons in the modified film. Enhanced absorption (up to 40 percent) and transmission (up to 20 percent) are present for arrays in which holes occupied only 6 percent of the total area. Large absorbance suggests that perforated SiC films can be used as efficient, tunable thermal emission sources. Strong anisotropy with respect to array orientation has been demonstrated and explained, and can be used in sensing applications and as a diagnostic of sample orientation.

It was shown in Chapter 5 that the polarization state of *spoof* surface plasmons, which are supported in structured, perfect electric conductors, can be altered, controlled, and made chiral through interactions with other perforations in the metamaterial lattice. The metamaterial is a metal surface with rectangular holes that are rotated with respect to the array's square, subwavelength lattice by angle θ. Control is manifested by polarization rotation or "helicity," which induces EOT. The degree of EOT is determined by cross-polarized IR transmission micro-spectroscopy of seven samples, each with a different angle θ. Such unique dispersion and polarization control in IR spoof surface plasmon materials may pave the way for advanced photonic device.

Chapter 6 showed that by engineering individual subwavelength infrared antenna modes, the metamaterial properties of impedance and absorption can be controlled and optimized. First, cutting long antennas to subwavelength size reduces electric resonance and scattering, allowing for impedance control. Second, large, tunable absorption is created by generating a magneto-electric (bianisotropic) response in an asymmetric antenna/pedestal structure. This control was experimentally verified with a novel metal-free metamaterial array of 3D SiC antennas. Direct emission measurements taken at Sandia National Laboratories agree with absorption data collected with FTIR micro-spectroscopy, confirming Kirchhoff's law of emission, and demonstrating the metamaterial's potential as a tunable IR source. Antenna mode engineering through periodic and cross-sectional structuring improves the outlook for more efficient tunable metamaterial absorbers and infrared emission sources.

The benefits of Fourier transform infrared (FTIR) spectroscopy were presented in Chapter 7, the most important of which being its broad spectral range. It was then shown that the use of an infrared microscope allows for the collection of reflected and transmitted radiation from small ($(50\ \mu\text{m})^2$ to large $(100\ \mu\text{m})^2$) samples. It was reviewed that the microscope suffers from limitations that include a fixed incidence angle and large convergence/divergence that leads to wavevector averaging. The external FTIR beamline, which served as the major experimental development of this dissertation work and provides a remedy to the issues encountered with the microscope, was presented. Chapter 8 detailed the beamline's setup, focusing characterization, and usage. It was shown that the beamline's 200-μm spot size is limited to a select wavelength range by chromatic aberration, but that numerical renormalization compensates for this limitation, even permitting the study of samples smaller than the beam (e.g., 150-μm samples). Furthermore, a small-area array of gold antennas was used to verify the system's angle-dependent spectroscopic capability. With its small spot size, broadband IR range, control over polarization, and incidence angle tunability, the external beamline will support many innovative metamaterial projects.

Chapter 9 presented an excellent candidate for detailed measurements using the external FTIR beamline: the simple design of an ultra-thin, wide-angle, perfect IR absorber was demonstrated as such (up to 96 percent) from small (20°) to large (80°) incidence angles. The near-perfect absorption was explained in terms of critical coupling, where the scattering (radiative) cross-section is equal to the absorptive (resistive) cross-section. Samples in these experiments were prepared by step and flash imprint lithography, allowing the rapid fabrication of large-area metamaterials. It was discussed that the absorbing frequency can be tuned by changing geometric parameters, and that the structure can be designed to simultaneously absorb light of both polarizations by structuring in two dimensions.

The electromagnetic properties of the symmetric and anti-symmetric transverse magnetic modes of the Surface Wave Accelerator Based on SiC (SWABSiC) were numerically studied and experimentally verified in Chapter 10. The modes exist in the gap between two SiC films grown on Si slabs, and are powered by a $^{13}CO_2$ laser. The accelerating cavity is a high-quality resonator with a relatively low geometrical loss factor. Therefore, moderate laser powers produce accelerating gradients on the order of a few hundred MV/m. Super-luminous ($v_{ph_x} > c$) and sub-luminous mode excitation by side-coupling through the triangular Si prism was demonstrated. Future work will seek to directly observe the luminous mode and make experimental advancement toward charged particle integration and acceleration.

11.2 Directions for Future Research

Years ago, during a conversation on our doctoral research in experimental physics, a friend once said: “six years is not much time to get good work done.” While initially surprising, the statement has become reality: thoughtful science takes time, sometimes years, to plan, execute, and publish, and there are never enough resources—neither time nor funding—to pursue each great idea or improvement. In regard to the projects detailed in this dissertation, here are some future directions that were either not currently available or were limited by time or budget.

Experiments that demonstrated critical coupling to surface phonon-polaritons relied on micron-scale air gaps. Gaps of 3 μm and 5 μm were achieved by cleaning the sample and prism, placing them on the aluminum target holder, and then compressing the two, all in the clean room environment. Indeed, dirty samples often resulted in gaps exceeding 10 μm. One proven way to reduce the gap without the clean room requirement was to make smaller parts. In the work discussed, however, the prism was 1" in diameter, while the SiC/Si sample was 1.5" in diameter.

To test this small-parts method, one 8-mm round sample was cut, which resulted in a sub-micron gap. Therefore, a reduced sample and/or prism will permit reduced gaps, at the expense of handing difficulty. If precise gap tunability or small gaps are required, small components integrated with a variable gap apparatus [24] can be used.

Refractive index sensing with infrared laser radiation utilized a static fluid chamber. The fluid was placed between the prism and the SiC film, and compression reduced the gap to micron scale. Advanced experiments, and eventual commercialization, would require a dynamic flow chamber integrated with micro-fluidics. One such possibility would require a fixed gap between the prism and SiC, possibly defined by a thin dielectric film, with a narrow fluid channel etched within. With proper design, a flow of analyte could be maintained, and real-time signal monitoring would be possible.

Many advancements are possible with air-bridged SiC membrane metamaterials. While multiple array periods (5 μm and 7 μm) and hole diameters (1 μm and 2 μm) were fabricated, interesting physics may lie in other variations. Perforation designs beyond the round hole may also be of interest. The sample presented in this dissertation was fabricated with focused ion beam (FIB) milling, a process known to alter or destroy crystallinity [75]: such damage may prevent a permittivity less than zero, rendering a sample useless. Therefore, the tool should be used sparingly with SiC and other polar crystals. Additionally, FIB is slow (serial milling), expensive ($\geq$ \$50/hour), and requires a special shareware program run on MATLAB to create batch files ("streams" that define pixels to be milled) for milling large, periodic patterns. The FIB tool is commonly used because SiC is nearly diamond-hard and difficult to etch. One method that can etch SiC, however, was presented in Chapter 6: the inductively coupled plasma (ICP) etching tool quickly and anisotropically (vertical side walls) etches SiC, after a pattern is defined via photolithography or electron beam lithography (EBL). The ICP tool used is located at Sandia National Laboratories (Albuquerque, NM). While the University of Texas at Austin does not currently possess such a tool, it is recommended that this tool or similar tools are sought out for the fabrication of larger and more complicated SiC-based structures.

The square arrays of rectangular apertures demonstrated strong chirality or "helicity" as a sign of polarization control. But reflection and transmission spectra that were not cross-analyzed retained many complicated features and resonances. This is thought to arise from the dielectric (SiC) thickness: when the substrate thickness (1 μm) is comparable to wavelength (5 μm–10 μm), waveguiding effects become important. Two extreme alternatives have been proposed: the sample should be made on ultra-thick or ultra-thin films. The use of SiC is not necessarily required, since the wavelength of interest is shorter than SiC's *reststrahlen* band: instead, (i) a thick ($\geq$1 mm) substrate of CaF_2, or (ii) a thin (100 nm) film of silicon-on-insulator (where the middle SiO_2 layer provides an etch stop in membrane fabrication) could be used. Another improvement would come from EBL fabrication. Currently, samples are made via FIB, which makes sample fabrication difficult for arrays larger than (100 μm)^2. The EBL tool could be used to make large arrays (e.g., (300 μm)^2) more appropriate for the external FTIR beamline. With such advanced measurements, k_x can be varied through θ rotations and full dispersion diagrams can be explored.

Several improvements can be made to the external FTIR beamline system. A self-contained purge gas generator (compressor, air cleaner (CO_2), and air drier (H_2O)) was bought for the lab because FTIR spectroscopy spans the IR, a spectral range rich with absorption lines from atmospheric gasses. While the spectrometer and microscope are sealed and purged, the external beamline is not. The design and construction of an enclosure would make an excellent project for an undergraduate or new graduate student. In fact, a third and final port on the purge distribution manifold remains unused, just for this purpose. Another improvement has been proposed, though it is of lower priority. The beamline's height matches that of the FTIR ($\sim$ 4"). Lowering this height via a periscope (two mirrors on orthogonal planes) may increase IR beam stability and alignment, though such a procedure would more greatly benefit a visible-range laser experiment.

There is much to be done with the perfect IR absorber, as the project and applications are still quite new. As discussed, only one mask has been designed, with a limited number of metamaterial samples (nine variations, some of which did not provide viable samples), one design type (1D strips), and with only one metamaterial array size verified. Many innovations have been proposed, such as expanding the number of sample variations, increasing dimensionality (2D patches), and vastly increasing the array size (up to the device limitations, which greatly exceed $(1.2 \text{ mm})^2$). The incorporation of unconventional materials may result in interesting applications: it was proposed that replacing Au and SiO_2 with W and AlN, respectively, would allow the absorber to be used as a high-temperature, narrow-band thermal emitter. To date, multiple such samples have been made, but with no spectroscopic success. It is hoped that design and fabrication improvements will yield functional devices.

Lastly, the SiC accelerator has many exciting potential improvements. Most importantly, the luminous mode must be accessed, which will require a prism redesign. Collaborator Gabriel Ferro has grown one- to two-micron-thick SiC on Si bricks (5 mm) that was cut by the author from 2" rounds into 1 cm×2 cm rectangles using either the wafer dicing saw within the University of Texas at Austin's Center for Nano and Molecular Science and Technology (CNM) or the low-speed rock saw in the Geology department. These unfinished bricks may be designed such that the refracted ray, which carries information about the luminous excitation, exits the prism at an accessible angle (i.e., steered away from the incident laser beam). The current design of 15°/28° doesn't permit luminous mode observation, but it does have the benefit of maintaining a spacing larger than 4° between the refracted and specularly reflected rays for all incident angles. With the luminous mode observed, tests may begin to diagnose breakdown power, and with a sufficient laboratory expansion, the group may pursue electron injection and acceleration.

Appendix

Appendix 1

Target Stage Alignment Procedures

To diagnose the external FTIR beam's diameter in the focal plane, apertures were placed at the focus via x, y, and z stage adjustments. Because the stage has a rotation axis (Fig. 8.2), the axis should be placed in the beam's focus; this is achieved using two sets of x–z translators, referred to as X_{in}, Z_{in} and X_{out}, Z_{out}. The former set denotes the inner translators that place the sample at the rotation axis, and these values change for each sample. The latter set denotes the outer translators that place the rotation stage's axis at the IR beam's focus, and these values, once set, should remain valid for all samples. Focal point alignment is performed with Z_{out} and compensates for chromatic aberration, as reviewed in Sec. 8.8. Only one y translator (perpendicular to the table) is needed because no rotations (and thus no deviations) occur in that plane. Sample heights can be easily adjusted with the y translator at any time. Stage alignment procedures developed with Dmitriy Korobkin will be presented, with a real example set of data for future reference.

Simply placing a pinhole or sample into the IR's focus is trivial: either "inner" or "outer" translators can be used, but once rotations are initiated, the sample will "walk off" focus because the rotation stage does not necessar-

Coarse alignment			
Z_{in}	$X_{in}(\theta = 0°)$	$X_{in}(\theta = 30°)$	$X_{in}(\theta = -30°)$
0.400	0.439	0.467	0.405
0.425	0.439	0.453	0.419
0.450	0.439	0.437	0.433
0.475	0.439	0.422	0.448
0.500	0.439	0.408	0.462
Medium alignment			
0.455	0.439	0.434	0.436
0.460	0.439	0.433	0.439
0.465	0.439	0.428	0.441
Fine alignment			
0.452	0.439	0.4365	0.4345
0.454	0.439	**0.4345**	**0.4345**

Table A.1: Sample data collected during stage alignment using a 200-μm-diameter pinhole. Z_{in} is set to coarse, medium, and fine values for incident angles of $\theta = \pm 30°$. X_{in} is adjusted until the pinhole is in focus for each value of Z_{in}. The routine is repeated until X_{in} is equal (blue text) for both rotations: the sample is now coincident with the z plane (red text) of the rotation axis. All values are in units of inches, as specified by the translator.

ily coincide with the focal position. The first step to correct the axis/focus misalignment is to eliminate the z offset, ΔZ_{in}, between the sample (pinhole) and the rotation axis. The elimination of ΔZ_{in} will occur when the same x offset between the sample and the axis, ΔX_{in}, is required to return the pinhole to the focus when using symmetric rotations. Once the HeNe and IR beams are made coincident through the target pinhole, the visible HeNe beam can be used for all alignment steps but the last. Sample data are shown in Table A.1: the dependent variable Z_{in} is set to coarse values, and X_{in} is adjusted until

Coarse alignment		
X_{out}	$X_{in}(\theta = 0°)$	$X_{in}(\theta = 45°)$
0.950	0.459	0.454
0.975	0.483	0.490
1.000	0.509	0.525
1.025	0.534	0.562
Medium alignment		
0.955	0.464	0.462
0.960	0.469	0.470
0.965	0.474	0.476
0.970	0.479	0.483
Fine alignment		
0.957	0.4660	0.4645
0.959	0.4685	0.4675
0.960	**0.4680**	**0.4680**

Table A.2: Sample data collected during stage alignment using a 200-μm-diameter pinhole. Using zero and non-zero incident angles, X_{out} is set to coarse, medium, and fine adjustments until X_{in} no longer requires translations to place the pinhole back in focus. The result is a permanent value of X_{out} that corresponds to the (outer) x translator position that places the rotation stage's axis coincident with the beamline. All values are in units of inches, as specified by the translator.

light passes through the pinhole. Note that $X_{in}(\theta = 0°)$ remains constant: as x and z are orthogonal, changes in z will not alter x when $\theta = 0°$. The stage is rotated to $\theta = \pm 30°$, and X_{in} is adjusted until the HeNe beam is in focus. Using coarse, medium, and fine steps, the routine is repeated until X_{in} is equal for both rotations: the sample is now in the z plane of the rotation stage. Note that this value of Z_{in} is only applicable to this sample, but this intermediate step must be completed before proceeding.

The next step is to make the rotation stage's x axis coincident with the IR beam focal point. The external translator X_{out} is set to coarse, medium, and fine adjustments until X_{in} no longer requires translations to place the pinhole back in focus for zero and non-zero rotations (Table A.2). The result is a permanent value of X_{out} that corresponds to the outer x translator position that places the rotation stage's axis into the beamline. The pinhole is now coincident with the rotation stage's axis (with correct X_{in}, Z_{in}), and the rotation stage's x axis coincides with the IR beamline (with correct X_{out}).

The final step is to place the rotation axis in the IR beam's ideal focus: alignment is performed by monitoring transmitted IR power through the pinhole while adjusting Z_{out}. As the beam's waist will be minimal in focus, maximum IR transmission corresponds to an ideal Z_{out} position. With the stage aligned and an initial IR focus achieved, the detailed IR focal analysis of Sec. 8.8 and Sec. 8.9 was performed. Figure 8.7 provides data relating the ideal Z_{out} position with the wavelength range of interest.

List of Publications

The following is a list of published, accepted, or submitted manuscripts that resulted from work contributed by the author. Nearly complete manuscripts are also included. Refereed articles that have been published or accepted are denoted by *. This list is current as of the degree completion date.

1. [59]* D. Korobkin, Y. A. Urzhumov, B. Neuner III, C. Zorman, Z. Zhang, I. D. Mayergoyz, and G. Shvets, *Mid-infrared metamaterial based on perforated SiC membrane: engineering optical response using surface phonon polaritons*, Appl. Phys. A **88** (2007), 605.
2. [108]* Y. A. Urzhumov, D. Korobkin, B. Neuner III, C. Zorman, and G. Shvets, *Optical properties of sub-wavelength hole arrays in SiC membranes*, J. Opt. A: Pure Appl. Opt. **9** (2007), S322.
3. [69]* B. Neuner III, D. Korobkin, C. Fietz, D. Carole, G. Ferro, and G. Shvets, *Critically coupled surface phonon-polariton excitation in silicon carbide*, Opt. Lett. **34** (2009), 2667.
4. [70]* B. Neuner III, D. Korobkin, C. Fietz, D. Carole, G. Ferro, and G. Shvets, *Midinfrared index sensing of pL-scale analytes based on surface phonon polaritons in silicon carbide*, J. Phys. Chem. C **114** (2010), 7489.

5. [58]* D. Korobkin, B. Neuner III, C. Fietz, N. Jengenyes, G. Ferro, and G. Shvets, *Measurements of the negative refractive index of sub-diffraction waves propagating in an indefinite permittivity medium*, Opt. Express **18** (2010), 22734.
6. [68]* S. H. Mousavi, A. B. Khanikaev, B. Neuner III, Y. Avitzour, D. Korobkin, G. Ferro, and G. Shvets, *Highly confined hybrid spoof surface plasmons in ultrathin metal-dielectric heterostructures*, Phys. Rev. Lett. **105** (2010), 176803.
7. [85]* S. Rajasekhara, B. Neuner III, C. A. Zorman, G. Ferro, G. Shvets, P. J. Ferreira, and D. Kovar, *The influence of impurities and planar defects on the optical performance of silicon carbide films*, Appl. Phys. Lett. **accepted** (2011), L10–10303R1.
8. [118] C. Wu, B. Neuner III, J. John, A. Milder, B. Zollars, S. Savoy, and G. Shvets, *Large-area, wide-angle, spectrally selective plasmonic absorber*, Phys. Rev. B **submitted** (2011).
9. [57] A. B. Khanikaev, S. H. Mousavi, B. Neuner III, and G. Shvets, *Tailoring the polarization state of spoof surface plasmons with chiral metal surfaces*, **manuscript in progress** (2011).
10. [72] B. Neuner III, C. Wu, G. Ten Eyck, M. Sinclair, I. Brener, and G. Shvets, *Low-albedo metamaterial array of silicon carbide antennas*, **manuscript in progress** (2011).

11. [71] B. Neuner III, D. Korobkin, S. Kalmykov, and G. Shvets, *Prism-coupled accelerator based on surface wave excitation in silicon carbide*, **manuscript in progress** (2011).

Bibliography

[1] R. Adato, A. A. Yanik, J. J. Amsden, D. L. Kaplan, F. G. Omenetto, M. K. Hong, S. Erramilli, and H. Altug, *Ultra-sensitive vibrational spectroscopy of protein monolayers with plasmonic nanoantenna arrays*, Proc. Natl. Acad. Sci. USA **106** (2009), 19227.

[2] S. A. Alterovitz, J. A. Woollam, and E. D. Palik (ed.), *"Cubic Silicon Carbide (β-SiC)," Handbook of Optical Constants of Solids*, Academic, New York, NY, 1991.

[3] E. Altewischer, M. P. van Exter, and J. P. Woerdman, *Polarization analysis of propagating surface plasmons in a subwavelength hole array*, J. Opt. Soc. Am. B **20** (2003), 1927.

[4] A. Alu and N. Engheta, *Guided modes in a waveguide filled with a pair of single-negative (sng), double-negative (dng), and/or double-positive (dps) layers*, IEEE Trans. Microw. Th. Tech. **52** (2004), 199.

[5] Y. Avitzour, Y. A. Urzhumov, and G. Shvets, *Wide-angle infrared absorber based on a negative-index plasmonic metamaterial*, Phys. Rev. B **79** (2009), 045131.

[6] I. Balin, N. Dahan, V. Kleiner, and E. Hasman, *Slow surface phonon*

polaritons for sensing in the midinfrared spectrum, Appl. Phys. Lett. **94** (2009), 111112.

[7] W. L. Barnes, A. Dereux, and T. W. Ebbesen, *Surface plasmon subwavelength optics*, Nature **424** (2003), 824.

[8] W. L. Barnes, W. A. Murray, J. Dintiger, E. Devaux, and T. W. Ebbesen, *Surface plasmon polaritons and their role in the enhanced transmission of light through periodic arrays of subwavelength holes in a metal film*, Phys. Rev. Lett. **92** (2004), 107401.

[9] D. Bergman and D. Stroud, *Physical properties of macroscopically inhomogeneous media*, Solid State Phys. **46** (1992), 147.

[10] H. A. Bethe, *Theory of diffraction by small holes*, Phys. Rev. **66** (1944), 163.

[11] M. Born and E. Wolf, *Principles of optics*, Cambridge University Press, Cambridge, England, 1999.

[12] V. V. Bryksin, Yu. M. Gerbshtein, and D. N. Mirlin, *Experimental study of surface optical modes in ionic crystal slabs*, Phys. Stat. Sol. B **51** (1972), 901.

[13] J. Burke, K. Wang, and A. Bramble, *Null test of an off-axis parabolic mirror. I. Configuration with spherical reference wave and flat return surface*, Opt. Express **17** (2009), 3196.

[14] G. F. Cairns, S. M. O'Prey, and P. Dawson, *Variable temperature, variable-gap Otto prism coupler for use in a vacuum environment*, Rev. Sci. Instrum. **71** (2000), 4213.

[15] Q. Cao and P. Lalanne, *Negative role of surface plasmons in the transmission of metallic gratings with very narrow slits*, Phys. Rev. Lett **88** (2002), 057403.

[16] S.-H. Chang, S. K. Gray, and G. C. Schatz, *Surface plasmon generation and light transmission by isolated nanoholes and arrays of nanoholes in thin metal films*, Opt. Express **13** (2005), 3150.

[17] D.-Z. A. Chen and G. Chen, *Measurement of silicon dioxide surface phonon-polariton propagation length by attenuated total reflection*, Appl. Phys. Lett. **91** (2007), 121906.

[18] D.-Z. A. Chen, A. Narayanaswamy, and G. Chen, *Surface phonon-polariton mediated thermal conductivity enhancement of amorphous thin films*, Phys. Rev. B **72** (2005), 155435.

[19] H.-T. Chen, J. F. O'Hara, A. K. Azad, A. J. Taylor, R. D. Averitt, D. B. Shrekenhamer, and W. J. Padilla, *Experimental demonstration of frequency-agile terahertz metamaterials*, Nature Photon. **2** (2008), 295.

[20] J. V. Coe, S. M. Williams, K. R. Rodriguez, S. Teeters-Kennedy, A. Sudnitsyn, and F. Hrovat, *Extraordinary IR transmission with metallic arrays of subwavelength holes*, Anal. Chem. **78** (2006), 1385.

[21] T. J. Coutts, *A review of progress in thermophotovoltaic generation of electricity*, Renewable and Sustainable Energy Rev. **3** (1999), 77.

[22] K. B. Crozier, A. Sundaramurthy, G. S. Kino, and C. F. Quate, *Optical antennas: resonators for local field enhancement*, J. Appl. Phys. **94** (2003), 4632.

[23] D. H. Dawes, R. C. McPhedran, and L. B. Whitbourn, *Thin capacitive meshes on a dielectric boundary: theory and experiment*, Appl. Opt. **28** (1989), 3489.

[24] P. Dawson, G. F. Cairns, and S. M. O'Prey, *Prism coupler with variable coupling gap*, Rev. Sci. Instrum. **71** (2000), 4208.

[25] A. Degiron, H. J. Lezec, W. L. Barnes, and T. W. Ebbesen, *Effects of hole depth on enhanced light transmission through subwavelength apertures*, Appl. Phys. Lett. **81** (2002), 4327.

[26] M. Diem, T. Koschny, and C. M. Soukoulis, *Wide-angle perfect absorber/thermal emitter in the terahertz regime*, Phys. Rev. B **79** (2009), 033101.

[27] G. Dolling, C. Enkrich, M. Wegener, C. M. Soukoulis, and S. Linden, *Simultaneous negative phase and group velocity of light in a metamaterial*, Science **312** (2006), 892.

[28] T. W. Ebbesen, H. J. Lezec, H. F. Ghaemi, T. Thio, and P. A. Wolff, *Extraordinary optical transmission through sub-wavelength hole arrays*, Nature **391** (1998), 667.

[29] J. A. Fan, C. Wu, K. Bao, J. Bao, R. Bardhan, N. J. Halas, V. N. Manoharan, P. Nordlander, G. Shvets, and F. Capasso, *Self-assembled plasmonic nanoparticle clusters*, Science **328** (2010), 1135.

[30] N. Fang, H. Lee, C. Sun, and X. Zhang, *Subdiffraction-limited optical imaging with a silver superlens*, Science **308** (2005), 534.

[31] L. Feng, Z. Liu, V. Lomakin, and Y. Fainman, *Form birefringence metal and its plasmonic anisotropy*, Appl. Phys. Lett. **96** (2010), 041112.

[32] Y. Fuzi, G. W. Bradberry, and J. R. Sambles, *Infrared surface plasmon-polaritons on Ni, Pd and Pt*, J. Mod. Optics **36** (1989), 1405.

[33] A. Ganjoo, H. Jain, C. Yu, J. Irudayaraj, and C.G. Pantano, *Detection and fingerprinting of pathogens: mid-IR biosensor using amorphous chalcogenide films*, J. Non Cry. Sol. **354** (2008), 2757.

[34] C. Genet, M. P. van Exter, and J. P. Woerdman, *Fano-type interpretation of red shifts and red tails in hole array transmission spectra*, Opt. Commun. **225** (2003), 331.

[35] F. Gervais and B. Piriou, *Temperature dependence of transverse- and longitudinal-optic modes in* TiO_2 *(rutile)*, Phys. Rev. B **10** (1974), 1642.

[36] J. Giergiel, C.E. Reed, S. Ushioda, and J.C. Hemminger, *Attenuated-total-reflection study of pyridine overlayers on silver films*, Phys. Rev. B **31** (1985), 3323.

[37] J.-J. Greffet, R. Carminati, K. Joulain, J.-P. Mulet, S. Mainguy, and Y. Chen, *Highly directional radiation generated by a tungsten thermal source*, Nature **416** (2002), 61.

[38] K. P. Gurton, D. Ligon, and R. Dahmani, *Measured infrared optical cross sections for a variety of chemical and biological aerosol simulants*, Appl. Opt. **43** (2004), 4564.

[39] J. Hao, J. Wang, X. Liu, W. J. Padilla, L. Zhou, and M. Qiu, *High performance optical absorber based on a plasmonic metamaterial*, Appl. Phys. Lett. **96** (2010), 251104.

[40] N. J. Harrick, *Internal reflection spectroscopy*, Interscience, New York, NY, 1967.

[41] H. M. Heise, R. Marbach, Th. Koschinsky, and F. A. Gries, *Multi-component assay for blood substrates in human plasma by mid-infrared spectroscopy and its evaluation for clinical analysis*, Appl. Spectrosc. **48** (1994), 85.

[42] S. Herminjard, L. Sirigu, H-P. Herzig, E. Studemann, A. Crottini, J.-P. Pellaux, T. Gresch, M. Fischer, and J. Faist, *Surface plasmon reso-*

nance sensor showing enhanced sensitivity for CO_2 detection in the mid-infrared range, Opt. Express **17** (2009), 293.

[43] M. J. Hernandez, G. Ferro, T. Chassagne, J. Dazord, and Y. Monteil, *Study of surface defects on 3C-SiC films grown on Si(111) by CVD*, J. Crystal Growth **253** (2003), 95.

[44] H. Hertz, *Uber electrodynamische wellen im luftraume und deren reflexion*, Annalen der Physik und Chemie **270** (1888), 609.

[45] R. Hillenbrand, *Towards phonon photonics - scattering-type near-field optical microscopy reveals phonon-enhanced near-field interaction*, Ultramicroscopy **100** (2004), 421.

[46] R. Hillenbrand, T. Taubner, and F. Keilmann, *Phonon-enhanced light-matter interaction at the nanometre scale*, Nature **418** (2002), 159.

[47] A. J. Hoffman, L. Alekseyev, S. S. Howard, K. J. Franz, D. Wasserman, V. A. Podolskiy, E. E. Narimanov, D. L. Sivco, and C. Gmachl, *Negative refraction in semiconductor metamaterials*, Nat. Mater. **6** (2007), 946.

[48] J. Homola, S. Yee, and G. Gauglitz, *Surface plasmon resonance sensors: review*, Sens. Actuators B **54** (1999), 3.

[49] K. C. Huang, M. L. Povinelli, and J. D. Joannopoulos, *Negative effective permeability in polaritonic photonic crystals*, Appl. Phys. Lett. **85** (2004), 543.

[50] A. Huber, N. Ocelic, D. Kazantsev, and R. Hillenbrand, *Near-field imaging of mid-infrared surface phonon polariton propagation*, Appl. Phys. Lett. **87** (2005), 081103.

[51] J. D. Jackson, *Classical electrodynamics*, Wiley, New York, 1998.

[52] S.C. Johnson, T.C. Bailey, M.D. Dickey, B.J. Smith, E.K. Kim, D.P. Mancini, W.J. Dauksher, K.J. Nordquist, and D.J. Resnick, *Advances in step and flash imprint lithography*, Proc. SPIE **5037** (2003), 197.

[53] S. F. Johnston, *Fourier transform infrared*, Ellis Horwood London, 1991.

[54] S. Kalmykov, O. Polomarov, D. Korobkin, J. Otwinowski, J. Power, and G. Shvets, *Novel techniques of laser acceleration: from structures to plasmas*, Phil. Trans. R. Soc. A **364** (2006), 725.

[55] J. Kauppinen and J. Partanen, *Fourier transforms in spectroscopy*, Wiley-VCH Verlag Berlin, 2001.

[56] M. C. Kemp, P. F. Taday, B. E. Cole, J. A. Cluff, A. J. Fitzgerald, and W. R. Tribe, *Security applications of terahertz technology*, Proc. SPIE **5070** (2003), 44.

[57] A. B. Khanikaev, S. H. Mousavi, B. Neuner III, and G. Shvets, *Tailoring the polarization state of spoof surface plasmons with chiral metal surfaces*, **manuscript in progress** (2011).

[58] D. Korobkin, B. Neuner III, C. Fietz, N. Jengenyes, G. Ferro, and G. Shvets, *Measurements of the negative refractive index of sub-diffraction waves propagating in an indefinite permittivity medium*, Opt. Express **18** (2010), 22734.

[59] D. Korobkin, Y. A. Urzhumov, B. Neuner III, C. Zorman, Z. Zhang, I. D. Mayergoyz, and G. Shvets, *Mid-infrared metamaterial based on perforated SiC membrane: engineering optical response using surface phonon polaritons*, Appl. Phys. A **88** (2007), 605.

[60] N. Kuroda, Y. Iida, T. Shigeta, H. Watanabe, and J. Watanabe, *Infrared attenuated total reflection by chemomechanically polished (0001) surface of 6H-SiC*, Jpn. J. Appl. Phys. **42** (2003), L1241.

[61] M. Laroche, R. Carminati, and J. J. Greffet, *Near-field thermophotovoltaic energy conversion*, J. Appl. Phys. **100** (2006), 063704.

[62] Y. H. Lee, *Alignment of an off-axis mirror with two parallel He-Ne laser beams*, Opt. Eng. **31** (1992), 2287.

[63] H. Lezec and T. Thio, *Diffracted evanescent wave model for enhanced and suppressed optical transmission through subwavelength hole arrays*, Opt. Express **12** (2004), 3629.

[64] Z. Li, K. Aydin, and E. Ozbay, *Determination of the effective constitutive parameters of bianisotropic metamaterials from reflection and transmission coefficients*, Phys. Rev. E **79** (2009), 026610.

[65] N. Liu, M. Mesch, T. Weiss, M. Hentschel, and H. Giessen, *Infrared perfect absorber and its application as plasmonic sensor*, Nano Lett. **10** (2010), 2342.

[66] B. Maddams, *How does FTIR work?*, Int. J. Vibr. Spec. **5** (2001), 2.

[67] L. Martin-Moreno, F. J. Garcia-Vidal, H. Lezec, K. M. Pellerin, T. Thio, J. B. Pendry, and T. W. Ebbesen, *Theory of extraordinary optical transmission through subwavelength hole arrays*, Phys. Rev. Lett. **86** (2001), 1114.

[68] S. H. Mousavi, A. B. Khanikaev, B. Neuner III, Y. Avitzour, D. Korobkin, G. Ferro, and G. Shvets, *Highly confined hybrid spoof surface plasmons in ultrathin metal-dielectric heterostructures*, Phys. Rev. Lett. **105** (2010), 176803.

[69] B. Neuner III, D. Korobkin, C. Fietz, D. Carole, G. Ferro, and G. Shvets, *Critically coupled surface phonon-polariton excitation in silicon carbide*, Opt. Lett. **34** (2009), 2667.

[70] ———, *Midinfrared index sensing of pL-scale analytes based on surface phonon polaritons in silicon carbide*, J. Phys. Chem. C **114** (2010), 7489.

[71] B. Neuner III, D. Korobkin, S. Kalmykov, and G. Shvets, *Prism-coupled accelerator based on surface wave excitation in silicon carbide*, **manuscript in progress** (2011).

[72] B. Neuner III, C. Wu, G. Ten Eyck, M. Sinclair, I. Brener, and G. Shvets, *Low-albedo metamaterial array of silicon carbide antennas*, **manuscript in progress** (2011).

[73] S. S. Ng, Z. Hassan, and H. A. Hassan, *Experimental and theoretical studies of surface phonon polariton of AlN thin film*, Appl. Phys. Lett. **90** (2007), 081902.

[74] L. Novotny, *Effective wavelength scaling for optical antennas*, Phys. Rev. Lett. **98** (2007), 266802.

[75] N. Ocelic and R. Hillenbrand, *Subwavelength-scale tailoring of surface phonon polaritons by focused ion-beam implantation*, Nat. Mater. **3** (2004), 606.

[76] D. Olego and M. Cardona, *Temperature dependence of the optical phonons and transverse effective charge in 3C-SiC*, Phys. Rev. B **25** (1982), 3889.

[77] A. Otto, *Excitation of nonradiative surface plasma waves in silver by the method of frustrated total reflection*, Z. Phys. **216** (1968), 398.

[78] R. B. Palmer, N. Baggett, J. Claus, R. Fernow, I. Stumer, H. Figueroa, N. Kroll, W. Funk, G. Lee-Whiting, M. Pickup, P. Goldstone, K. Lee, P. Corkum, and T. Himel, *Report of near field group*, AIP Conf. Proc. **130** (1985), 234.

[79] J. B. Pendry, *Negative refraction makes a perfect lens*, Phys. Rev. Lett. **85** (2000), 3966.

[80] J. B. Pendry, A. J. Holden, D. J. Robbins, and W. J. Stewart, *Magnetism from conductors and enhanced nonlinear phenomena*, IEEE Trans. Microwave Theory Tech. **47** (1999), 2075.

[81] J. B. Pendry, L. Martin-Moreno, and F. J. Garcia-Vidal, *Mimicking surface plasmons with structured surfaces*, Science **305** (2004), 847.

[82] E. Plum, V. A. Fedotov, and N. I. Zheludev, *Optical activity in extrinsically chiral metamaterial*, Appl. Phys. Lett. **93** (2008), 191911.

[83] I. V. Pogorelsky, J. Fischer, K. P. Kusche, M. Babzien, N. A. Kurnit, I. J. Bigio, R. F. Harrison, and T. Shimada, *Subnanosecond multi-gigawatt* CO_2 *laser*, IEEE J. Quantum Electron. **31** (1995), 556.

[84] H. Raether, *Surface plasmons on smooth and rough surfaces and on gratings*, Springer-Verlag, Berlin, Germany, 1988.

[85] S. Rajasekhara, B. Neuner III, C. A. Zorman, G. Ferro, G. Shvets, P. J. Ferreira, and D. Kovar, *The influence of impurities and planar defects on the optical performance of silicon carbide films*, Appl. Phys. Lett. **accepted** (2011), L10–10303R1.

[86] P. Roepstorff, C. P. Sonksen, O. Jansson, and M. Hamalainen, *A powerful combination: BIACORE 3000 and MALDI-TOF MS*, Biajournal **6** (1999), 9.

[87] J. Rosenzweig, A. Murokh, and C. Pellegrini, *A proposed dielectric-loaded resonant laser accelerator*, Phys. Rev. Lett. **74** (1995), 2467.

[88] M. Sarrazin, J. P. Vigneron, and J.-M. Vigoureux, *Role of wood anomalies in optical properties of thin metallic films with a bidimensional array of subwavelength holes*, Phys. Rev. B **67** (2003), 085415.

[89] C. B. Schroeder, D. H. Whittum, and J. S. Wurtele, *Multimode analysis of the hollow plasma channel wakefield accelerator*, Phys. Rev. Lett. **82** (1999), 1177.

[90] J. A. Schuller, T. Taubner, and M. L. Brongersma, *Optical antenna thermal emitters*, Nature Photon. **3** (2009), 658.

[91] J. A. Schuller, R. Zia, T. Taubner, and M. L. Brongersma, *Dielectric metamaterials based on electric and magnetic resonances of silicon carbide particles*, Phys. Rev. Lett. **99** (2007), 107401.

[92] D. Schurig, J. J. Mock, B. J. Justice, S. A. Cummer, J. B. Pendry, A. F. Starr, and D. R. Smith, *Metamaterial electromagnetic cloak at microwave frequencies*, Science **314** (2006), 977.

[93] G. Shvets and S. Kalmykov, *Design and fabrication of a surface-wave accelerator based on silicon carbide*, AIP Conf. Proc. **737** (2004), 983.

[94] G. Shvets and Y. Urzhumov, *Engineering the electromagnetic properties of periodic nanostructures using electrostatic resonances*, Phys. Rev. Lett. **93** (2004), 243902.

[95] B. C. Smith, *Fundamentals of Fourier transform infrared spectroscopy*, CRC Press, Florida, 1996.

[96] D. R. Smith, W. J. Padilla, D. C. Vier, S. C. Nemat-Nasser, and S. Schultz, *Composite medium with simultaneously negative permeability and permittivity*, Phys. Rev. Lett. **84** (2000), 4184.

[97] T. I. Smith, *The source issue in infrared microspectroscopy*, Nucl. Instr. and Meth. **483** (2002), 565.

[98] W. G. Spitzer, D. Kleinman, and D. Walsh, *Infrared properties of hexagonal silicon carbide*, Phys. Rev. **113** (1959), 127.

[99] L. C. Steinhauer and W. D. Kimura, *Slow waves in microchannel metal waveguides and application to particle acceleration*, Phys. Rev. ST Accel. Beams **6** (2003), 061302.

[100] M. E. Stewart, N. H. Mack, V. Malyarchuk, J. A. N. T. Soares, T.-W. Lee, S. K. Gray, R. G. Nuzzo, and J. A. Rogers, *Quantitative multispectral biosensing and 1D imaging using quasi-3D plasmonic crystals*, Proc. Nat. Acad. Sci. **103** (2006), 17143.

[101] M. I. Stockman, S. V. Faleev, and D. J. Bergman, *Localization versus delocalization of surface plasmons in nanosystems: Can one state have both characteristics?*, Phys. Rev. Lett. **87** (2001), 167401.

[102] T. H. Taminiau, R. J. Moerland, F. B. Segerink, L. Kuipers, and N. F. van Hulst, *Lambda/4 resonance of an optical monopole antenna probed by single molecule fluorescence*, Nano Lett. **7** (2007), 28.

[103] L. Tang, S. E. Kocabas, S. Latif, A. K. Okyay, D.-S. Ly-Gagnon, K. C. Saraswat, and D. A. B. Miller, *Nanometre-scale germanium photodetector enhanced by a near-infrared dipole antenna*, Nature Photon. **2** (2008), 226.

[104] T. Taubner, D. Korobkin, Y. Urzhumov, G. Shvets, and R. Hillenbrand, *Near-field microscopy through a SiC superlens*, Science **313** (2006), 1595.

[105] K. A. Tetz, L. Pang, and Y. Fainman, *High-resolution surface plasmon resonance sensor based on linewidth-optimized nanohole array transmittance*, Opt. Lett. **31** (2006), 1528.

[106] K. Torii, T. Koga, T. Sota, T. Azuhata, S. F. Chichibu, and S. Nakamura, *An attenuated-total-reflection study on the surface phonon-polariton in GaN*, J. Phys.: Condens. Matter **12** (2000), 7041.

[107] K. Tvingstedt, N. K. Persson, O. Inganas, A. Rahachou, and I. V. Zozoulenko, *Surface plasmon increase absorption in polymer photovoltaic cells*, Appl. Phys. Lett. **91** (2007), 113514.

[108] Y. A. Urzhumov, D. Korobkin, B. Neuner III, C. Zorman, and G. Shvets, *Optical properties of sub-wavelength hole arrays in SiC membranes*, J. Opt. A: Pure Appl. Opt. **9** (2007), S322.

[109] N. Verellen, Y. Sonnefraud, H. Sobhani, F. Hao, V. V. Moshchalkov, P. V. Dorpe, P. Nordlander, and S. A. Maier, *Fano resonances in individual coherent plasmonic nanocavities*, Nano Lett. **9** (2009), 1663.

[110] V. G. Veselago, *The electrodynamics of substances with simultaneously negative values of ϵ and μ*, Soviet Physics Uspekhi **10** (1968), 509.

[111] K. Vynck, D. Felbacq, E. Centeno, A. I. Cabuz, D. Cassagne, and B. Guizal, *All-dielectric rod-type metamaterials at optical frequencies*, Phys. Rev. Lett. **102** (2009), 133901.

[112] J. Watanabe, K. Uchinokura, and T. Sekine, *Surface-phonon polariton on gratings of GaP thin slabs: Raman scattering*, Phys. Rev. B **40** (1989), 7860.

[113] C. E. Weitzel, J.W. Palmour, C. H. Carter Jr., K. Moore, K. K. Nordquist, S. Allen, C. Thero, and M. Bhatnagar, *Silicon carbide high-power devices*, IEEE Trans. Electron Devices **43** (1996), 1732.

[114] D. H. Whittum, *Ultimate gradient in solid-state accelerators*, AIP Conf. Proc. **472** (1999), 72.

[115] M. B. J. Wijesundara, G. Valente, W. R. Ashurst, R. T. Howe, A. P. Pisano, C. Carraro, and R. Maboudian, *Single-source chemical vapor deposition of 3C-SiC films in a LPCVD reactor*, J. Electrochem. Soc. **151** (2004), C210–C214.

[116] S. M. Williams, K. R. Rodriguez, S. Teeters-Kennedy, S. Shah, T. M. Rogers, A. D. Stafford, and J. V. Coe, *Scaffolding for nanotechnology: extraordinary infrared transmission of metal microarrays for stacked sensors and surface spectroscopy*, Nanotechnology **15** (2004), S495.

[117] C. Wu, Y. Avitzour, and G. Shvets, *Ultra-thin, wide-angle perfect absorber for infrared frequencies*, Proc. SPIE **7029** (2008), 70290W.

[118] C. Wu, B. Neuner III, J. John, A. Milder, B. Zollars, S. Savoy, and G. Shvets, *Large-area, wide-angle, spectrally selective plasmonic absorber*, Phys. Rev. B **submitted** (2011).

[119] S. Zhang, W. Fan, N. C. Panoiu, K. J. Malloy, R. M. Osgood, and S. R. J. Brueck, *Experimental demonstration of near-infrared negative-index metamaterials*, Phys. Rev. Lett. **94** (2005), 137404.

[120] C. A. Zorman, A. J. Fleischman, A. S. Dewa, M. Mehregany, C. Jacob, and P. Pirouz, *Epitaxial growth of 3C-SiC films on 4 in. diam (100) silicon wafers by atmospheric pressure chemical vapor deposition*, J. Appl. Phys. **78** (1995), 5136.

Vita

Burton Hamilton Neuner III attended Rolling Meadows High School in Rolling Meadows, Illinois. He then began undergraduate studies at the University of Illinois at Urbana-Champaign, performing research under Professor S. Lance Cooper, and earning a Bachelor of Science in Engineering Physics with a minor in Mathematics. He married his wife Carrie, whom he met at the University of Illinois at Urbana-Champaign, and moved to Austin to attend the University of Texas at Austin to pursue a doctoral degree in Physics. From 2004–2011, he worked as a graduate research assistant for Professor Gennady Shvets and as a teaching assistant for multiple undergraduate laboratory courses. In 2006, he joined the University of Texas at Austin's Doctoral Portfolio Program in Nanoscience and Nanotechnology.

Permanent address: 11970 Jollyville Road 205, Austin, Texas 78759

This dissertation was typeset by the author.